UNIVERSIDADE DE SANTIAGO DE COMPOSTELA

FACULTAD DE FÍSICA
Departamento de Física de Partículas

Coulomb Dissociation of ^{27}P at 498 *A MeV*: an indirect measurement of the astrophysical ^{26}Si(p,γ) reaction

Memoria presentada por:
Saúl Beceiro Novo
como disertación para optar al
Grado de Doctor
en Ciencias Físicas
septiembre de 2011

UNIVERSIDADE DE SANTIAGO DE COMPOSTELA

María Dolores Cortina Gil, Profesora Titular de Física Atómica, Molecular y Nuclear de la Universidad de Santiago de Compostela,

CERTIFICO: que la memoria titulada **Coulomb Dissociation of ^{27}P at 498 *A MeV*: an indirect measurement of the astrophysical ^{26}Si(p,γ) reaction** ha sido realizada por **Saúl Beceiro Novo** en el **Departamento de Física de Partículas** de esta Universidad bajo mi dirección y constituye el trabajo de **tesis** que presenta para optar al **Doctor en Ciencias Físicas**.

Santiago de Compostela, Septiembre de 2011

Fdo: María Dolores Cortina Gil

Abstract

In this work the astrophysical ^{26}Si(p,γ)^{27}P reaction is studied using the Coulomb dissociation technique.
We performed a ^{27}P Coulomb Dissociation experiment at GSI, Darmstadt (28 May-5 June 2007) using the ALADIN-LAND setup which allows complete-kinematic studies. A secondary ^{27}P beam at 498 AMeV impinging a 515mg/cm^2 Pb target.
The relative energy of the outgoing system (^{26}Si+p) is measured obtaining the resonant states of the ^{27}P. Four states are measured at 0.36±0.07, 0.88±0.09, 1.5±0.2, 2.1±0.3 MeV and there is evidence of a higher state at around 3.1 MeV.
The angular distributions were also measure to be compared to the theoretical calculations and as a crosscheck of the measurements.
The total cross section obtained for relative energies between 0 a 3 MeV has been measured and yields 55±7 mb.
The resonance strength and radiative widths for the different resonant states are calculated and compare to previous measurements and theoretical predictions. Astrophysical implications about the competition of our reaction and the β decay of the are also explained concluding that in stellar conditions the capture reaction dominates.

Contents

Chapter 1

Introduction

The aim of this work is to study the Coulomb Dissociation reaction of ^{27}P which is an indirect way of measuring the proton direct capture reaction ^{26}Al(p,γ)^{27}P.
In this chapter the astrophysical interest of the studied reaction is motivated. Mainly we focused on the nucleosynthesis in stellar scenarios and the different ways to prove that this is still an ongoing process. The ^{26}Al is a historical good candidate to prove such scenario, thus nuclear reactions involved in the production and decay of this isotope are of great interest to better understand the process. The reaction studied in this work is competing with the production path of the ^{26}Al and thus its importance.

1.1. Nucleosynthesis in stars

Nuclear physic inputs are of great importance in the building of a coherent picture of the production and evolution of the constituens of the Universe. In particular, the production and evolution of stars is an important topic throghout the history of the science. The success of the theories by Eddington (1920) [Edd20] and Hans Bethe (1939) [Bet39] explaining nuclear fusion processes involved in stars lead the development of nucleosynthesis theories as a key part of the understanding of the Universe.

The famous review paper by Burbidge, Fowler and Hoyle in 1957 [Bur57] stands the stars as the seat of the origin of the elements as previously proposed in 1946 by Hoyle [Hoy46]. Previous theories assumed that nuclide were built in a primordial fireball (for which there was no evidence) at the beginning of the Universe. Those models were very attractive for the scientific comunity and managed to explain many observable features. However,

they failed in the explanation of the observational fact that not all the stars exhibit the same surface composition.

Later on, with the help of satellites, the measurement of γ-rays coming from the Galaxy confirmed the idea of an ongoing nucleosynthesis scenario still active in stars.

The main physical processes involved in stellar synthesis are the Hydrogen burning, Helium burning, Carbon burning, Neon burning, Oxygen burning, Silicon burning, neutron capture via s or r-process (slow and rapid) and proton capture (rp-process).
The temperature and density conditions needed in the different nucleosynthesis processes vary depending on the nuclear reaction processes. For the burning scenarios moderate temperatures are needed ranging from 10^7k for the Hydrogen burning to some 3×10^9k for the Silicon. The temperature increases while going to heavier elements. The same happens with the density. Typical values are in the order of 10^{10}kg/m^3.
Regarding the capture processes, for the neutrons high neutron densities and intermediate-high temperatures are needed, in the order of 10^8 neutrons/cm^3 and 10^8k for the slow and 10^{24} neutrons/cm^3 and 10^9 for the rapid. The proton capture needs an intense proton flux (10^{28} protons/cm^3) and temperatures higher than 0.3 GK.

In particular we are interested in the region of the production ^{26}Al, and this part of the nuclide chart (very proton rich nuclei) evolves mainly due to the rp-process, so let us describe it:

The rapid proton capture process (rp-process) consist of consecutive proton captures producing heavier nuclei. It occurs on the proton-rich side of the nuclide chart producing heavy elements in that region. The end point is not well stablished but it is suggested to be around tellurium. The rp-process is inhibited by α decay.
The process must take place at very high temperature environments (higher that 0.3 GK) so that the protons can overcome the large Coulomb barrier present in charge particle reactions. The time scale is set by the β^+ decays at or near the proton dripline, because the weak interaction is slower than the strong and electromagnetic ones at this temperature regimes but it tipically takes up to 100 seconds. The process needs a huge proton flux, so a hydrogen-rich environment is needed as well.

Nucleosynthesis models using cross sections of nuclear reaction rates try to predict the different stellar scenarios in which the ^{26}Al is being produced. Several sources have being postulated, as the winds of Wolf-Rayet (WR) stars [Pal05], AGB stars, X-ray bursts or classical novae. However, it is not yet clear how much each one of the scenarios contribute to ^{26}Al [Pra96].
The main production scenarios of the ^{26}Al via rp-process are Novae and X-ray bursts.

The measurement of populations of ^{26}Al in stellar scenarios served as a proof of the ongoing nucleosynthesis in stars. This nucleus has a life time of 1.05×10^{6} years, much shorter than the age of the Universe. Thus, the detection of this nucleus is a direct evidence of nucleosynthesis as an ongoing proccess.
The first evidence for live ^{26}Al in the early solar system [Lee77] was the discovery of enhanced ^{26}Mg/^{24}Mg ratios in Ca/Al rich inclusions of the Allende meteorite which is a presolar meteoritic grain [Jos07] (briefly described in section 1.1.3). Afterwards, the measurement of the 1.809 MeV γ -ray line coming from the de-excitation of ^{26}Mg produced by the β -decay of ^{26}Al by the HEAO-3 (High Energy Astrophysics Observatory) satellite [Mah82; Mah84] confirmed the existence of this nucleus in stellar scenarios, confirming that stars are major nucleosynthesis agents.

Afterwards some other γ -ray instruments have also detected the 1.809 MeV line from ^{26}Al. Specially relevant are the measurements that were taken with the COMPTEL (COMPton TELescope) instrument onboard the Compton Gamma Ray Observatory (CGRO) which made an all-sky map of the diffuse emission from ^{26}Al in the galactic interstellar medium [Die95] (Fig. 1.1).
From all the observations, it was concluded that the origin of bulk ^{26}Al is in the galactic plane, and not in foreground sources closer to us.

1.1.1. Novae scenarios

The peak temperatures of novae are supposed to be around 0.5 GK being an appropriate scenario for the rp-process.
Generally, a nova burst can be explained as the result of mass transfer within a close-binary system between a companion star and white dwarf [Gal78].

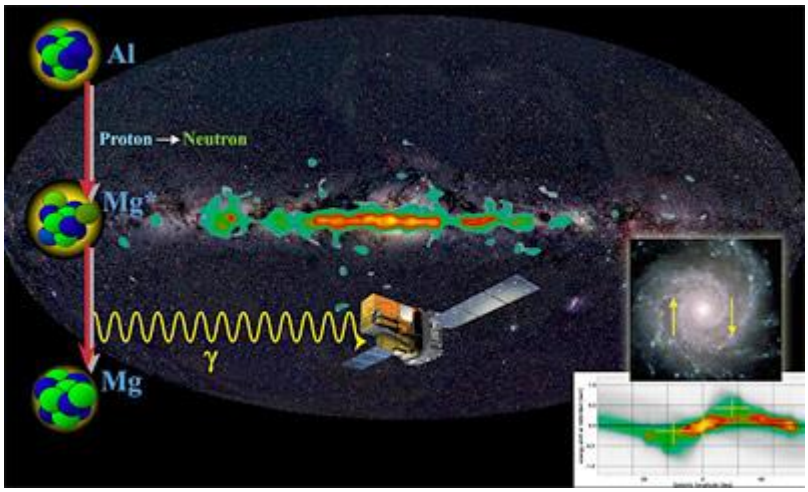

Figure 1.1: Image of the full sky from the COMPTEL data [Die95], showing 1.809 MeV gamma rays from radioactive ^{26}Al, produced in supernovae, concentrated along the Milky Way. Credit: The COMPTEL collaboration and NASA.

The typical composition of a white dwarf is C-O (in the order of 1 $M_\odot$[1]) or, in the case of more evolved progenitors, O-Ne-Mg with masses ranging 1.2-1.4 $M_\odot$. The companion star contains Hydrogen-rich materials which are ejected (typical times of 100 seconds) and infall the white dwarf producing nuclear reactions on its surface. These nuclear reactions release an important amount of energy which leads to a consequent rise in temperature with peak values of 0.1-0.5 GK [Pac84].

The thermonuclear runaway in O-Ne-Mg novae has been suggested to be a possible production site of the nuclide ^{26}Al. The end point of the reaction flow in the nucleosynthesis depends on the mass of the white-dwarfs (Sulfur for 1.2 $M_\odot$ white dwarfs and Calcium for 1.3 $M_\odot$) . In these novae the seed for the production of ^{26}Al is the nuclide ^{24}Mg.
The ^{26}Al is synthesized via ^{24}Mg(p,γ)^{25}Al(β^+,n)^{25}Mg(p,γ)^{26}Al$_{g.s.}$. At low temperature ($\leq$0.3 GK), the ^{24}Mg is produced via ^{23}Mg(p,γ)^{24}Al(β^+,n)^{24}Mg. At high temperatures ($\geq$0.3 GK), the reaction sequence
^{25}Al(p,γ)^{26}Si(β^+,ν)^{26}Al$_m$(β^+,ν)^{26}Mg and possibly ^{25}Al(p,γ)^{26}Si(p,γ)^{27}P bypass the production of ^{26}Al.

[1] $M_\odot$ is the solar mass

1.1.2. X-ray Burst scenarios

X-ray bursts are also possible sites for the rp-process, in particular Type I X-ray bursts. They have been proposed as possible sites for high temperature hydrogen burning via the rp-process. These astrophysical binary systems are composed of an accreting compact object, typically a neutron star, and a companion star. The accretion rate onto the neutron start ranges from 10^{-8} to $10^{-10} M_{\odot}$ per year. Nuclear burning processes at high densities ($\geq 10^5$ g/cm^3) are produced at the base of the accreted envelope, via pp-chains, CNO-cycles, and triple-α-process releasing important amounts of energy. This energy triggers a thermal runaway reaching peak temperatures up to 3 GK. These temperatures are high enough to start the rp-process which causes rapid nucleosynthesis towards heavier proton rich nuclei and produce the ultimate energy which causes an X-ray burst. The burst lasts from 10 to 300 seconds typically [Sch01].

The ^{26}Si(p,γ)^{27}P reaction is on the path of the rp-process in X-ray bursts. The energy generation and timescale of X-ray burst can be affected by this reaction because ^{26}Si β^+ decay lifetime is relatively long compared with the surrounding unstable nuclei. Its competitive processes are ^{26}Si(α,p)^{29}P and β^+ decay of ^{26}Si. The ^{26}Si(p,γ)^{27}P reaction is expected to be dominant except for the region around the peak temperature (T$\geq$1.5 GK),. The ^{26}Si(α,p)^{29}P reaction is also important when the α particle can overcome the Coulomb barrier at T$\geq$1.5 GK. The reaction data for ^{26}Si(p,γ)^{27}P are useful for the estimation of the energy generation and timescale of X-ray bursts, because this reaction is on the main path and dominant process in most temperature as discussed above.

1.1.3. Presolar meteoritic grains

Presolar grains [Jos07] are very small pieces of stardust appeared in primitive meteorites and interplanetary dust particles. Their main characteristic is that they show enormous isotopic anomalies linked to the nucleosynthesis processes that took place in their parent stellar sources.

Explosive scenarios such as novae release huge amounts of energy and eject about 10^{-4} to 10^{-5} $M_{\odot}$ into the interstellar medium. The ejecta are enriched in nuclear material due to the high peak temperatures attained during the outburst, and contain significant amounts of ^{13}C, ^{15}N, and ^{17}O and traces of isotopes such as ^{7}Li, ^{20}Ne, ^{26}Al, ^{28}Si, etc. The observed abundances and composition of the ejecta gives information about the explosive process as

well as for the nucleosynthesis process.
Such information can be partially obtained through the laboratory analysis of presolar grains, which yields isotopic abundance ratios.

In fact, detailed studies of these grains have opened up a new and promising field of astronomy [Zin98].
So far, silicon carbide (SiC), graphite (C), diamond (C), silicon nitride (Si3N4), and oxides have been identified as presolar grains. Ionic analysis of the microprobes showed a big variety of isotopic signatures allowing the identification of the stellar scenarios in which the grains were produced. Some examples are asymptotic giant branch stars (AGB), novae and supernovae [Zin98]. The studied grains are classified into different populations on the basis of their main isotopic ratios.

The study of the isotopic ratios plays a major role in the understanding of those meteoritic grains. Several models try to predict the stellar scenario in which those grains were formed. For those models, the nuclear physics involved in the formation of the different isotopes is of major importance. Currently, the available isotopic abundance ratios for grains of putative nova origin are C, N, Ne, Al, Si and Ti.

In particular, the ^{26}Al/^{27}Al ratio is one of the interesting quantities to complete the "puzzle", thus, the study of the nuclear reactions involved in the production of both ^{26}Al and ^{27}Al is of great interest.

1.2. Nucleosynthesis of ^{26}Al

Nucleosynthesis of ^{26}Al is complicated by the presence of a short-lived $^{26}\mathrm{Al}_m$ (τ 9.15 s) spin isomer. The only way to synthesize the long- lived $^{26}\mathrm{Al}_g$ isotope in nova explosions is through proton capture reactions on ^{25}Mg, which can yield both the ^{26}Al ground and isomeric states [Jos99].
A subset of the nuclide chart with the ions involved in this process is shown in figure 1.2.
The isomeric state decays predominantly to the ground state of ^{26}Mg, while the ground state decays to the first excited of ^{26}Mg giving the γ -ray of 1.809 MeV, (the one detected in galactic measurements). The β -decay of ^{26}Si mainly populates the ^{26}Al(g.s.), and the production of the ^{26}Si comes from the competition of the β -decay ^{25}Al and the reaction ^{25}Al(p,γ)^{26}Si that is destructed in the ^{26}Si(p,γ)^{27}P.

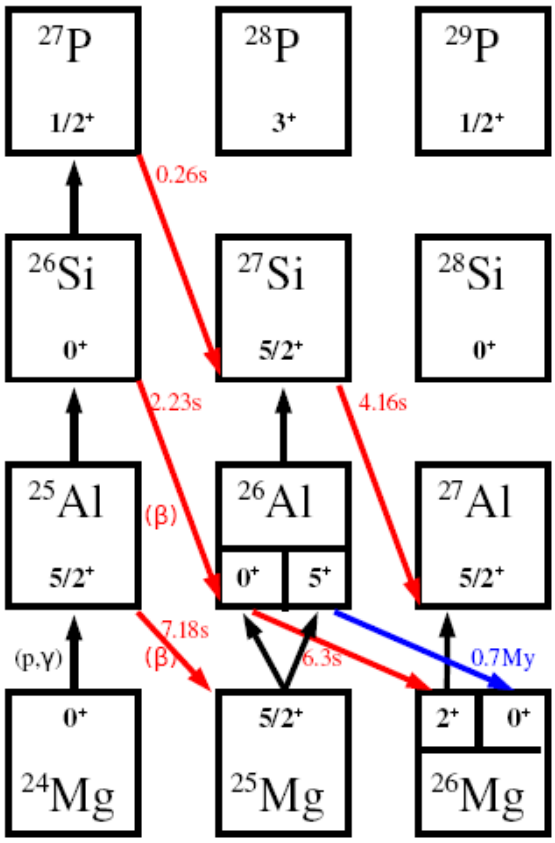

Figure 1.2: Subset of the nuclide chart showing the ions involved in the production of ^{26}Al, including the reaction of interest $^{26}Si(p,\gamma)^{27}P$

The production of ^{27}Al has also a big importance as the ratio ^{26}Al/^{27}Al is of great interest in the study of presolar meteoritic grains (see section 1.1.3). The synthesis of the ^{27}Al is itself a complicated process, whereas it is mainly destroyed by ^{27}Al(p,γ), several mechanisms compete in its synthesis: one is ^{26}Mg(p,γ), with ^{26}Mg coming from its initial abundance, as well as from ^{26}Al$_m$ decay synthesized by ^{25}Mg(p,γ) or through two proton captures on ^{24}Mg, leading to the beta decay of the unstable ^{26}Si. On its turn, the beta decay of ^{26}Si competes with the reaction ^{26}Si (p,γ)^{27}P. Another possibility is ^{27}Si(β+)^{27}Al, with ^{27}Si coming from both ^{26}Al$_{g,m}$(p,γ).
One has to note the beta decay of the ^{26}Si produces only the ^{26}Al$_m$ isomer and not the ground state (which is the one emitting the gamma ray). At stellar temperatures both states are not in equilibrium. A good understading of the production of the ^{26}Al$_m$ is then crucial to explain the synthesis of the ^{27}Al.

Within this scenario the ^{26}Si(p,γ)^{27}P reaction appears as important, not only for being a reaction in the rp-path but also for its implications in the generation of ^{26}Al and ^{27}Al, both isotopes of enormous astrophysical interest. The Coulomb barrier for this reaction can be calculated by using a simple Coulomb potential function $U = k\frac{Z_p Z_{Si} e^2}{R_p + R_{Si}}$, being $k = 1/4\pi\epsilon_0$ and ϵ_0 the permitivity of free space, e the charge of the electron, Z_i and R_i the atomic numbers and radii of the involved species (proton and Si). For our reaction, the estimated Coulomb barrier is 3.5 MeV, which gives a temperature ($E = k_B T$, k_B Boltzmann constant) of T=27GK.

The direct study of the reaction ^{26}Si(p,γ)^{27}P at astrophysical energies is extremely challenging due to the low intensity associated to radioactive beams and low cross sections involved. Coulomb dissociation studies of the inverse kinematics reaction ^{27}P(γ,p)^{26}Si have instead been proposed in this work. A ^{27}P beam impinges on thick Pb target. The ^{27}P is then excited via the absorption of a virtual photon to a particle unbound state which decays into p+^{26}Si. This inverse reaction profits of a much larger cross section.

Chapter 2

Physical principles

In this section the physical principles applied to the study of the reaction of interest are explained. The direct measurement of the reaction was not favoured in the laboratory, so we decided to do an inverse kinematics experiment by using the Coulomb dissociation technique and virtual photon method which are explained in this chapter.

2.1. Radiative capture reaction

Nuclear capture reactions such as (p,γ) play a major role in the study of the Universe. One of the main goals of the nuclear astrophysics is to determine reaction rates for the capture reactions that are involved in the different nucleosynthesis processes and evolution of stars.
In this kind of reactions the high Coulomb barrier involved due to the precence of charged particles, makes it hard to reproduce the reactions in the laboratory.
In a charge particle reaction, two main energetic components play a major role: the quantum mechanical tunneling function through the Coulomb barrier and the thermal energy distribution (Maxwell-Boltzmann). The convolution of the two of them gives a narrow peak between them called Gamow peak.
The typical Coulomb barriers for this reactions (in the order of MeV) lead to a Gamow window energy of some hundreds of keV for a typical stellar temperature, meaning that most of the reactions will take place in that window. Thus, a direct measurement would need a low energy beam of ^{26}Si at 300 keV. The cross section for the (p,γ) reaction would be tiny at this energy regime (in the order of nb) because the energy of the interacting nuclei is far below their Coulomb barrier. A direct measurement would require a very

intense ^{26}Si beam or would need a measurement over many days in order to get enough statistics. Besides, most of this reactions involve radioactive targets which make very difficult and sometimes impossible to measure the reaction using conventional methods. The background/signal ratio is also a major problem to overcome for a direct measurement.

Even though the direct measurement is very challenging, some facilities are prepared to measured some of these reactions like for instance the LUNA collaboration [Bem05]. In this case they have measured reactions of great interest like ^{2}H(p,γ)^{3}He or ^{14}N(p,γ)^{15}O. The astrophysical Gamow peaks lie in energies less than 100 keV, thus, the direct measurement is performed at this energy regime.
To overcome the background problem, LUNA is located underground in the Gran Sasso laboratory, so most of the cosmic contributions are eliminated effectively. This combined with windowless gas targets and high efficiency detection techniques, makes the direct measurement possible.

For our reaction of interest ^{26}Si(p,γ)^{27}P, the direct measurement is extremely challenging; for example in typical novae conditions, the energy of the Gamow window is around 300 keV, so a low energy beam would be needed and also a radiactive target of short half live. The cross section of such a reaction would be tiny (in the order of nb).
To overcome this issue, we propose an indirect methode to extract the (p,γ) reaction cross section from the inverse reaction which can be effectively measured as compared to the direct one: the Coulomb dissociation.

2.2. Coulomb Dissociation reaction

The Coulomb dissociation technique [Bau86] [Win79] is proposed as a very suitable method for the investigation of electromagnetic transitions between a bound state of two particles and resonant states at small relative energies between the resonant particles. In this method, the nuclear Coulomb field is used as a source for the photodisintegration process, so instead of the direct (p,γ), the time reverse reaction (γ,p) is measured (see fig. 2.1). The Coulomb field of the target induces the reaction and acts as a photon, thus, it is calle virtual photon. The number of equivalent photons can be calculated theoretically (see Appendix **??**), so the experimental measurement of the Coulomb breakup can be used to obtain the corresponding γ-induced cross section (see section 2.4). Using the detailed balance theorem the related direct capture reaction cross section (which is the astrophysical interesting

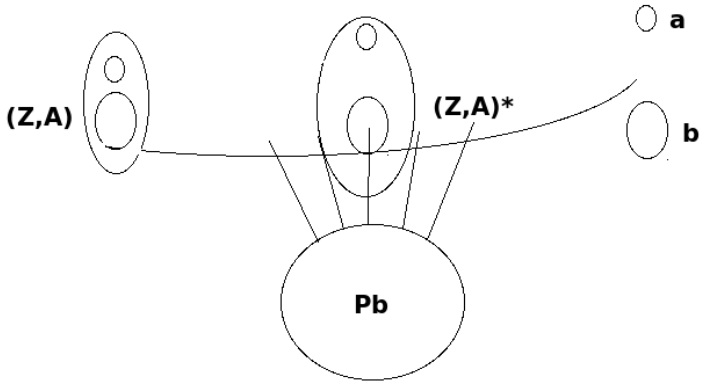

Figure 2.1: Schematic view of a Coulomb Dissociation breakup

one). Since the phase space for a photon is between 100 to 1000 times larger than that of a particle beam, the cross section is enhanced.
As this inverse reaction is performed at relativistic energies, the use of much thicker targets is possible, and thus, the cross section is again enlarged as compared to the direct measurement.
The main disadvantages are that this method cannot be used when higher-order effects like coupled channels play a role, and that with this kind of measurement the information obtained at high energy, has to be extrapolated to the astrophysical region.

In this experiment for the reaction a ^{27}P projectile beam is used and excited by the field of a thick Pb target.

In the past this method has been applied to very important reactions like ^{13}N(p,γ)^{14}O [Mot91] [Kie93], ^{11}C(p,γ)^{12}N [Lef95] or ^{7}Be(p,γ)^{8}B [Iwa] [Mot94] among others.

2.3. Invariant Mass method

The measurement of the excitation function of exotic nuclei is one of the very interesting observables that can be obtained in a Coulomb dissociation experiment. The excitation energy provides information on the electromagnetic modes of the different transitions of the reaction and thus allows further studies of cross section components.

The invariant mass is a Lorentz invariant, which is very helpful for changing from rest frame to laboratory frame. In the rest frame of a given object, the invariant mass is equal to its rest mass m_0.
For the reconstruction of the invariant mass, four-momentum vectors, which are composed of the total energy and of the three momentum vector components, are used:

$$\mathbf{P}^{\mu} = \begin{pmatrix} E \\ p_x \\ p_y \\ p_z \end{pmatrix} \tag{2.1}$$

$$M_{inv}^2 = \eta_{\mu\nu}\mathbf{P}^{\mu}\mathbf{P}^{\nu} = E^2 - p_x^2 - p_y^2 - p_z^2 \tag{2.2}$$

where $\eta_{\mu\nu} = \mathrm{diag}(1, -1, -1, -1)$ is the Minkowski metric and $c = 1$.

Equation (2.2) shows that the invariant mass squared is the inner product of the four-momentum. The invariant masses of the excited incoming (1) and outgoing (2) systems can be written as it follows:

$$M_{inv}^{(1)} = m_{proj} + E^* \tag{2.3}$$

$$M_{inv}^{(2)} = \sqrt{\begin{pmatrix} \sum_i E_i \\ \sum_i \overrightarrow{p_i} \end{pmatrix}^2} \tag{2.4}$$

with the subindex i summing all fragments in the outgoing channel. The excitation energy E^* in expression (2.3) is decoupled from the projectile invariant mass m_{proj} after expanding the total invariant mass in a Taylor series, where the recoil of the photon on the heavy ion is neglected. The energy of the gamma photons may as well be decoupled from the heavy fragments in a similar way for the outgoing invariant mass.

For a two-body decay the invariant mass of the outgoing system can then be written as:

$$M_{inv}^{(2)} = \left\{ \left[\left(m_1^2 + \mathbf{P_1}^2\right)^{1/2} + \left(m_2^2 + \mathbf{P_2}^2\right)^{1/2} \right]^2 - (P_{1x} + P_{2x})^2 - (P_{1y} + P_{2y})^2 - (P_{1z} + P_{2z})^2 \right\}^{1/2} \tag{2.5}$$

and taking into account the conservation of the invariant mass, $M_{inv}^{(2)} = M_{inv}^{(1)}$ and the excitation energy can be calculated as:

$$E^* = \left\{ \left[\left(m_1^2 + \mathbf{P_1}^2\right)^{1/2} + \left(m_2^2 + \mathbf{P_2}^2\right)^{1/2} \right]^2 - \left(P_{1x} + P_{2x}\right)^2 - \left(P_{1y} + P_{2y}\right)^2 - \left(P_{1z} + P_{2z}\right)^2 \right\}^{1/2} - m_{proj} \tag{2.6}$$

One can also do the calculation in terms of masses and velocities by neglecting the energy of the emitted gamma photons in a first step, getting an energy and momentum terms for (2.4) as it follows:

$$\left(\sum_i E_i\right)^2 = \sum_i \left(\gamma_i m_i\right)^2 + \sum_{i \neq j} \gamma_i \gamma_j m_i m_j \tag{2.7}$$

$$\left(\sum_i \overrightarrow{p_i}\right)^2 = \sum_i \left(\beta_i \gamma_i m_i\right)^2 + \sum_{i \neq j} \beta_i \beta_j \gamma_i \gamma_j m_i m_j \cos\vartheta_{ij} \tag{2.8}$$

Taking into account that $\gamma^2\left(1 - \beta^2\right) = 1$, equations (2.7) and (2.8) are introduced into expression (2.4), to which the gamma energy has been added, providing the following outgoing invariant mass:

$$M_{inv}^{(2)} = \sqrt{\sum_i m_i^2 + \sum_{i \neq j} \gamma_i \gamma_j m_i m_j \left(1 - \beta_i \beta_j \cos\vartheta_{ij}\right)} + E_\gamma \tag{2.9}$$

Due to the conservation of the invariant mass, the excitation energy is expressed by:

$$E^* = \sqrt{\sum_i m_i^2 + \sum_{i \neq j} \gamma_i \gamma_j m_i m_j \left(1 - \beta_i \beta_j \cos\vartheta_{ij}\right)} + E_\gamma - m_{proj} \tag{2.10}$$

Expression (2.10) shows that the reconstruction of the excitation energy relies on the identification and tracking of all outgoing species and on the rest mass of the incoming ion.

2.4. Extraction of radiative capture cross section

The measurement of the excitation energy allows the calculation of the cross section for the Coulomb Dissociation reaction. Besides, by using the

virtual photon theory (see appendix **??**) this value can be converted to the cross section of the radiative capture as in 2.11.

$$\sigma_{(\gamma,p)} = \frac{\sigma_{CD} E_{ex}}{N_{vp}} \tag{2.11}$$

where E_{ex} is the excirtation energy and N_{vp} the equivalent photon number. Applying the detailed balance theorem, the radiative capture cross section can be calculated as it follows:

$$\sigma_{(p,\gamma)} = \frac{2J_{res}+1}{(2J_P+1)(2J_{Si}+1)} \frac{k_\gamma^2}{k^2} \sigma(\gamma, p) \tag{2.12}$$

where J_P and J_{Si} are the spin of the incoming nuclei (^{27}P and ^{26}Si) and J_{res} is the spin of the compound nucleus in the resonant state. k and k_γ are the wave numbers of the outgoing channel (^{26}Si+p) and photon wave number respectively. They can be calculated as it follows:

$$k^2 = \frac{2\mu E_{rel}}{\hbar^2} \tag{2.13}$$

$$k_\gamma = \frac{E_{exc}}{\hbar c} \tag{2.14}$$

2.4.1. Parametrisation of a resonant state

The capture cross section in the resonant peaks can be well described by a Breit-Wigner parametrization [Rol88]:

$$\sigma_{\text{cap}}(E) = \frac{\pi}{k^2}\, \omega\gamma\, \frac{\Gamma}{(E-E_r)^2 + \Gamma^2/4} \tag{2.15}$$

where the total resonance width $\Gamma = \Gamma_p + \Gamma_\gamma$ is the sum of the particle width Γ_p and the γ width Γ_γ. The resonance energy is denoted by E_r and $\hbar k$ is the p-^{26}Si relative momentum in the continuum state. The resonance strength

$$\omega\gamma = \frac{2J+1}{(2J_p+1)(2J_{Si}+1)} \frac{\Gamma_\gamma \Gamma_p}{\Gamma} \tag{2.16}$$

depends on the widths and on the total angular momenta of the fragments J_p, J_{Si} and of the resonance J in the continuum.
The integration of a Breit-Wigner in a resonance gives the following:

$$\int_0^{infty} \sigma_{BW}(E) dE = 2\pi^2 \bar{\lambda}_R^2 \omega\gamma \tag{2.17}$$

where $\bar{\lambda} = \hbar/p_r$ being p_r the relative momemtum of the outgoing fragments, defined as

$$p_r = \sqrt{2\mu E_r}$$

2.5. Determination of Stellar Reaction Rates

A very important quantity for astrophysical studies is the stellar reaction rate per particle at a given temperature [Rol88].
During the evolution of a star the temperature changes, and so does the reaction rate. In general it is defined as:

$$\langle \sigma v \rangle = \left(\frac{8}{\pi \mu} \right)^{1/2} \frac{1}{(k_B T)^{3/2}} \int_0^\infty \sigma(E) \exp\left(-\frac{E}{k_B T} \right) dE \tag{2.18}$$

where k_B is the Boltzmann constant, T the temperature, μ the reduced mass, E the energy and $\sigma(E)$ the cross section. For a resonant state, as the cross section can be parametrised as a Breit-Wigner the reaction rate can be converted to the following expression as explained in detail in reference [Rol88]:

$$\langle \sigma v \rangle = \left(\frac{2\pi}{\mu k_B T} \right)^{3/2} \hbar^2 (\omega\gamma)_R \frac{1}{(k_B T)^{3/2}} \exp\left(-\frac{E_R}{k_B T} \right) f \tag{2.19}$$

where the variables with subindex R indicate that are evaluated in the resonance and f is the so-called screening or electron shielding factor which at typical densities and compositions varies between 1 and 2.
Usually what is given is the product of the rate and the Avogadro number, and then the expression in energy units of MeV and temperature in GK can be written and taking $f = 1$ as:

$$N_A \langle \sigma v \rangle = \frac{1.54 \times 10^{11}}{(\mu T)^{3/2}} \omega\gamma \exp\left(-\frac{11.605 E_R}{T} \right) \tag{2.20}$$

The representation of this quantity helps in understanding the main capture process at a given temperature. Thus one can study if a resonant process is dominant and in which temperature region this happens.

Chapter 3

The ^{26}Si(p,γ)^{27}P capture reaction

The radiative capture reaction (p,γ) for ^{26}Si is relevant in the nucleosynthesis process of ^{26}Al in stellar scenarios. A subset of the nuclide char containing the ions and reactions involved in the scenario is represented in figure 1.2.
The main production sequence of this nuclide is ^{24}Mg(p,γ)^{25}Al(β^+,ν)^{25}Mg(p,γ)^{26}Al. An alternative way is the chain ^{24}Mg(p,γ)^{25}Al(p,γ)^{26}Si(β^+,ν)^{26}Al. The β destruction of the ^{26}Si to ^{25}Al competes with the proton capture reaction ^{26}Si(p,γ)^{27}P which bypasses the production of ^{26}Al. The study of the reaction rate and the competition between these reactions may help in a better understanding of the nucleosynthesis process.

This destruction is dominated in novae conditions by resonant radiative proton capture via the first excited state ($\frac{3}{2}^+$) in the continuum to the $\frac{1}{2}^+$ ground state in ^{27}P. The electromagnetic transition competes between M1 and E2.

The main purpose of the C.D. experiment is to determine the resonant states and study the different electromagnetic contributions to the gamma decay of the $\frac{3}{2}^+$ state of the radiative capture reaction.

In the present chapter, nuclear models used for the theoretical input of the reaction are explained as well as the interesting parameters which are used in the analysis. For a simulation of the breakup reaction a reasonable model of the initial system (in this case ^{27}P) has to be constructed as well as a good breakup mechanism. The work was done by Stefan Typel [Typ07]. The

parameters used for the calculation with the CDXS+ program are explained.

3.1. Nuclear model of the ^{27}P nucleus

A potential model with a proton interacting with an inert ^{26} Si core can be a good description for the states of the ^{27}P nucleus which is the relevant system for the studied reaction. The solution of the Schrödinger equation with the adequate boundary conditions gives the corresponding bound and continuum wave functions that are represented on a radial grid with spacing 0.1 fm and a maximum standard values for the radius parameter r_0=1.25fm. and diffuseness parameter a=0.65fm. The depths of the nuclear potential are adjusted in each partial wave to reproduce the binding energy of the ground state in ^{27}P with respect to the breakup threshold into proton and ^{26}Si and the resonance energies in the continuum. The Coulomb contribution is assumed to be that of a homogeneously charged sphere with radius parameter 1.25fm.

In a simple single-particle model for ^{27}P with a proton bound to a ^{26}Si core, one would expect to describe the ground state ($1/2^+$) by a $S_{1/2}$ proton state and the second resonance ($3/2^+$) by a $d_{3/2}$ proton state; but such a simple model will give a pure E2 electromagnetic transition following the selection rules but it is known that the first state is a M1+E2 mixture. Consequently, a more refined model must be used taking into account the deformation of the system.
For that purpose Skyrme Hartree-Fock calculations with the parametrization SKX [AB98] were performed usinga code designed for the description of deformed axially symetric nuclei [Typ03]. The given solution predicts a prolate $1/2^+$ ground state with deformation parameter β_2=0.247 for the ^{27}P.

In the present study we are interested in the radiative capture reaction of a proton (p,γ) but being studied through a breakup reaction (Coulomb Dissociation). The cross section of those processes can be converted one into the other as explained in section 2.4. Let us explain some hints on the theoretical models which can explain both reaction mechanisms:

3.2. Radiative Capture Reaction

With the explained parameters for the model system, the electromagnetic transition matrix elements were calculated using the standard value 2.793 μ_N for the magnetic dipole moment of the proton. The model predicts a non-resonant contribution dominated by an almost constant E1 transition. The resonant contributions are prominent with the very sharp $\frac{3}{2}^+$ and $\frac{5}{2}^+$ resonances that are connected to the $\frac{1}{2}^+$ ground state by M1/E2 and E2 transitions, respectively. The capture cross section in the peaks is very well described by a Breit-Wigner parametrization as explained in section 2.4.1. In table 3.1 the resonance parameters obtained in the calculation are specified.

Table 3.1: Parameters of the resonances in ^{27}P.

J^π	E_r [MeV]	E^* [MeV]	σ [mb]	Γ_p [eV]	Γ_γ [eV]	$\omega\gamma$ [eV]
$\frac{3}{2}^+$	0.3376	1.1990	4.7	0.1841	2.113×10^{-4}	4.226×10^{-4}
$\frac{5}{2}^+$	0.7536	1.6150	5.7	30.78	1.385×10^{-4}	4.154×10^{-4}

The E2/M1 ratio for the capture reaction is depicted in figure 3.1 as a function of the relative energy E in the continuum. In general, the E2 contribution is much larger than the M1 contribution but near the $\frac{3}{2}^+$ resonance the situation is reversed.

3.3. Coulomb dissociation of ^{27}P

In this case a single particle potential model is used to calculate the cross section for the ^{208}Pb(^{27}P,^{26}Si p)^{208}Pb breakup reaction with a 500 A MeV beam. The Coulomb dissociation is treated in the relativistic semiclassical approximation; this can be done because the diffraction effects are negligible at this energy regime.
In order to prove it, a trial calculation was performed with an optical folding potential in the EDAD 1 parametrization (fig. 3.2). The result shows that it exist only a small oscillation of the diffraction corrected model as compared to the pure semiclassical result, indicating that diffraction effects are not very important and that a pure semiclassical calculation gives reasonable results. Only at larger scattering angles where the absorption of the projectile becomes important the diffraction corrected calculation becomes considerably smaller than the simple semiclassical result.

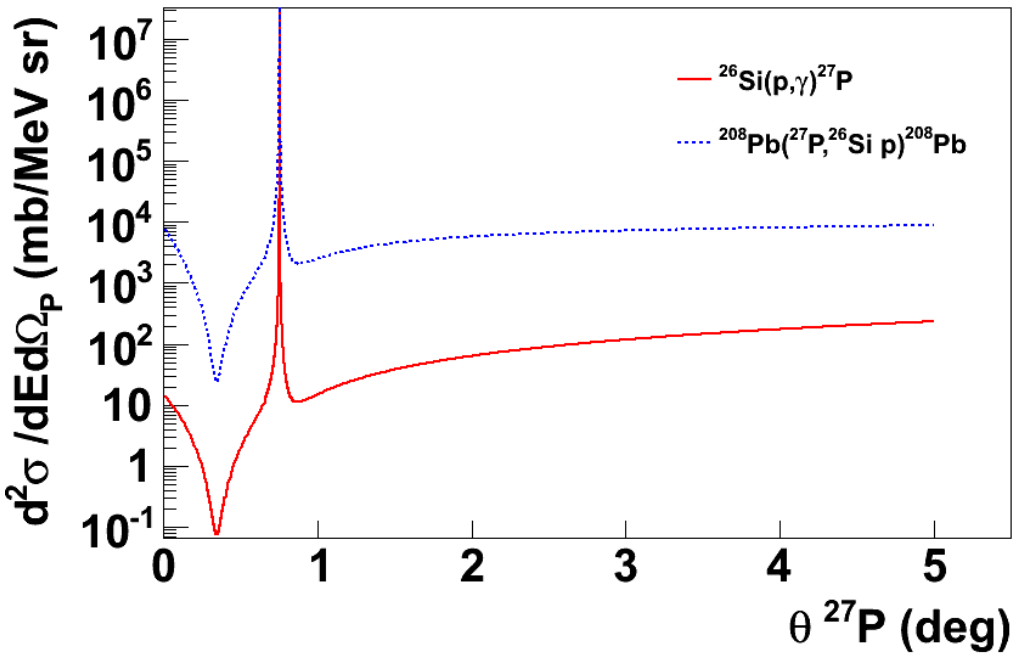

Figure 3.1: E2/M1 ratio for the radiative capture reaction $^{26}Si(p,\gamma)^{27}P$ (red solid line) and the breakup raction $^{208}Pb(^{27}P,^{26}Si\ p)^{208}Pb$ at 500 A MeV projectile energy (blue dashed line) as a function of the fragment relative energy.

The semiclassical Coulomb breakup cross section is shown then in figure 3.3 as a function of the relative energy E, calculated by the integration of the double differential cross section in the scattering angles ranging from zero to 1.5°. The E2 contribution is strongly enhanced compared to the E1, and the M1 is mainly suppressed. In figure 3.1 the E2/M1 ratio for the C.D. and the direct capture is represented. For the C.D. the E2 dominates in all the energy regime. Special comment deserves the $\frac{3}{2}^+$ resonance in which the M1 contribution amounts about the 3.6% of the total cross section. This fact makes the direct measurement of the M1 component very difficult. An even smaller percentage of the M1 component would be more favourable for the C.D. experiment.

The full triple differential cross section for the Coulomb breakup of ^{27}P was used for the Monte-Carlo simulation of the reaction. An event distribution with 100000 entries was generated and used as an input for the GEANT4 simulation of the experiment.

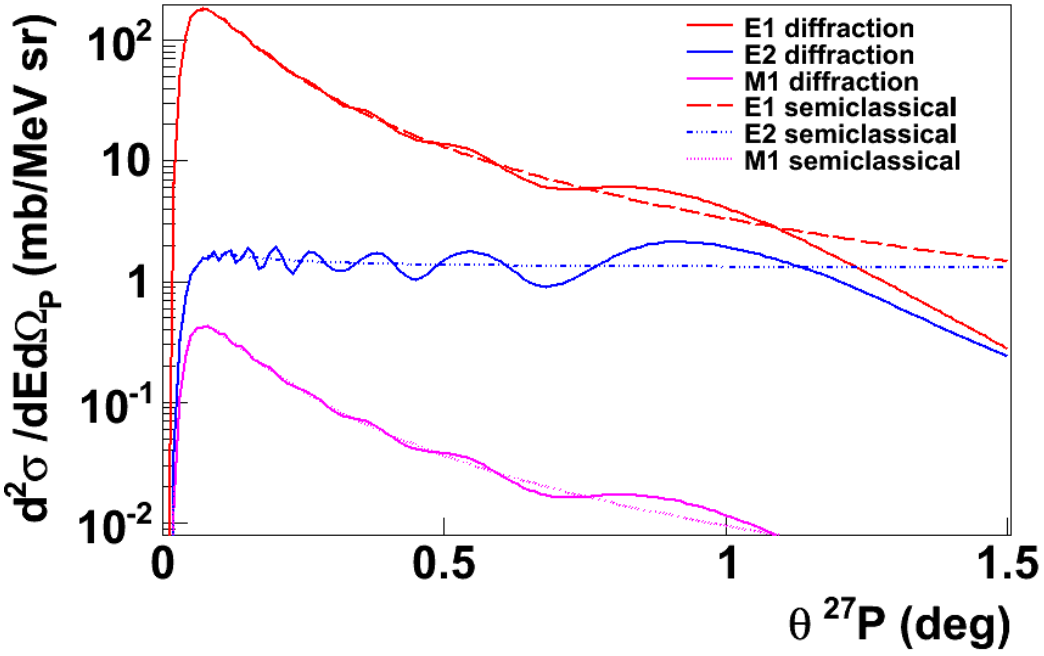

Figure 3.2: Contributions to the double differential cross section of the breakup reaction $^{208}Pb(^{27}P,^{26}Si\ p)^{208}Pb$ at 500 A MeV projectile energy and 0.5 MeV fragment relative energy as a function of the ^{27}P scattering angle: E1 (red), E2 (blue), and $10^4\times$ M1 (green). Solid lines correspond to the pure semiclassical approximation and dashed lines correspond to the semiclassical approximation with the eikonal correction for diffraction. Only the s-wave ground state was considered in the calculation.

According to this model, the total breakup cross section estimated for relative energies up to 3 MeV is about 98.7 mb with 83.0 mb, 14.5 mb, and 1.2 mb for the E1, E2, and M1 contributions, respectively. The $\frac{3}{2}^+$ resonance (M1+E2) contributes with about 4.7 mb and the $\frac{5}{2}^+$ resonance (E2) with about 5.7 mb to the total cross section.

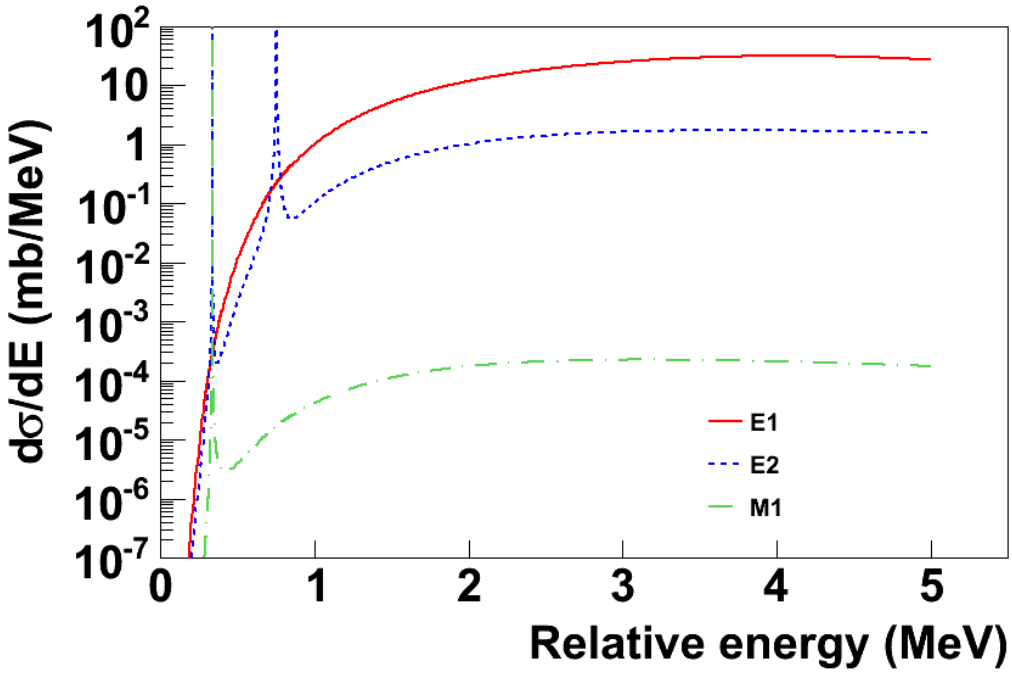

Figure 3.3: Contributions to the single differential cross section of the breakup raction $^{208}Pb(^{27}P,^{26}Si\ p)^{208}Pb$ at 500 A MeV projectile energy integrated between $0°$ and $1.5°$ ^{27}P scattering angle as a function of the fragment relative energy : E1 (red solid line), E2 (blue dashed line), and M1 (green dot-dashed line).

Chapter 4

Experimental setup

The experiment was performed at the German laboratory Hemholtz zentrum fur Schwerionenforschung (GSI) (figure 4.1) located in Darmstadt. In particular in the ALADIN-LAND experimental setup.
In this chapter we will introduce the experimental setup and some hints on the performance of the different detectors which were used for the experiment.

4.1. GSI facility

A schematic view of the facility is shown in figure 4.1. This facility allows the production and acceleration of heavy ion exotic beams. The ion sources allow to produce ions ranging from protons to uranium that are then first injected into the UNIversal Linear ACcelerator (UNILAC), which accelerates the ions up to an energy of 11.4 AMeV [UNI]. The beam is then transmited to the SchwerIonenSynchrotron (SIS 18), which accelerates the ions to the desired energy. The versatility of the UNILAC and SIS accelerators gives access to ion beams of all possible stable and long-lived unstable primary beams with maximum energies ranging from 1 AGeV in the case of uranium to 4.5 GeV for protons [Gei92].
In the present work, the primary beam is ^{36}Ar, that is directed towards the FRagment Separator (FRS) after the acceleration in SIS.

4.2. Fragment separator

After the accelaration of the beam in the SIS18 synchrotron it is transmited to the FRS [Gei92] [Gei95] [Mue92] where the secondary beam is produced and selected (Fig. 4.2). For the production of radioactive beams, the

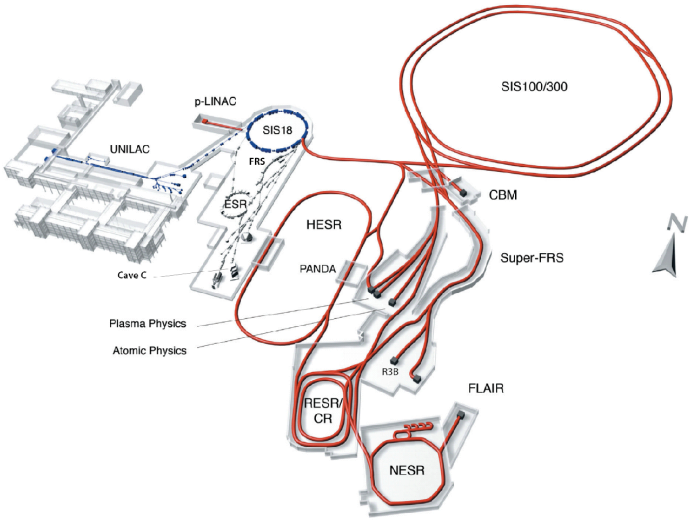

Figure 4.1: GSI accelerator facility (depicted with blue line) and the future FAIR (in red)

high energy primary beam impinges a 4.19 g/cm^2 Be production target. A large amount of nuclear species are produced via nuclear fragmentation due to the relativistic energy of the projectiles. The reaction products together with the unreacted beam enter the first half of the FRS, filtering out all species except the ones with specific A/Z ratio, according to the setting of the magnetic field. The passage of a charged particle through a magnetic field is described by

$$B\rho = \frac{p}{Q} \propto \frac{A}{Z}\beta\gamma \tag{4.1}$$

being B the strength of the magnetic field, ρ the curvature radius of the trajectory, p the momentum of the particle, Q its charge, A and Z the mass and atomic number, respectively, β the velocity and γ the associated Lorentz factor. The expression 4.1 does not take into account the mass defect. For the selection of a given ion with known A and Z, having into account that the radius ρ is physically fixed by the geometry of the FRS, the only variable that can be tuned is the magnetic field B. The velocity of the ions is related to their production mechanism; the width of that velocity distribution must be narrow in order to prevent losses due to the limited acceptance of the magnets, forcing the velocity variation between the primary and secondary ion beams to be small.
The momentum resolution of the FRS is $\Delta p/p = 2\%$ [Gei92]. With this resolution the secondary beam still includes multiple non desired species in

the focal plane after the first two magnets. The insertion of an aluminuum degrader into de beam path at the intermediate FRS focal plane is decisive to further select a pure specie. Since the energy loss is proportional to Z^2 according to the Bethe-Bloch formula [Bet30], the magnetic rigidity of the various charges will be different in the second $B\rho$ separation stage of the FRS allowing the isolation of a quasi-pure secondary beam. The ion of interest can be software-selected in an event-by-event basis by means of a combined identification based on energy-loss and time-of-flight as explained in chapter 5.

The FRS is fully equiped with detectors for the tracking of the ions used for online alignment of the beam during the set up of the experiment. Two plastic-scintillator paddles are placed at the two focal planes of the FRS respectively, the one at F2 (in the middle of FRS) is called S2 and the one at F8 (at the end of FRS) is called S8. Each one is read out by two photomultipliers. The data for those two plastic-scintilators together with the first scintillator detector placed at the entrance of Cave C (POS), are then used to calculate the time of flight of the different ions which allows the A/Z identification: The S2 and S8 scintillators can provide the velocity measurement of the incoming ions. Since the trajectory between them is not rectilinear, the distance is not well defined and depends on the effective beam trajectory. The actual velocity measurement is then performed using the POS detector which is presented in next section.

4.3. ALADIN-LAND setup

After the selection of the secondary beam in the FRS with an approximate length of 17 m, the exotic nuclei are transmited to the ALADIN-LAND setup in Cave C (Fig. 4.3) which has a total length of around 15 m from the first detector (POS) to the very last time-of-fllight wall.

1. Along the path to the ALADIN-LAND reaction target the incoming species are tracked and identified with the help of the incoming detectors.

2. The target area comprises a target chamber that contains a target wheel, which allows changing the target without entering the cave and a microstrip-silicon detector located just behind it. The Crystal Ball

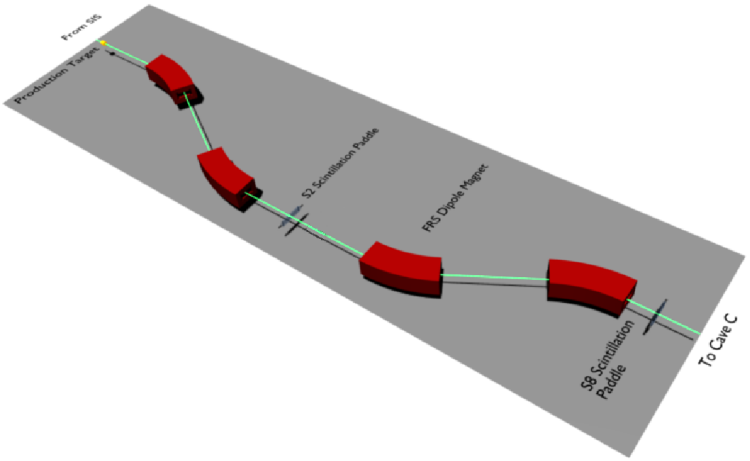

Figure 4.2: Schematic view of the FRS from the reaction target to S8. It consists of 2 stages with two dipole magnets each. After every stage a plastic scintillator is located in order to perform time-of-flight measurements.

detector surrounds the target and guarantees the detection of gamma-rays originated in the reaction.

3. Then A Large Area DIpole magNet (ALADIN) separates the species produced in the reaction according to their magnetic rigidities, in particular in this experiment we are interested in protons and heavy fragments (mainly ^{26}Si).

After ALADIN we can distinguish two branches: one that allows the tracking of the protons, composed by two drift chambers (DCH) and a tof wall (TFW); and another branch for the heavy fragments with two fiber chambers (GFI) and a smaller tof wall (NTF).
This ensamble of detectors allows the kinematically complete measurement of the reaction of interest.

Let us describe the three sections of the setup in detail.

4.3.1. Incoming detectors

In this region represented in figure 4.3 a set of scintillator and tracking detectors are located for the identification of the different incoming species. Starting from the entrance of the beam line in the cave the first one is the ROLU (not in the figure) which controls the beam aperture, then a position

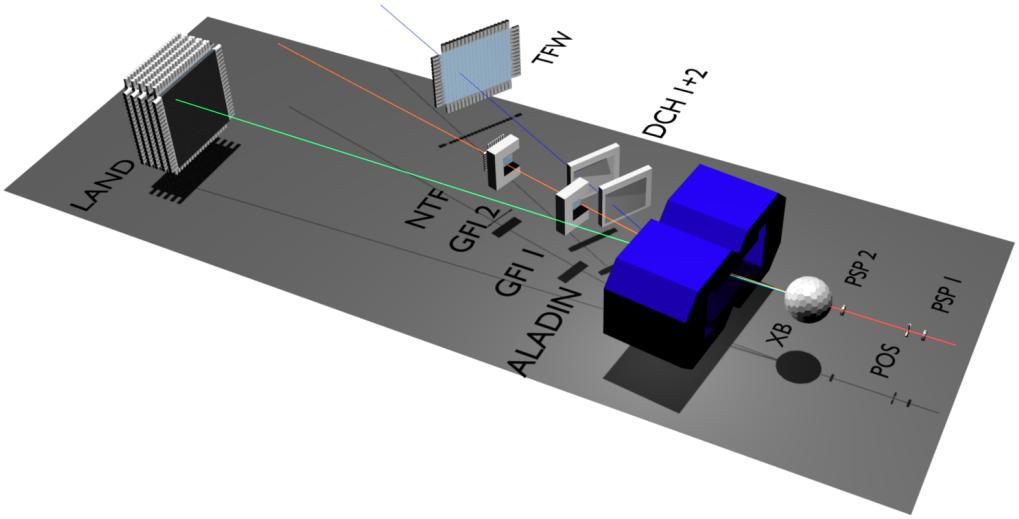

Figure 4.3: Schematic view of the entire setup. The beam line comes from the right in the pictures and leave signals in order in the PSP1, POS, PSP2 and the Crystal Ball surrounding the reaction chamber in the incoming area, then crosses ALADIN and splits in protons, which leave signal in both DCH and TFW, and heavy ions which are measured in both GFI and NTF.

sensitive silicon pin diode detector (PSP1) to measure position and charge, afterwards a plastic scintillator (POS) to measure time-of-flight and just before the target chamber another silicon detector PSP2.

In the FRS the scintillator at S2 and S8 provide a time-of-flight measurement which allows to calculate the velocity of the fragments and consequently the ratio A/Z for the fragments. However, the charge of the fragments and their angles of the trajectory must still be determined.

The first detector found in the line is the **ROLU** (first drawing in figure 4.4). The acronym ROLU stands for Rechts Oben Links Unten (right top left bottom), and indicates the position of the four plastic scintillators which form the detector (each one read out by a PM tube) with respect to the beam axis. Each scintillator can be driven into the beam line with a small robot, creating a rectangular variable aperture for the ions. ROLU is normally used as a veto for the beam by acting on the beam trigger in an anti-coincidence mode. In the present experiment, the ROLU was most often set to a square aperture of (2.5×2.5 cm^2). Besides the two scintillators of the FRS, at the entrance of Cave C there is a thin plastic-scintillator detector (POS) ($5 \times 5 \times 0.02$ cm^3) read out by four photomultipliers (Second drawing of figure 4.4). **POS** gives the time reference for all the other detectors and can also be used to get a better measurement of the ratio A/Z. The flight time from S8 to POS can be measured and used to get a better determination of the velocity of the fragments at the entrance of the cave[1]. This detector can also provide energy loss and position measurements but these quantities are measured with much higher resolution with the PSP.

The position sensitive silicon pin diode (**PSP**) detectors ($4.5 \times 4.5 \times 0.03$ cm^3) consist of a pin diode of a high resistivity n-type Si, with a 300 μm thick Si wafer. Implementation of boron ions into one side of the n-type Si forms a p-n junction, which serves as an anode, while the other side serves as a cathode. The charge deposited in the detector is read out from all four corners of the anode side (Q_1, Q_2, Q_3, Q_4) allowing the position reconstruction (third picture of figure 4.4). The charge is also collected from a contact on the cathode side (Q), which is used to measure the total energy loss of the incident particle through the detector and from which the charge Z can be calculated. The position measured in the two PSP provides the position of the reaction

[1]If the velocity is calculated just using S2 and S8 information, one needs to simulate the energyloss efect in order to calculate the velocity at the entrance of the cave; by using the velocity in POS, most of the matter is already taken into account

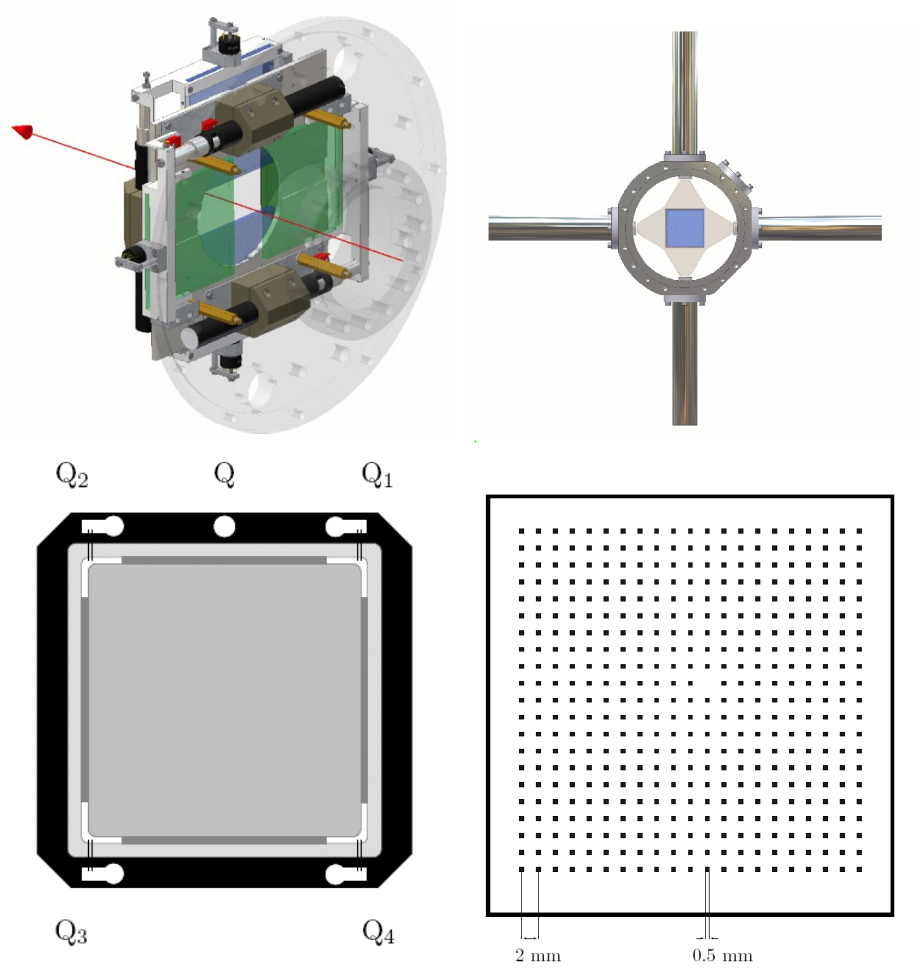

Figure 4.4: The main incoming tracking detectors: the first drawing shows a layout of ROLU a veto for the beam. The second one is POS, a scintillator readout by four photomultipliers. The third one is a PSP, a silicon detector with one anode and four cathodes. The last picture shows a pixel mask used for the position calibration of the PSP.

vertex in the target by extrapolation. The absolute time at which the ion reaches the target is also extrapolated from the measured velocity. Both extrapolations are strongly dependent on the geometrical knowledge of the setup and the estimated flight path.

In order to get a position measurement of the hits in PSP, a **PIXEL** mask detector is also located in the incoming line and used for the calibration. This pixel detector is exclusively used for the position calibration of the PSP detectors. It is mounted on a retractable structure, allowing its removal from the beam path whenever it is not required for calibration. It consists of a clear plastic mask with 21 $\times$ 21 (0.5 $\times$ 0.5 mm^2) square scintillator pixels with a pitch of 2 mm (last drawing of figure 4.4). The scitillation light is collected by the mask and detected by a PM tube. A coincidence measurement of the PSP and of its pixel detector provides a projection of the pixel layout on the PSP, which is distorted before calibration. A map can then be stablished using a cluster-finding algorithm, in order to make the positions of the pixels match.

4.3.2. Target region

The target is mounted on a rotating wheel which allows changing from lead to carbon or empty that are the three configurations needed for this experiment. The wheel is fixed inside an aluminuum spherical reaction chamber which has vacuum inside (Fig. 4.5). Also inside the reaction chamber, there are 5 micro Strip Silicon Detectors (SSD) allowing precise position measurement. Surrounding the chamber the 4-pi gamma spectrometer Crystal Ball [Met82] calorimeter is located. It measures gamma rays emitted by the deexciting fragments.

Silicon Strip Detectors (SSD)

Silicon strip detectors have been used in this setup for the first time during this experiment. They have been developed for tracking (in x and y) of protons and heavy ions produced in high-energy reactions. Additionally, they also give information on the atomic number of the tracked particle via energy-loss measurement. The detector design is originally based on double-sided Si microstrip detectors (SSD) developed for tracking high-energy cosmic rays (protons up to Fe nuclei) at the Alpha Magnet Spectrometer (AMS) to be deployed to the International Space Station (ISS) [Sta06]. To detect si-

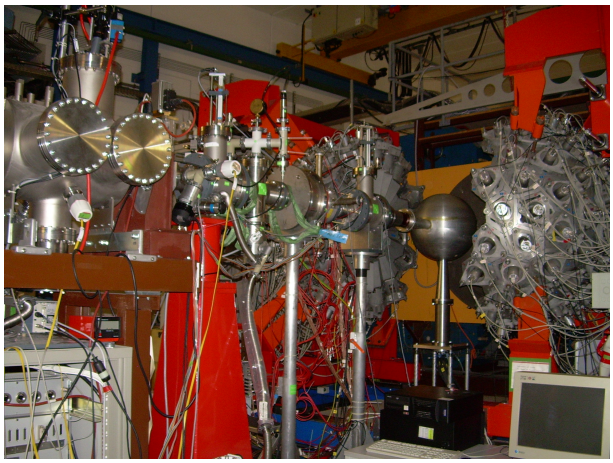

Figure 4.5: Picture of the reaction chamber inside the Crystal Ball (open)

multaneously protons and the residual heavy nuclei it is necessary to have a low-noise and a wide-range integrated-circuit amplifier.

Each Si sensor has an active area of 72 mm × 40 mm, and is 0.3 mm thick. At relativistic energies the reaction products are strongly forward focused, thus a high position resolution, and therefore a high granularity of the Si detectors is required in order to distinguish the different products. In order to distinguish different particles a separation of at least one strip is required. If this is not the case, the two particles are treated as a single cluster and then as only one particle. Therefore, each sensor has an implantation pitch on the junction side (called S-side or p-side) of the sensor of 27.5 μm. The corresponding read-out pitch is 110 μm, i.e. every fourth strip is connected to a read-out channel, while the others are left floating. On the ohmic (K- or n-) side of the sensor, the implantation pitch is 104 μm with every strip being read out. This adds up to 640 strips to be read out on the S-side and 384 on the K-side, yielding a total of 1024 channels per sensor. Two printed circuit boards ("hybrids") are glued back to back, and they perform readout of a single sensor. Each silicon sensor is connected electrically to these boards through flexible capton cables.
The sensors require a bias voltage of 75 V; the strips are coupled to the Front-End-Electronics (FEE) through coupling capacitors. Electrical connections to the strips are made via thin capton cables and wire bonding. A photograph of the sensor plus FEE is shown in figure 4.6.

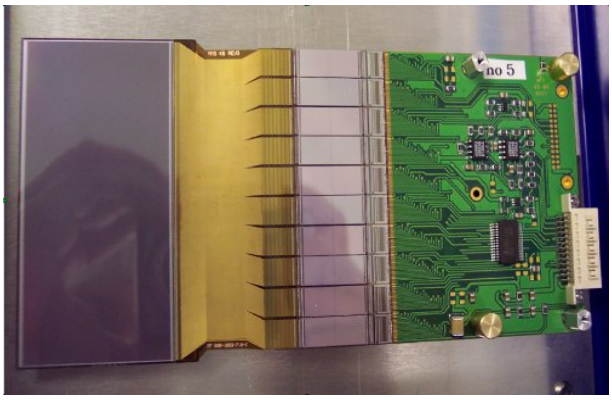

Figure 4.6: Photograph of a SSD detector showing (from left) the sensor, the capton cable, the coupling capacitors, the VA chips, the front-end electronics board, and the 26-pin S-side connector.

Crystal Ball

Around the target a spherical 4π calorimeter is mounted in order to detect the possible gammas coming from the deexcitation of the reaction products and thus helping to identify the excited state in which the reaction products are produced. This detector is an array consisting of 162 NaI crystals, read-out by photomultiplier tubes, forming a sphere of inner radius of 25 cm and thickness of 20 cm. The geometry is such that each crystal covers the same solid angle of 77 msr. In order to optimise a regular angular coverage four different shapes of crystals were used: a regular hexagon (12 crystals) and three kinds of irregular pentagons (60 + 60 + 30).

All the crystals can be easily dismounted, making place for a beam-line or auxiliary equipment such as a target holder, etc. Furthermore, left and right hemispheres of the ball are movable on a kind of rails. They can be moved apart and back by means of an integrated motor system. The whole construction is mounted on a platform of 2×4 m size.
Even though it was not designed for in beam gamma detection, the relatively high granularity of the detector allows for the correction of Doppler shift. On the other hand, the large volume of the crystals and compact geometry provide high detection efficiency and a possibility of reconstruction of the total energy of gamma rays Compton scattered from one crystal to the other.

4.3.3. ALADIN

After the reaction chamber A Large Area DIpole magNet is placed. This magnet is used to separate the heavy and light fragments due to their different magnetic rigidity Bρ. The curvature radius of a given charged particle in a magnetic field varies according to the expresion $B\rho = \frac{Am_0}{Ze}\beta\gamma c = 3.107\frac{A}{Q}\gamma\beta\ [Tm]$ being B the magnetic field, ρ the curvature radius, Z and A charge and atomic mass of the nucleus (respectively), e the electron charge, m_0 one atomic mass unit, β the velocity of the nucleus in units of the speed of light, γ the Lorentz factor and c the speed of light in vacuum. This magnetic rigidity allows the separation of light particles like for instance protons in this experiment and heavy fragments. In our particular case, the protons produced at around 500 MeV are deflected at approximately 31 deg for currents of about 2000A, while a heavy fragment like ^{26}Si in the same current conditions only 16.7 deg. This separation allows the independent tracking of both species produced in the reaction.
Among the most remarcable characteristics of ALADIN there is an angular acceptance of $\pm$60 mrad, the gap is 0.5 m heigh and 1.54 m width. The magnet consists of two coils with 11$\times$15 turns each. The maximum current is 2500 A whose central field strength is 1.66 T and a voltage of 600 V. For currents higher than 1900A the relation between magnetic field and current is not linear anymore due to saturation effects as seen in figure 4.7. The effective length for 2500 A is 1.41 m.

In figure 4.8 a picture of the spatial behaviour of the spatial components of the magnetic field is shown for different cuts.

4.3.4. Proton branch

After the magnet, the protons produced in the reaction are deflected around 31 deg, thus a setup of tracking detectors is located at this angle in order to measure the position and be able to calculate de momentum of the protons. In particular, two multiwire Drift Chambers (DCH) are used for tracking purposes and a time of flight wall (TFW) which determines the velocity of the protons together with the measurement at the start detector (POS)

Drift chambers (DCH)

Specifical DCH have been recently developed for the ALADIN-LAND setup and were used for the first time for this experiment. They were im-

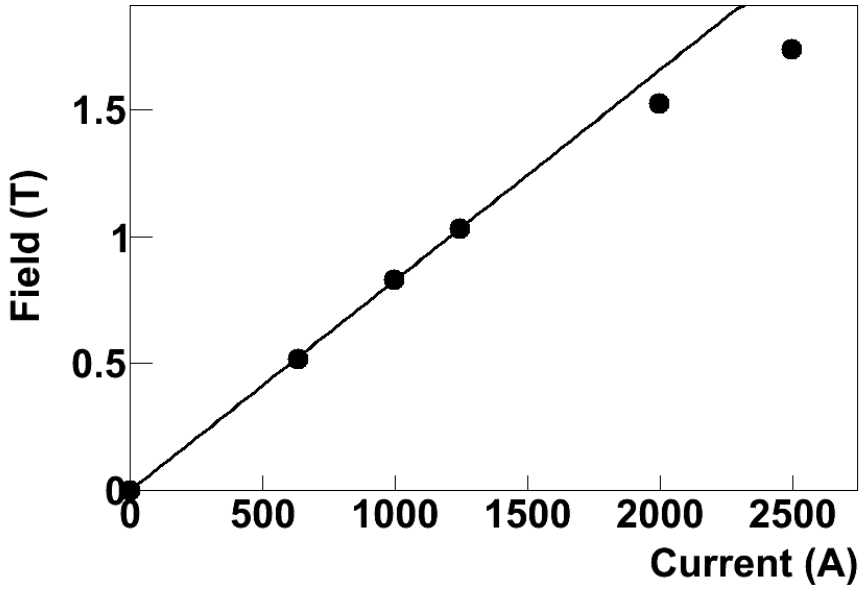

Figure 4.7: Magnetic field of the ALADIN magnet versus the applied current. At 2000A the relation is not linear anymore due to saturation effects.

plemented to allow an accurate proton detection and consist on a set of two identical drift chambers built at PNPI Gatchina/St. Petersburg following the concept of the SPES 4π Forward Spectrometer drift chambers [Zuc00].

Each DCH [R3B05] covers an active area of $100\times80\text{cm}^2$; by using a GEANT4 simulation (see chapter 6) with a theoretical proton distribution typical of a Coulomb dissociation, we obtain a detection acceptance of protons behind the magnet within a 95% . The geometry and the operational parameters were optimized to detect minimum ionizing particles with an efficiency larger than 95% and a spatial resolution better than 0.2 μm. The intrinsic resolution and the straggling were estimated with Monte-Carlo simulations providing a relative momentum resolution of $\Delta\text{p/p} = 3 \times 10^{-3}$ for protons including the tracking though the dipole magnet.

Mechanically, each DCH comprises and x and y plane, both placed in a common housing. It has 256 read out channels, 144 sense wires for detection in x and 112 in y-direction. The outer dimensions are 120 cm length, 100 cm height and 15 cm depth. For each plane, six layers of field wires define hexagonal drift cells in two different depths of the detector. Each individual drift cell has a diameter of 16 mm and is being read out via one sense wire

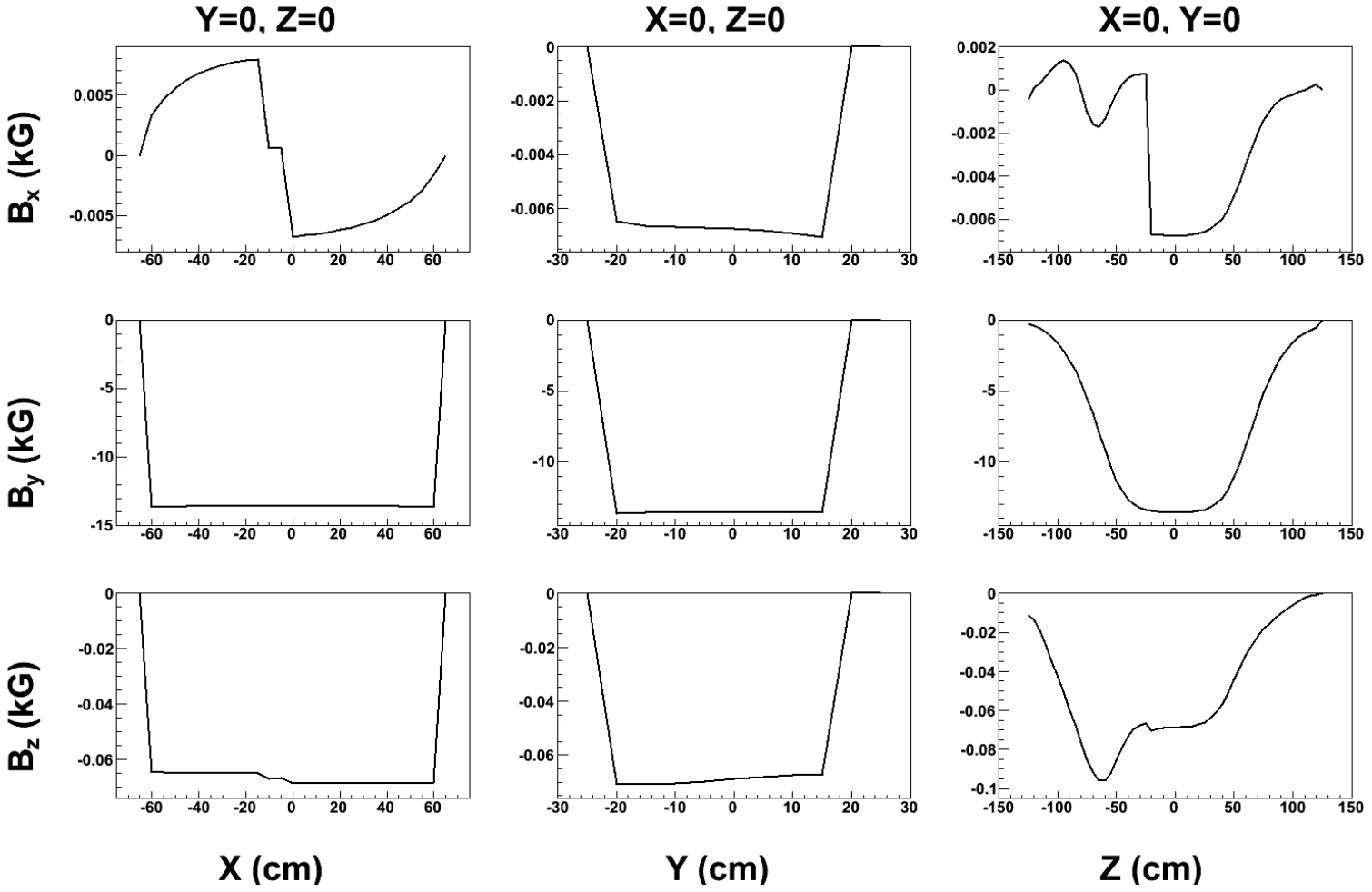

Figure 4.8: Spatial behaviour of the ALADIN magnetic field components. Each column shows Bx, By, Bz respect upside down: the first one for a cut Y=0 Z=0, the second X=0 Z=0 and the third X=0 Y=0

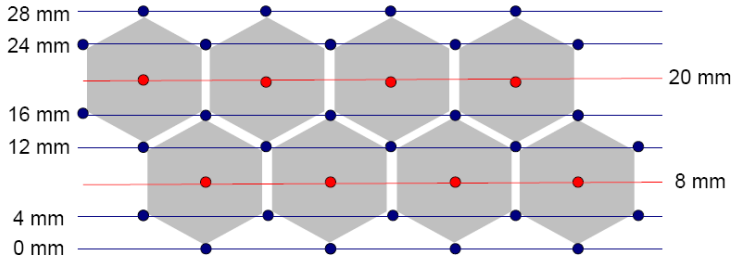

Figure 4.9: Layout of the DCH: two layers of sense wires composed of hexagonal cells with six layers of wires each

in its centre (figure 4.9). The field wires consist of 75 μm diameter copper-beryllium, while the sense wires are build of 25 μm diameter gold-plated tungsten. The detector is built with 8 consecutive layers like this.

The window foil consist of mylar, metallized from the inner surface with aluminum to prevent charge from collecting on it.
One important issue that needed to be handle, was that the DCH are built to detect protons and could result seriously damaged if heavy fragments interact with the chambers; this is specially dramatic for the first DCH that is closer to the beamline center. To minimize straggling before the first reacted proton is detected it is advisable to locate first DCH as close to the magnet as possible but at the same time one has to guarantee that the DCH frame does not interfer with the heavy fragments trajectory. This favours a design with the thinner possible frame in the side which faces the center of the line and it is closer to the fragments trajectory. The final design, allowed to build this frame with a thickness of only 80 mm because all read-out electronics and power-supply cables are attached to the other side, away from the fragments, and also to the top of the support.

The gas mixture used during the experiment, was the one suggested by the manufacterers that comprises an 80% Argon and a 20% CO_2.

Regarding the events reconstruction, as said before, each DCH consists of two separate layers, one for detection of x coordinates and the other for detection in y coordinates. Each layer consists of two rows of sense wires. Each row has an offset of half a cell width with respect to the following one. Each sense wire is surrounded by six field wires forming a hexagonal drift cell. A particle which passes though the DCH in a direction approximately perpendicular to the detector surface is certain to cross two adjacent cells, one in each row. This gives two radii values which are the distance to the

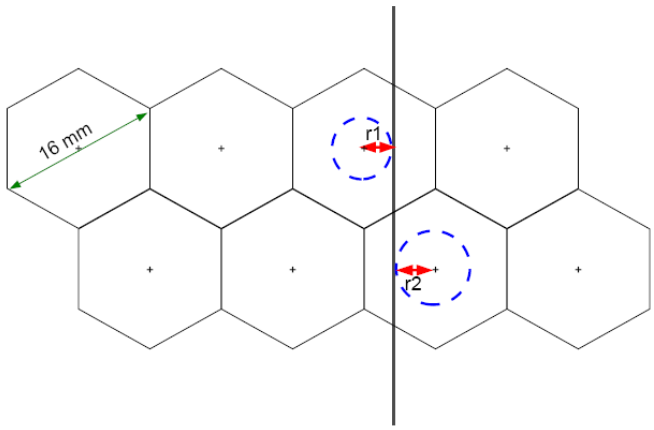

Figure 4.10: Drift length measured in the hexagonal cells

center of the cell: r_1 for the first cell and r_2 for the second one. This allows one to accurately determine the position of the particle within the inter-wire distance of 6.92 mm. When a particle interacts with cells number i and i + 1 being x_i and x_{i+1} the corresponding sense wires coordinates, position can be determined in a first attemp as

$$x = \frac{x_i + x_{i+1}}{2} \tag{4.2}$$

The reconstruction within the inter-wire distance uses the drift length r derived from the measured drift time. Thus, we can talk about the reconstruction within a cell.

The position can be determined with higher accuracy by taking the drift time of the electrons into account. Assuming the dependence between a drift time t and an drift length $r=r_1+r_2$ is known (fig. 4.10), the position x of the track between the two sense wire positions x_i and x_{i+1} is:

$$x = \frac{x_i + r_i + x_{i+1} - r_{i+1}}{2} \tag{4.3}$$

Time of flight wall (TFW)

This detector is used for the determination of the stop time for the heavy fragments and also to get a charge identification of them, allowing the identification of the outgoing products of the reaction. The TFW detector consists of two planes of plastic scintillator paddles placed perpendicular to the beam

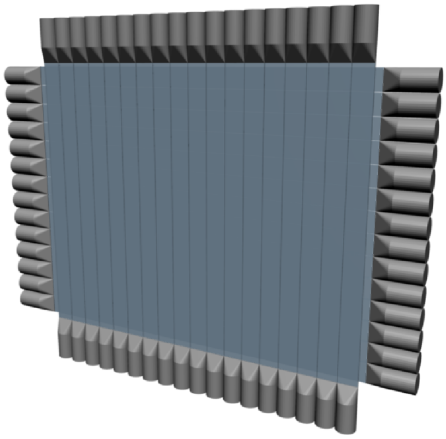

Figure 4.11: Layout of the Time of Flight Wall

direction, one with 18 horizontal paddles and one with 14 vertical paddles, as illustrated in Fig. 3.9. The size of the paddles is 189×10×0.5 cm^3 and 147×10×0.5 cm^3 for the horizontal and vertical direction respectively. Each paddle is read out by two PMs mounted at the end of the paddle, delivering time and energy signals. This method of constructing a detector with two layers is very advantageous and allows us to make coincidence of events for ions interacting within the scintillator. The technique known as self calibration is based on the fact that an event passing through two paddles was produced at the same time and with the same energy. This allows a comparison of paddles against each other with a very high level of accuracy in the calibration.

The detection principles are based on the production of light when an ion passes through the scintillator material due to the excitation of electrons. When these electrons de-excite they create light in the visible range. The amount of light produced is proportional to both the charge of the ion and its velocity. This light produced then propagates along the length of the scintillator and is measured by the PM tubes. The scintillator paddles must be wrapped ensuring that no light pollution from the lab enters the detector. The scintillator is not perfectly transparent and some losses of light occur during propagation. This effect can also be used to determine the hit location of a given fragment as ilustrated in Fig. 4.12. In tis situation, not only PM tube 1 and PM tube 2 observe different arrival times, but they also observe different energies. By averaging the energy values we can calculate the energy of the initial hit. And by taking the difference in the time we can

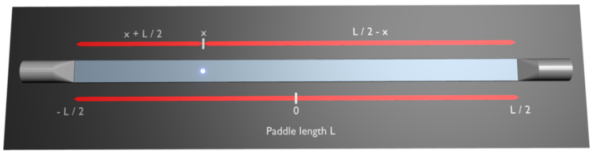

Figure 4.12: Hit of one particle in one of the paddles of TFW

calculate the point at which it originated with a position resolution of 1 - 2 cm which is not sufficient to significantly contribute to the tracking of the particle even though it helps to select reaction fragments which should fulfil a given condition in position for the TFW.

4.3.5. Heavy Fragments branch

In the reaction also heavy fragments are produced (mainly in our case ^{26}Si) that are less deflected than protons in ALADIN. At the energy range we work (≈500 AMeV) with an ALADIN current of around 1800 A, we expect a deflection of around 16.7 deg, thus a set of tracking detectors is located covering this angle. It is composed by two large area walls, one based on scintillator fibers GFI (GroßFiber detektor) and the other is a standard plastic paddle wall, NTF (New ToF wall).

Große FIberdetektor (GFI)

The large-area scintillating fiber detector (GFI) [Cub98] [Mah09] provides horizontal position measurements of fragments with high precision. Each detector has an area of 50×50 cm^2 and consists of 475 thin and long (0.1×50×0.1 cm^3) scintillator fibres placed parallel and close to each other, as illustrated in Fig. 4.13. Each fibre is coated with white paint to minimise cross talk between neighbours, which, however, causes a small reduction in the efficiency of the detector. Fibres are glued from one end to a mask in a sequential way, covering an array where each fibre has a distinct (u, v) coordinate on the plane of the mask, as shown by the numbering in Fig. 4.13. This mask is then coupled to the face of a Position-Sensitive PM (PSPM), which consists of a photocathode, meshtype dynodes and a multi-wire anode with 18 wires in the u direction and 16 in the v direction, creating a rectangular grid. The other end of the fibre is coupled to an ordinary PM for triggering purposes.
When a charged particle passes through a fibre it causes scintillation light which is guided on the mask where it appears as a light spot on the plane

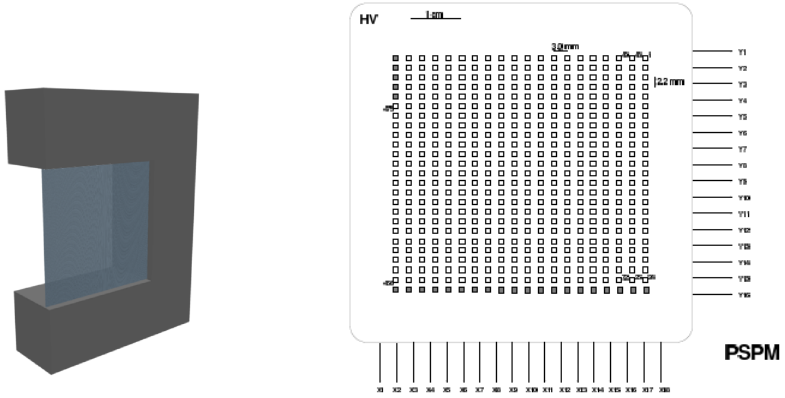

Figure 4.13: On the left a layout of the GFI detector used to track the heavy fragments. The figure on the right shows the mask used to guide the fibres on the position sensitive photomultiplier (PSPM)

of the photocathode. The energy signal of each wire is read out and used to reconstruct the (u, v) coordinate of the light spot on the plane of the photocathode and from there it is associated to the fibre that was hit. The calibration procedure relies on a similar algorithm to the PSP detectors, getting the horizontal position via a coordinate system transformation. This requires the calibration of the PM tube using a so-called sweep run, during which the ion beam is swept over the various detectors of the fragment branch by varying the magnetic field of ALADIN. The position of each fiber can then be determined with a cluster-finding algorithm in order to establish the complete mapping of the fiber mask, which is used for the coordinate transformation.

New time of flight wall, (NTF)

The goal of the NTF in the our experiment is the same as the TFW but for the protons in this case. It provides a time stop signal in order to calculate time-of flight. It can also be used to determine the charge of the particles (which would allow to determine if any residual particle different to a proton passes through the proton branch).

The NTF is a detector made with plastic scintillator material and modern photo-multiplier tubes. It is very similar to the TFW (Time of Flight Wall) although the use for each detector is slightly different.

The NTF is constructed with paddles which are strips of plastic scintilla-

tor of 60mm width and 480mm length with photomultipliers at either end. These are arranged in two layers, the first (and nearest to the beam) has 8 paddles lying side by side in vertical stripes. Directly behind, the second layer is arranged in a perpendicular way with again 8 paddles lying horizontally, completing a square.

Whereas TFW is placed at a large angle to the ALADIN to detect light ions that suffer stronger deflection by the magnetic field, NTF detects heavier ions that are bend by a shallower angle.

Due to the wide variety of beam types, the NTF is responsible for measuring a wide variety of ions. With the limited range in sensitivity of photo multiplier tubes the NTF detector needs re-calibration for every beam type.

The readout and calibration procedures are very similar to the ones described for the TFW. The charge-mass ratio is also calculated in the same way as explained for the TFW; and by combining the two PM signals it is possible to obtain position information. This position information has rather moderate resolution and is not used for tracking but plays, however, an important role in the calibration procedures.

Chapter 5

Data analysis

The experiment subject of this work (S223) uses the complex setup of detectors presented in chapter 4 which need many complicated calibration procedures before useful physical information can be extracted from the data. In this sense, there has been a big effort in the last years to write a general analysis code that enhances its reusability. This code is called `land02`[LAN] and was originally written by Håkan Johansson and contains a group of calibration routines which can be applied to the data files in order to perform the different calibration levels.
In the present chapter the different steps in the calibration are explained, coming from raw data up to the momentum recontruction and tracking of the different particles.

5.1. Data Calibration Levels

The set of detectors used for the experiment generate analog signals that are digitized and stored in an event-by-event basis. The information obtained is either a time measurement given by a TDC module with respect to a trigger signal or a charge or amplitude measurement from QDC or ADC respectively. The data are organised in list mode data files (lmd) consisting of lists of events from which the information must be extracted and calibrated for further use. The extraction process is called unpacking and it is done by the `land02` program, and converts the lmd files into a ROOT [ROO] file which can afterwards be directly used for the ROOT program to make calculations. The calibration procedure can be divided into several levels:

RAW level

This level provides the access to the data as it has been stored without any calibration applied, thus all values are given in channel units. The unpacker is simply used to link a physical detector with the electronic channels of the data-acquisition system. This level is extensively used during the experiment to easily check the status of the detectors.

TCAL level

In this level the information coming from TDC channels is converted to time units (usually nanoseconds) and it is also performed a pedestal subtraction value from the measured energy values. `land02` provides tools to easily calculate the calibration parameters needed (mainly slopes and offsets) through the routines `tcal` and `clock` .

SYNC level

Usually the detectors are composed of a set of different units, for instance paddles, in the previous calibration levels each electronic channel was treated individually withot taking into account any other information coming from other subunits of the detector. In order to be able to consider a detector as an entire unit, all its channels must be syncronized with respect to each other. The calibration method is strongly dependent on the detector, but generally we need to illuminate the entire detector with a known source that allows the syncronization; after that all energy and time data of the different subunits can be compared and combined.

DHIT level

DHIT stands for detector-hit level and combines the time and energy information from the SYNC level according to the detector geometry. This provides position, mean time and energy loss of a hit in detector-internal coordinates.

HIT level

The HIT level provides data in the laboratory frame coordinates. The information regarding detector geometry is used to convert de DHIT data into HIT and be able to use the data for further analysis.

TRACK level

This level combines information of several detectors, in order to get kinematical information, which requires geometrical information of the setup as input. This step allows for instance the reconstruction of the reaction position in target or the identification of Z and A for the incoming cocktail beam, which is very useful taking into account that during the same run several different reactions can be measured at the same time and are only selected afterwards in the analysis with software. Despite the work done some steps are not yet implemented within the land02 framework and have to be done using external routines: this is the case of the tracking of charge particles through the magnetic field. For this purpose a tracker program was written by Ralf Plag [LAN], allowing to calculate the momenta of the particles from the measured position and magnetic field.

5.2. Calibration of different detectors

The detectors we need to calibrate can be grouped into different types: S2, S8, POS, TFW and NTF are based on plastic scintilator paddles, PSP and SSD are silicon detectors and then GFI and DCH are big chambers allowing to measure position. The calibration routines for the plastic scintillators can be generally explained and then applied to each of them:

5.2.1. Plastic scintillator detectors

Plastic scintillator paddles are read out by two photomultiplier tubes (PM) providing time and energy information. The information is extracted by averaging both signals. Position can also be calculated by measuring time differences or energy ratios between the tubes. Complex detectors (i.e. TFW and NTF) are composed by several scintillation paddles (subunits) that need to be synchronized to each other in order to work as a homogeneous entity. A usual paddle has a PM in each corner as in figure 4.12, considering the PM located at the left and right ends of the paddle, the measured times and energies are expressed as it follows:

$$
\begin{aligned}
t_L &= \frac{1}{v_{eff}}\left(\frac{L}{2}+x\right)+T \\
t_R &= \frac{1}{v_{eff}}\left(\frac{L}{2}-x\right)+T \\
e_L &= E\exp\left[-\frac{\left(\frac{L}{2}+x\right)}{\lambda}\right] \\
e_R &= E\exp\left[-\frac{\left(\frac{L}{2}-x\right)}{\lambda}\right]
\end{aligned}
\tag{5.1}
$$

being v_{eff} the effective light velocity in the scintillation material, l the length of the paddle, x the position of the interaction in the paddle, T the time of the interaction, E is proportional to the deposited energy at the interaction point and λ the light attenuation length of the scintillator material. Subindex L and R stand for left and right respectively. A fraction of the deposited energy is withdrawn in the electronics chain, in order to build the timing signal. Since the measured individual times and energies are position dependent, the time and energy loss of the interaction are calculated using both measurements:

$$
\begin{aligned}
T &= \frac{t_L+t_R}{2}-\frac{l}{2v_{eff}} \\
\ln E &= \frac{\ln e_R+\ln e_L}{2}+\frac{l}{2\lambda}
\end{aligned}
\tag{5.2}
$$

The position of the interaction can be calculated using either the measured times or energies:

$$
\begin{aligned}
x &= v_{eff}\left(\frac{t_L-t_r}{2}\right) \\
x &= \lambda\left(\frac{\ln e_R+\ln e_L}{2}\right)
\end{aligned}
\tag{5.3}
$$

All the expresions used until now are ideal, they do not take into account that the analog signals are processed and digitized during the acquisition; to have a realistic measurement, one should account the cable lengths, signal losses and processing times; this is done by setting the calibration parameters. Also the measured quantities are collected in channel numbers that need to be converted into physical magnitudes. For instance, the measured times in a PM tube of a detector built of several paddles can be calculated as:

$$\begin{aligned} t_{L_{cal}} &= t_L \cdot \alpha_{t_L} + T_{diff} + T_{sync} + T_{L_{cal}} \\ t_{R_{cal}} &= t_R \cdot \alpha_{t_R} - T_{diff} + T_{sync} + T_{R_{cal}} \end{aligned} \tag{5.4}$$

where $t_{L_{cal}}$ and $t_{R_{cal}}$ are the calibrated times in nanoseconds, t_L and t_R the raw times in channels, α_{t_L} and α_{t_R} the time-calibration-slope parameters which reflect the time-to digital conversion, i.e. the conversion factor of TDC channels to time units; $T_{L_{cal}}$ and $T_{R_{cal}}$ the time-calibration-offsets which take into account cable lengths and processing time (it usually can be set to zero); T_{diff} the time difference parameter which synchronizes the two PM tubes of the same paddle, such that the hit in the middle of the paddle will give a time difference of zero; and T_{sync} the time-synchronization offset parameter which synchronizes all the paddles of the same detector versus each other. The evaluation of T_{sync} is achieved by considering a full illumination of the detector having at least two crossing paddles with a registered hit; the synchronization offset is then adjusted in order to equalize the measured mean times of both paddles.

The calibration of the energies measured by the paddles is treated in a very similar way as for the times; the energies can be expressed as in the following equations:

$$\begin{aligned} e_{L_{cal}} &= (e_L - e_{L_{pedestal}}) \cdot \alpha_{e_L} \cdot \frac{1}{E_{diff}} \cdot E_{sync} \\ e_{R_{cal}} &= (e_R - e_{R_{pedestal}}) \cdot \alpha_{e_R} \cdot E_{diff} \cdot E_{sync} \end{aligned} \tag{5.5}$$

where $e_{L_{cal}}$ and $e_{R_{cal}}$ are the calibrated energies in energy units, e_L and e_R the raw energies in channels, $e_{L_{pedestal}}$ and $e_{R_{pedestal}}$ the pedestal values in channels, α_{e_L} and α_{e_R} the energy-calibration-slope parameters which give the conversion factor of channels to energy units; and E_{diff} and E_{sync} are analogous to T_{diff} and T_{sync}.

In the following subsections, the calibration steps will be presented for the different detectors:

Scintillators S2 and S8 and POS

Those scintillators are formed by a single paddle located in the focal planes of the fragment separator or at the entrance of cave C in the case of POS. They are readout by two (S2, S8) or four (POS) PM tubes each. The

calibration of those is then simple, with a clock signal (called tcal) we can simply convert the channels into nanoseconds, then we just need to adjust the offsets of the PM in order to have the central hit in zero time. No further synchronization is needed. The information we get are relative times, which are very useful to calculate the time of flight of the particles. As all the detectors are synchronised with respect to a common start (POS) the time difference between two of them gives a good measurement of the time of flight that knowing the path length can be easily converted into velocity. The scintillators may also measured energy-loss and thus charge of the particles can be calculated but the resolution is much worse than in the PSP detectors and thus this signal is not used in our case.

The time-of-flight walls (TFW and NTF)

Those are complex detectors composed of several paddles each (TFW 32 and NTF 16) that need to follow the entire calibration process including the paddle synchronization.
Let us briefly go through the different steps:

- TDC gain adjustment: A TDC digitizes the time signals; the ones used for this experiment have a nominal gain of 50 picoseconds per channel, but this value can fluctuate for example due to temperature changes in the electronics, thus, a measurement is done in order to guarantee a good time resolution during the entire experiment. This is done by using a time calibrator module, that simply generates two pulses with known time delay, sending the first to all electronic channels as input, and the second as trigger to the DAQ; this trigger allows to monitor the stability of the TDC gain during the entire experiment.

- Calibration of QDC pedestal: The QDC modules need to be calibrated in order to determine the real origin of the scale. This is done by triggerig the electronics with a clock whenever no signals from the detectors are present. The so-called pedestal is a small internal current distributed to all QDC channels ensuring non-negative energy entries. The mean value of the pedestal distribution is then subtracted in all calibration levels beyond RAW.

- Time and energy synchronization: In order to obtain physical quantities we need to perform two different synchronizations for time and energy: the first one is based on the paddle geometry and concerns only photomultiplier tubes viewing the same paddle.

By using the general definition of calibrated times and energies (equations 5.4 - 5.5) we can calculate the different offsets as it follows:

$$\begin{aligned} \sqrt{\frac{e_{R_{cal}}}{e_{L_{cal}}}} &= \sqrt{\frac{(e_R - e_{R_{pedestal}}) \cdot \alpha_{e_R}}{(e_L - e_{L_{pedestal}}) \cdot \alpha_{e_L}}} \cdot E_{diff} \\ \frac{1}{2}\left(t_{L_{cal}} - t_{R_{cal}}\right) &= \frac{1}{2}\left(t_L \cdot \alpha_{t_L} + T_{L_{cal}} - t_R \cdot \alpha_{t_R} + T_{R_{cal}}\right) + T_{diff} \end{aligned} \tag{5.6}$$

With this, the origin of time ($T = 0$) for every paddle is adjusted to be the time in the center of the paddle. Since the length of the paddles is known, the $diff$ values for time and energy can be obtained by considering the entire distributions, instead of simply shifting the mean values to zero. This method also provides the v_{eff} and λ parameters of equation 5.3.

The second synchronization step is used to adjust the times and energies of all paddles of a given detector to a common level. This calibration procedure requires hits in crossing paddles, which allows their relative time an energy synchronization. For the time offset, the difference of mean times of the two crossing paddles is defined by the distance between the possible interaction vertices in the paddles and by the velocity of the heavy ions. In the case of the energies, the energy loss in the crossing paddles is considered to be equal.
By using the general definition of calibrated times and energies again, one can obtain expressions to calculate the sync offsets:

$$\begin{aligned} \frac{e^{(1)}_{m,cal}}{e^{(2)}_{m,cal}} &= \frac{t^{(1)}_{m,tcal}}{t^{(2)}_{m,tcal}} \cdot \frac{E^{(1)}_{sync}}{E^{(2)}_{sync}} = 1 \\ t^{(1)}_{m,cal} - t^{(2)}_{m,cal} &= t^{(1)}_{m,tcal} - t^{(2)}_{m,tcal} + T^{(1)}_{sync} - T^{(2)}_{sync} = \frac{d}{v} \approx 0 \end{aligned} \tag{5.7}$$

where $t_m = \frac{1}{2}(t_L + t_R)$, $e_m = \sqrt{e_L e_R}$ and the quantities labeled $tcal$ are the calibrated ones i.e. $t_{tcal} = t \cdot \alpha_t + T_{cal}$ and $e_{tcal} = (e - e_{pedestal}) \cdot \alpha_e$, and the labels $^{(1)}$ and $^{(2)}$ note two crossing paddles.

Each crossing provides an equation like 5.7, meaning that we have more equations than needed to get a solution and thus there is not a unique solution. A least-squares minimization will provide a set of optimal *sync* parameters for all the paddles of the detector. As these parameters are not unique a common value can be added or subtracted without modifying the final calibration. Figure 5.1 show the signal of different

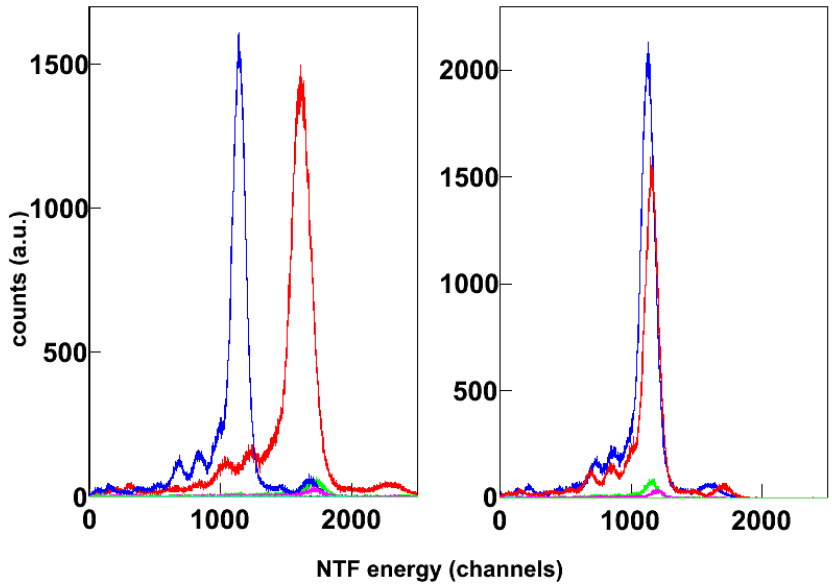

Figure 5.1: Energy signal for different paddles of the NTF before the synchronization was done (left pannel) and after synchronization (right pannel). One can actually see how the peaks are shifted into the same mean value after the calibration is performed

paddles of the NTF before (left) and after (right) the synchronization.

- Monitoring of parameter fluctuations: Data are usually recorded during long periods and some times the calibration parameters fluctuate due to electronic noise, temperature variations or detector defects. The `land02` program calculates the calibration parameters for a group of files together; in this case we used groups of 5 files in order to have good statistics. Dominic Rossi has implemented a set of programs to cross-check and monitor the parameter fluctuations during the experiment. The entire procedure is explained in detail in his phD thesis [Ros08]. It mainly plots the calibration parameters versus the file numbers and takes the average. Wherever there is a big jump it applies a different parameter.`land02` has a function called `LT_RANGE` which allows to apply different calibration parameters to different ranges of lmd files. In Fig. 5.2 the monitorization of the fluctuations of the time offset calibration parameter for one of the paddles of the NTF is represented. One can clearly see three different regions, thus, three calibration parameters are taken and applied for each range.

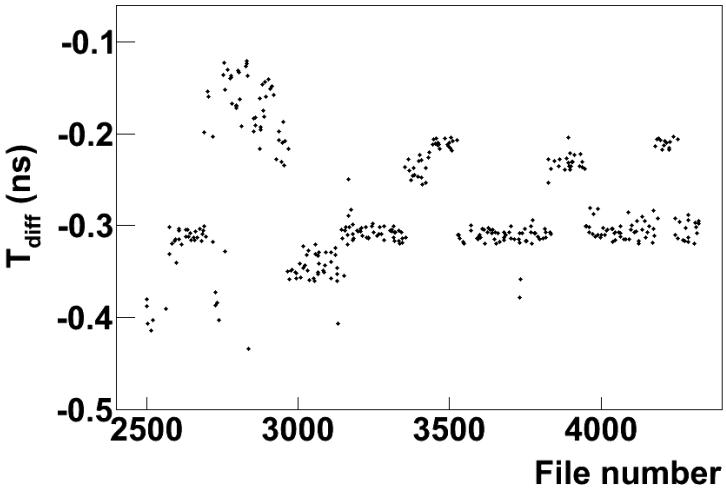

Figure 5.2: Example of monitorization of a calibration parameter of one paddle of the NTF

5.2.2. Crystal Ball

For the calibration of this array of crystals several sources were used prior to the experiment. In a first step all crystals are calibrated independently to the known peaks of the sources. In figures 5.3 and 5.4 the calibration for a ^{60}Co and a ^{22}Na sources is shown. The peaks are fit and then the gainmatch and offsets are adjusted to give the nominal energy to the centroid of the peak.
The problematic part, however is the synchronisation of all crystals, for that purpose, addback routines are developed. In this step the program looks for clusters belonging to the same gamma emission and adds them all.
A last step is the Lorentz boost and Dopler correction that is applied to the energy values.

5.2.3. Silicon detectors

Silicon Strip Detectors (SSD)

For this experiment we used only the forward SSD for tracking purposes. As any other detector it is calibrated in different steps: the raw level contains information of energy deposition strip-by-strip, each of them individually readout. In total 1024 energy channels.

The sync level runs a pedestal subtraction for every strip and afterwards

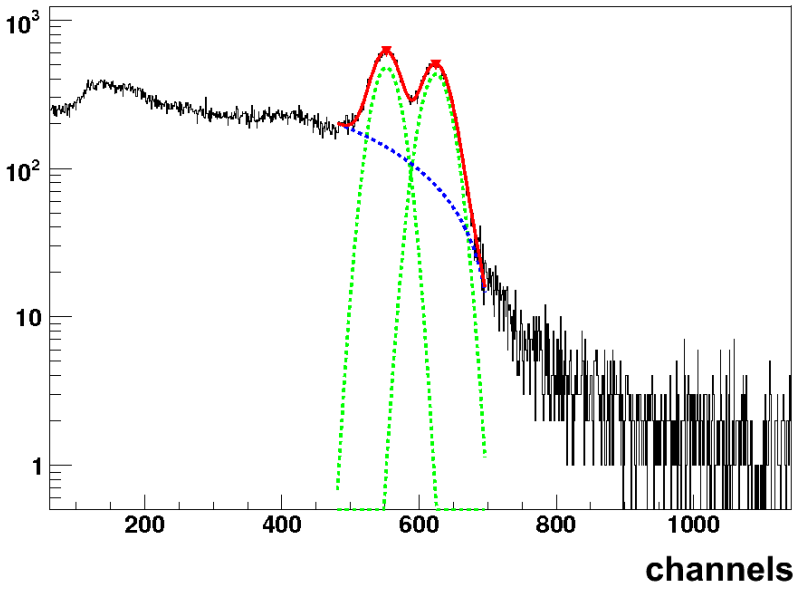

Figure 5.3: Calibration of one crystal using a ^{60}Co source

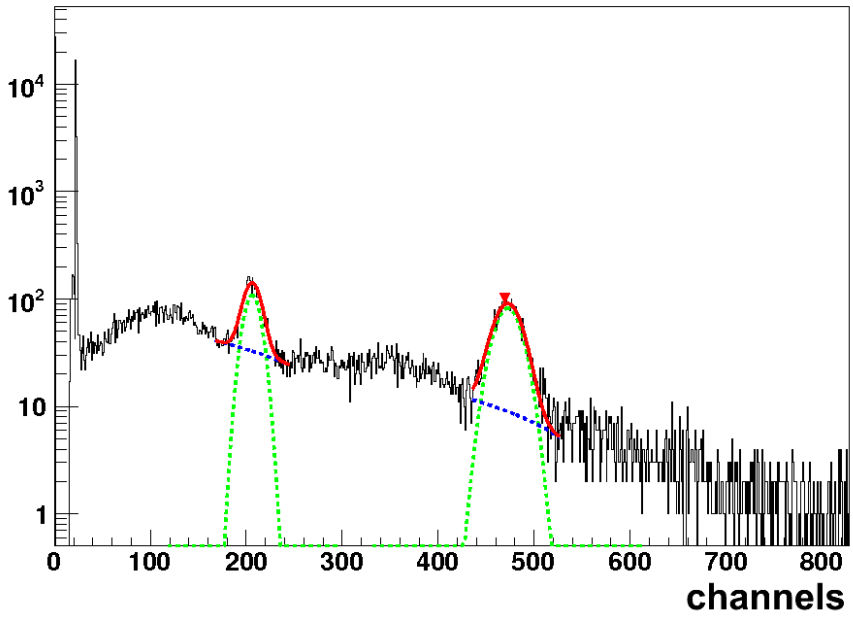

Figure 5.4: Calibration of one crystal using a ^{22}Na source

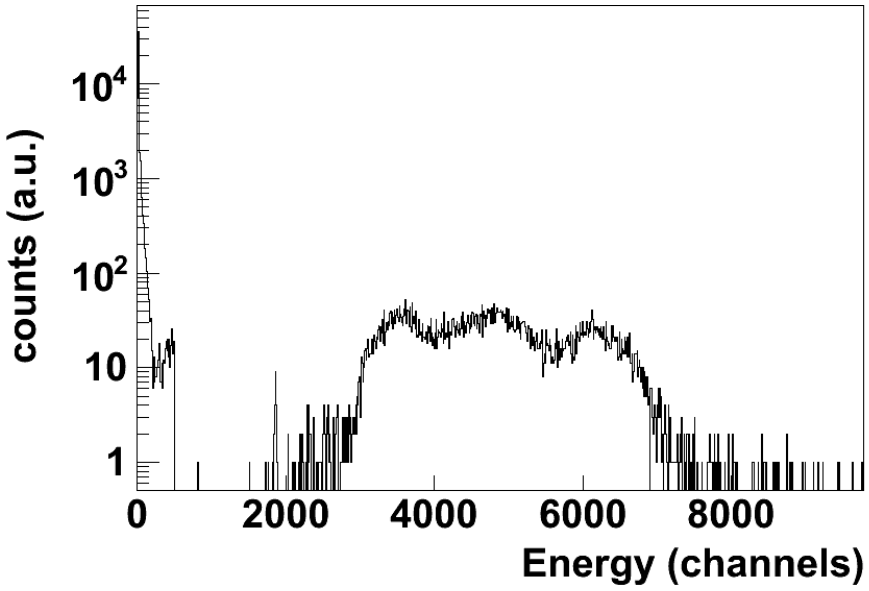

Figure 5.5: Typical energy spectrum of a SSD in a breakup reaction. The peak at low energy is the proton in this case and the bump at high energies is for the heavy ion.

a reconstruction of the baseline for each block of 64 channels is reconstructed when shifted. In this level it is also performed the gain adjustment for each block. At the same time a zero suppression is also done, keeping only clusters with an energy deposition larger than 4σ surrounded by neighbouring strips with energy larger than at least σ.
In the DHIT level the calibration routine searches clusters and analyses them in order to extract the position centroid,, energy, area, number or strips in the cluster and eta.
The last step, the HIT level converts the positions into x and y coordinates with origin in the center of the detector.
In figure 5.5 a typical energy spectrum of a SSD is represented. The peak at low energy is the proton in this case and the bump at high energies is for the heavy ion. In order to be able to distinguish the heavy ion and the proton it is mandatory to have at least one empty strip between both clusters, otherwise it will be identified as a unique cluster and the centroid position will not be correct.

Position Sensitive Silicon pin diode (PSP)

The PSP are used for position and energy loss measurements.
For the position calibration, each PSP detector is equipped with an additional active mask as described in chapter 4.3.1. During the experiment so-called "pixel runs" are performed in order to collect calibration data for the PSPs. The pixel masks are inserted in the beam line, ahead the PSP's, only during these calibration runs.

Each time a particle passes through one of the scintillating pixels, it produces light that is guided to a PM tube and triggering on these events the "pixel" on, one can afterwards select an "image" of this pixel mask on the PSP's.
The resulting two-dimensional position spectrum from the PSP looks as presented in Fig. 5.6 (picture on the right). The clusters of events are formed as a "shadow" of the beam through the pixel mask and are expected to be sitting on an orthogonal grid, as follows from the pixel mask geometry. A routine written by Stefanos Paschalis [Pas08] allows to associate every cluster to an index (k,l) in the orthogonal grid. However, we see that in the internal coordinate space of the PSP, due to non-linearities, the image is distorted.

The PSP measures the position in internal coordinates (let us call them (u,v)) that need to be related to the external coordinates (x,y) with the help of the mask. Since each pixel position has been associated to a (k,l) pair and thus to a (x,y) real position, it is possible to draw two 2D graphs with sets of (u,v,x) or (u,v,y) points. The fit of a 2D function to these data-points provides a continuous transformation that can be used to calculate from any measured (u,v) point its corresponding real (x,y) one. Two 2D polynomials, from third to fifth order depending on the distortion, are used to fit the data. By performing a χ^2 minimisation on all pixel positions, the parameters of these functions are determined. Applying this calibration parameters allows to get the desired position in the PSP like in Fig. 5.6 (picture on the left).

During the experiment there can be drifts in the response of the detectors, thus several pixel runs are performed to crosscheck the stability of the calibration parameters.

The energy loss is measured directly at the cathode. With the energy loss measurement of a known beam at different known energies, a slope and offset can be obtain relating this measurement with the charge of the particle by using the Bethe-Bloch formula [Bet30]. If the detector response would be homogeneous, it would not mind the interaction point inside the active are,

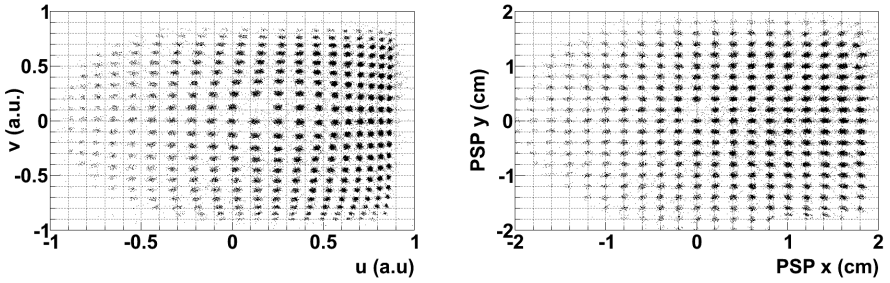

Figure 5.6: PSP signal in coincidence with PIXEL before position calibration (left picture) and after calibration (right picture). One can clearly see the distortion of the clusters in the first picture but after the calibration every cluster stands in the center of a grid intersection.

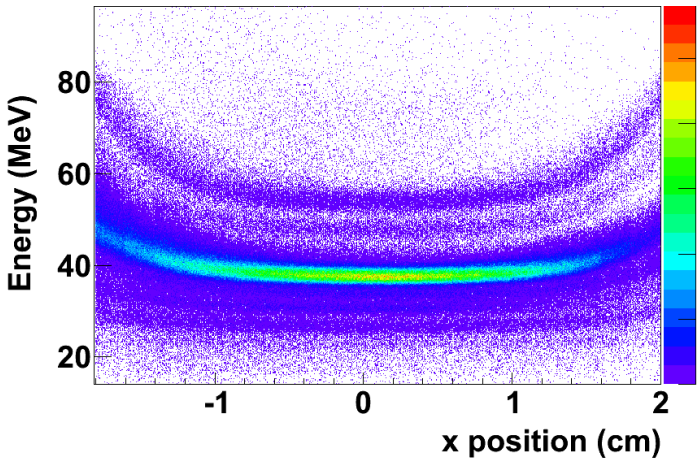

Figure 5.7: Position dependence of the energy in the PSP

nevertheless during the experiment we realised that there was a dependency of the energy with the position in the PSP (see Fig. 5.7). A two-dimensional fit is done which is used to correct for this effect and corrects drifts in the charge identification.

5.2.4. Große Fiberdetektor (GFI)

GFI fibres are coupled to the photocathode of a position sensitive photomultiplier tube (PSPM) with the use of a mask, which has holes arranged in a well-known geometry.
A hit in the detector produces light which is guided through the fibres and causes a well-defined light spot on the photocathode. An electrical signal

is then developed in some of the 18×16 anode wires, depending on the 2D position of the light spot on the photocathode. By combining information from these signals, it is possible to precisely reconstruct the position of the light spot on the photocathode and thus identify the hit fibre.
As for the PSP, the GFI has internal coordinates so-called (u,v) which need to be converted into a usual system in (x,y).

However, the amplitude of the signals depends on their amplification, which is in general different for each case, and also depends on their position on the photocathode of the PSPM. Thus, it is essential to properly gainmatch all the anode wires before proceeding with the position reconstruction of the hit.

It is in general expected that the charge distribution of a typical hit will produce electrical signals in about seven neighbouring wires in each (u,v) direction and that their amplitudes will exhibit a Gaussian-like shape. This expected Gaussian-like shape of the distribution can be used to gainmatch the wires, requiring all signals from neighbouring wires to fit in this distribution [Mah09]. This gainmatching is possible if we iluminate completely the detector (sweep run) by varying the field of the ALADIN magnet.

Once the gainmatching is performed, the mean position of the charge distribution for each hit gives the u and v coordinates of the light spot. For a typical sweep run all the light spots, which correspond to fibres, are reconstructed properly.

At this stage a method similar to the one used for PSP is used to find the (u,v) position of each dot (cluster), associate, index and assign them the corresponding fibre.

After the position (u,v) of each fibre on the mask has been found and indexed (k,l), as in the case of the PSP, a transformation is needed to send any point of the uv space to the corresponding x position.
In the case of the GFI, however, the reconstruction of the x position of the hit is not a continuous transformation of the uv space, since each point has to be related to a discrete fibre. If for a hit in the detector the point (u, v) on the mask is within the width of a cluster, the assignment is trivial, but for points lying between the clusters there are more than one candidate fibres. To reconstruct the x position, either a decision has to be made choosing the fibre closest to the hit or even better it can be calculated as a weighted average of the candidate fibres.

5.2.5. Drift chambers

The Drift Chambers (DCH) provide position measurements with high resolution. A good description on how to work with the DCH is in C. Wimmer's phD thesis.(REFERENCIA) To get the position from the DCH we need to determine the dependence between drift time and drift length (the so-called rt-curve). We assume that all positions between adjacent sense wires, x_i and x_{i+1}, have the same probability to occur. The correct rt-curve converts the measured drift time distribution to a rectangular box-like distribution of drift lengths between 0 mm and the cell size of 6.92mm. Some quality requirements are made to have only good data from real events contributing to the calibration: first, the area illuminated with particles has to be compared to the cell size to ensure all drift lengths are equally occupied; in addition, particles have to pass the detector close to its normal plane. Further, it is required that hits occur in two adjacent cells so that we can define the distance of the hit from the center of the cell (r_1 and r_2 for the first and second cell respectively). A preliminary rt-assignment is included in the calibration file, allowing an approximate value for r_1 and r_2 to be calculated (see chapter 4, fig. 4.10). If their sum is near their optimal value of 6.92mm an event is taken into account for this assignment. The start-time-distribution is folded with a function varied until the result is a rectangle of 0.692 cm length.
The procedure is implemented within the `land02` program and it is automatically performed with every unpack; the calculated values are afterwards applied in order to get the position information.

As this experiment was also the first usage of DCH, prior to it a pure proton parasitic beam was used to calibrate and study the performance of these detectors. This information proved to be very useful for the position calibration of the chambers in the setup and also to test the R3BSim simulation package (see chapter 6) and the tracker (described later in this chapter).
A beam of protons with seven different energies around 500 MeV were used (460 MeV, 480 MeV, 490 MeV, 500 MeV, 510 MeV, 520 MeV and 540 MeV). The nominal magnetic field value of the ALADIN magnet was 1782.5 A.

5.2.6. TRACK level calibrations

Once the detectors are individually calibrated we can proceed to combine the information to get the physics observables. In some cases general adjustments must be done.

Regarding time of flight determination for instance, a global start time must be fixed: in this case the signal originated in POS is considered the start for the time signals ($T0$) and therefore no offsets are added to the time measured in this detector since this would modify timing properties of all detectors as they take POS as a reference. The offsets are then fixed in the other detectors. This has to be done for the incoming fragments as well as for the outgoing ones after the reaction.

For the outgoing, the NTF charged fragment velocities must be measured. Using known ions the time of flight between POS and NTF can be estimated by using for example the code ATIMA [ATI] which calculates the energy loss in the different layers. With this information, the time synchronization can be done and thus, this time-of-flight can be used to calculate the mass over charge ratio for the different fragments. The NTF also allows energy loss measurements, and by using the code ATIMA again and the Bethe-Bloch formula the charge of the particles can be estimated, providing a complete identification of the different fragments.

Special interest has the calibration of the incoming ions as it plays a crucial role in the selection of the reaction channel, and also the calculation of the interaction point in target and the incoming angle.

Incoming identification

In order to identify the incoming ions one needs to calculate the charge and mass of the nuclei. For that purpose a good measurement of the incident velocity is needed: the ratio A/Z of an ion passing through a constant magnetic field B can be determined by using the equation:

$$A/Z = \frac{e}{uc}\frac{B\rho}{\beta\gamma} \tag{5.8}$$

being e the charge of the electron, u the atomic mass unit and c the speed of light.
Thus, it is required to measure the velocity of the ion and its magnetic rigidity ($B\rho$). The velocity is obtained through time-of-flight measurements (ToF) and known paths (S) as follows:

$$\beta = \frac{S}{(ToF)\cdot c} \tag{5.9}$$

where c is the speed of light. To get, however, time-of-flight measurements from the time measured by the detectors, the time signals need to be synchronised with each other. The paths and offsets (T_{offset}) are determined

using the following method: The measured time difference (δt) is:

$$\delta t = ToF + T_{offset} \tag{5.10}$$

Combining Eqs. 5.9 and 5.10 the following expressions are derived:

$$\begin{aligned} \beta &= \frac{S}{(\delta t - T_{offset}) \cdot c}, \\ \beta\delta t - \beta T_{offset} &= \frac{S}{c}, \\ \beta\delta t &= \frac{S}{c} + \beta T_{offset} \end{aligned} \tag{5.11}$$

From Eq. 5.11 it is clear that by plotting $\beta\delta t$ versus β for different known beam velocities (β=0.7144, 0.76211, 0.76369) and performing a linear fit, the flight path is obtained from the offset of the linear fit (times the speed of light) and the time offset (due to cabling, etc.) is obtained from the slope of the linear fit, as illustrated in Fig. 5.8

The velocity calibration is usually performed using runs with primary beam at different beam energies (i.e. velocities). In this experiment a ^{36}Ar beam with three different energies around 418.3, 517 and 615.5 MeV/nucleon (and well-known corresponding magnetic rigidities $B\rho$) has been used. The velocity β can then be precisely determined from the $B\rho$ value given by the FRS setting. The offset of the linear fit, which gives the flight path, needs to be inserted as an experiment-specific geometrical parameter and thus it is not allowed to be adjusted during the experiment. The synchronisation offset that is found (i.e. slope of the linear fit) is applied for the whole detector (e.g. all channels). With this a precise velocity calibration is obtained.

To get the A/Z ration we still need to measure the $B\rho$ value:
The nominal magnetic rigidity ($B\rho_0$) is obtained from the settings of the FRS magnets. An ion of charge Z_0 and momentum P_0 that travels in the central trajectory (reference trajectory) of the FRS setting satisfies the following equation:

$$\frac{P_0}{Z} = B\rho_0 \tag{5.12}$$

Ions, however, that travel through the FRS magnets with a trajectory that deviates from the reference trajectory have a different momentum-over-charge ratio and thus, for Eq. 5.12 to be valid, a different magnetic rigidity ($B\rho$). To determine for each ion the deviation of its magnetic rigidity from the reference magnetic rigidity, position measurements at the dispersive (F2) and

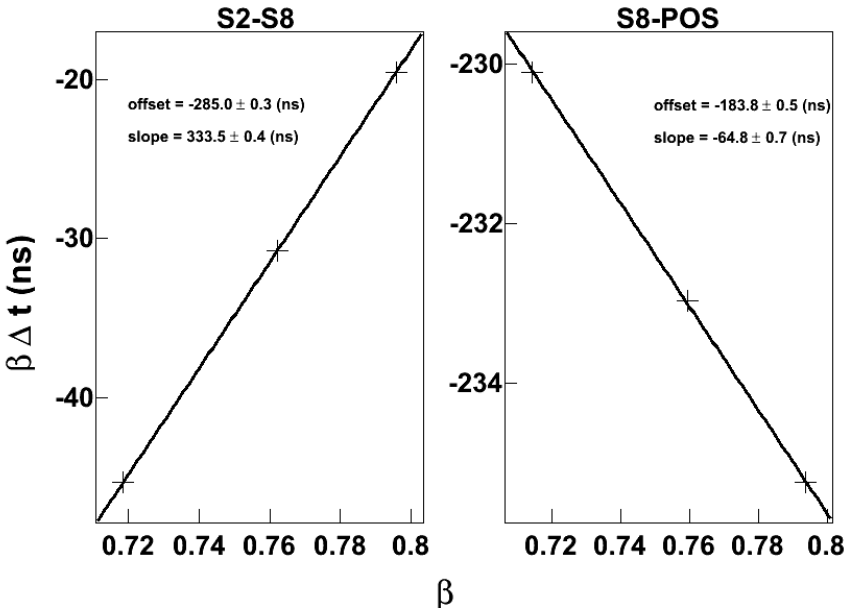

Figure 5.8: Linear fit of time-of-flight multiplied by β versus β for the 3 known energies. The offset multiplied by the speed of light gives the flight path and the slope gives information of time offsets due to electronics. The picture on the left corresponds to the flying path from S2 to S8 and the one on the right from S8 to POS

achromatic (F8) planes of the spectrometer are required using the S2 and S8 scintillators. The magnetic rigidity for each ion is then calculated by the equation:

$$B\rho = B\rho_0 \cdot \left(1 - \frac{X_{s8} - M \cdot X_{s2}}{D_8 \cdot 100}\right) \tag{5.13}$$

where M is the magnification of the achromatic system, $M = -X_{s8}/X_{s2}$, and D_2 and D_8 are the dispersions at the focal planes F2 and F8, respectively. In the case where the beam is centred at S8 ($X_{S8} = 0$), Eq. 5.13 can be simplified as follows

$$B\rho = B\rho_0 \cdot \left(1 + \frac{X_{s2}}{-D_2 \cdot 100}\right) \tag{5.14}$$

Using the measured velocity and magnetic rigidity of the ion in Eq. 5.8, the mass- over-charge ratio is obtained with a precision better than 0.2% for secondary beams. In this experiment the secondary fragments have mass and charge around $A \approx 27$ and $Z \approx 15$, respectively. In other words, the difference in the mass-over-charge ratio for isotopes with neighbouring masses is around 1.5%, which means that the resolving power of the spectrometer should be better than 0.5% in order to safely distinguish them. It is evident from the aforementioned estimates that the high resolving power of the FRS spectrometer allows for an unambiguous mass identification of nuclides in this mass region.
The charge is directly calculated in the PSP as explained before in this chapter. With all this we can get identification plots such as the one in Fig. 5.9

Position and angle on target

The tracking of the projectile on target, i.e. finding the position and the angle on target, requires at least two 2D position measurements before and close to the target, which are provided by the PSP1 and PSP2 detectors which are 1.22 m appart. The position and the angle on target is found simply by extrapolating the line defined by each pair of points (one in PSP1 and one in PSP2) to the target position. If an ion is moving along a straight line and hits the position sensitive silicon detectors (PSP1 and PSP2) at points $\vec{r_1}(x_1, y_1, z_1)$ and $\vec{r_2}(x_2, y_2, z_2)$, respectively, its coordinates $\vec{r}(x, y, z)$ should satisfy the following equation

$$\vec{r} = \vec{r_1} + (\vec{r_2} - \vec{r_1})t,\ t \in \mathbb{R} \tag{5.15}$$

or the symmetric equation of line

$$\frac{x - x_1}{x_2 - x_1} = \frac{y - y_1}{y_2 - y_1} = \frac{y - y_1}{y_2 - y_1} \tag{5.16}$$

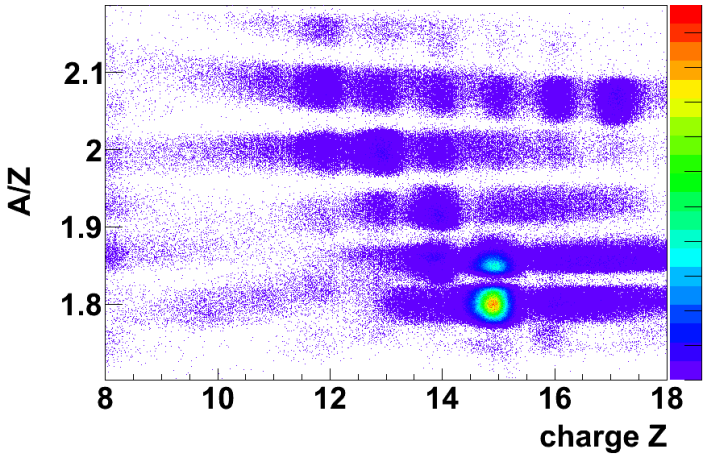

Figure 5.9: Identification plot of the incoming being after calibration. The y axis represents the mass over charge ratio and the x axis the charge of the different incoming species

which shows that if any of the x, y, z is known, the other two can be calculated. By considering that the target position (Z_0) is known, it is trivial to calculate the extrapolated (X_0 , Y_0) coordinates.
The position measurement from PSP1 and PSP2 detectors define the incoming angle, while the extrapolated position on target (fig. 5.10)

$$\theta_0 = \frac{x_2 - x_1}{z_2 - z_1} \tag{5.17}$$

In reality, the incoming angle at the target position (θ_0) is affected by the straggling in the PSP2 material θ_{str} and has to be accounted for

$$\theta_0 = \frac{x_2 - x_1}{z_2 - z_1} + \theta_{str}^{PSP2} \tag{5.18}$$

where θ_{str} is a Gaussian distribution, centered at zero with a standard deviation σ_{str}.

5.2.7. Tracking through ALADIN: momentum determination

Once the projectiles and fragments are identified, the ultimate goal of the tracking routine is to determine, once the reaction takes place at the target, the fragment and proton momentum.

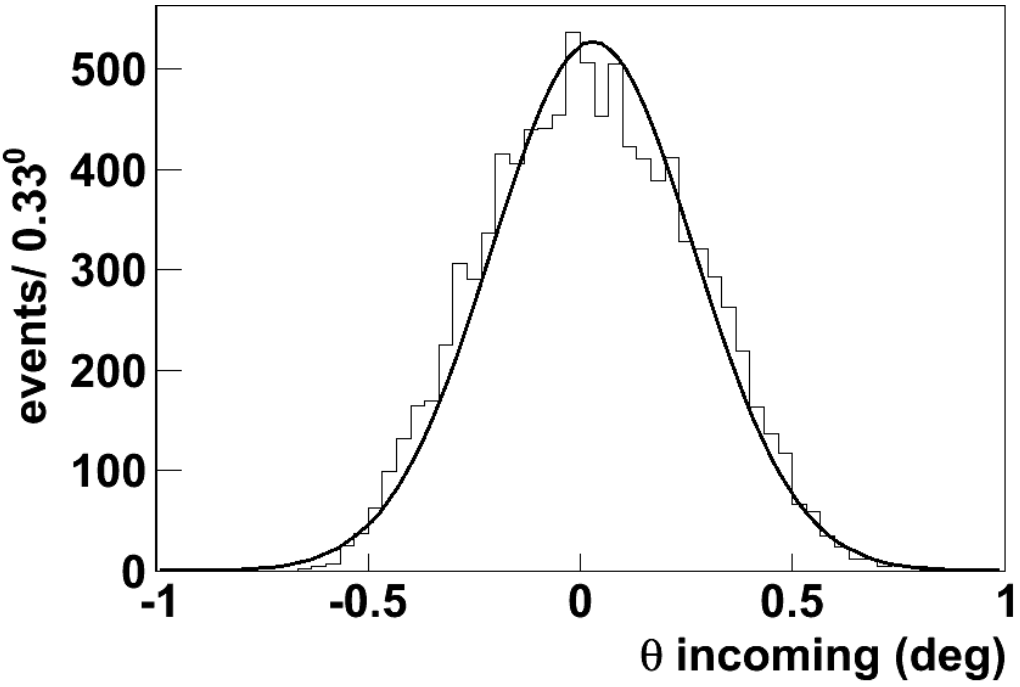

Figure 5.10: Incoming angle aperture for the present experiment

The field description of the Aladin magnet is achieved by the use of measured field maps for different settings of Aladin current (0, 500A, 1100A, 1300A, 1500A, 1700A, 1900A, 2100A, 2300A, 2500A). For values in between the measured ones an interpolated value is used. This interpolation is done by a linear rescale of the magnetic field value between the previous and following measured field map. The goal is to identify for each set of trajectories (root file containing hitlevel data for all detectors) the corresponding ^{26}Si and proton momentum. To select the reaction channel we need to apply several conditions: general reaction and good beam trigger; selection of reaction channel (i.e. incoming ^{27}P and outgoing charge Z=14 for Si in NTF in coincidence); proton multiplicity one in both DCH and TFW; valid GFI's and SSD hit.

From the larger declination angle of the proton arm with respect to the fragment arm (7 and 21 degrees) one can see that all fragments besides protons are too rigid to be bent into the DCHs. However, there is often more than one proton detected. This is believed to come from unspecific reactions of fragments in the GFIs or in the air. A condition on correlation between the x positions of DCH1 and DCH2, respectively for y positions, can be required.

Tracking of heavy ion fragment

In a first step the mass over charge ratio (A/Z) for the fragment is determined but as the charge (Z) is also measured in the NTF we can infere the mass (A). The A/Z ratio is determined by the $B\rho$ of the fragment of known velocity β which is accordingly deflected by the magnetic field of ALADIN. The direction of the fragment after the magnet is defined by position information in the Large Area Fiber detectors (GFI1 and GFI2). The position resolution of the NTF (5 cm) is inferior to the one of the GFIs (0.1mm), thus, the track is fully determined by the position of the GFIs. The value of β is calculated from the time-of-flight from target (T0) to NTF and the length of the flight path. With this β the vector connecting the measured positions in the GFIs is tracked backwards through the magnet by applying a Runge-Kutta iteration method. The mass (A) is varied until the track meets the measured position on the SSD before the magnet, being the one that allows the best fit. The trajectory is checked for consistency with the position information of the NTF. The reconstructed position of this track at the target is afterwards set as "interaction position", where the reaction took place, and used for tracking the proton.

The magnetic rigidity is related to the velocity of the fragment and its mass over charge ratio as in the following equation:

$$B\rho = \beta\frac{A}{Z} \tag{5.19}$$

For the momentum reconstruction, the mass identified by the tracking is rounded to an integer and the accurate mass looked up in standard tables to be used for futher calculations. The division of the momentum into x, y and z components is derived from the direction of the trajectory at the target. The momentum component in x direction is known with good precision since the track is defined by the position measurement of the GFIs. The y component of the track is only determined by the measured y position on the NTF. The component in z is derived from the time of flight.

For a first calibration of the heavy ion fragment tracker a beam of ^{27}P at 500 AMeV was used. This primary beam run helps as well in the estimation of the resolution of the procedure. In fig. 5.11 a picture of the reconstructed momentum for the selected ^{27}P beam is represented, being the resolution in this case $\Delta p/p = 0.74\%$. For the Coulomb dissociation events the result we got can be seen in figure 5.12.

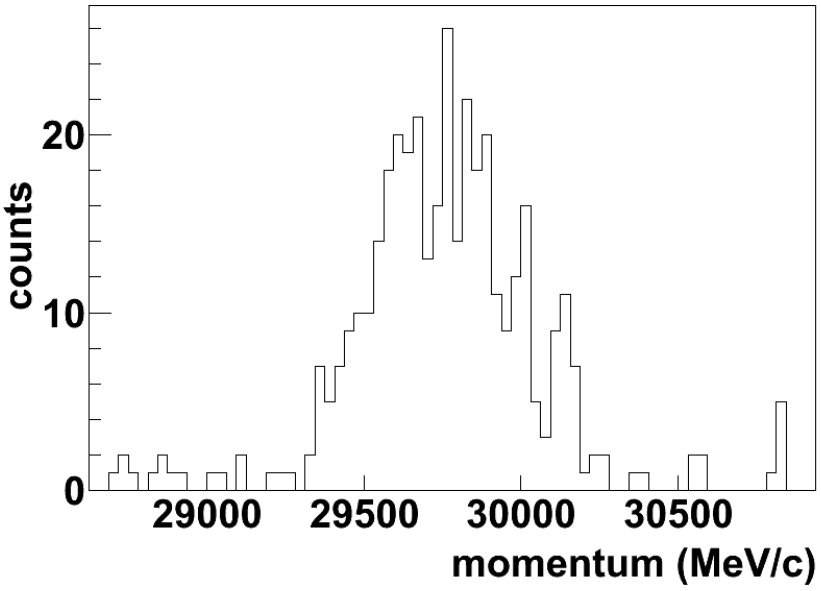

Figure 5.11: Reconstructed momentum for a selected beam of ^{27}P at 500 AMeV

Tracking of Proton

The trajectory after the magnetic field is defined by a straight line given by the hits in the DCHs. If a corresponding signal is found on the TFW in the vicinity of the prolonged connecting vector given by the two DCHs it is kept as a valid hit for tracking. For the protons, the plausability check is more important due to the relative high multiplicity. As A and Z of the proton are known only β in equation 5.19 has to be varied until the track meets the position on the target.

As said before, to propperly calibrate the tracker for protons, a beam of pure protons at seven different energies was used. In 5.13 the calculated momentum for protons corresponding to energies of 460, 500 and 540 MeV is represented. For the 500 MeV case, which is the nominal energy value used in the experiment, the obtained resolution for the momentum by using the tracker is $\Delta p/p = 0.46\%$ In figure 5.14 the reconstructed momentum for the protons coming from the Coulomb dissociation of the ^{27}P can be seen.

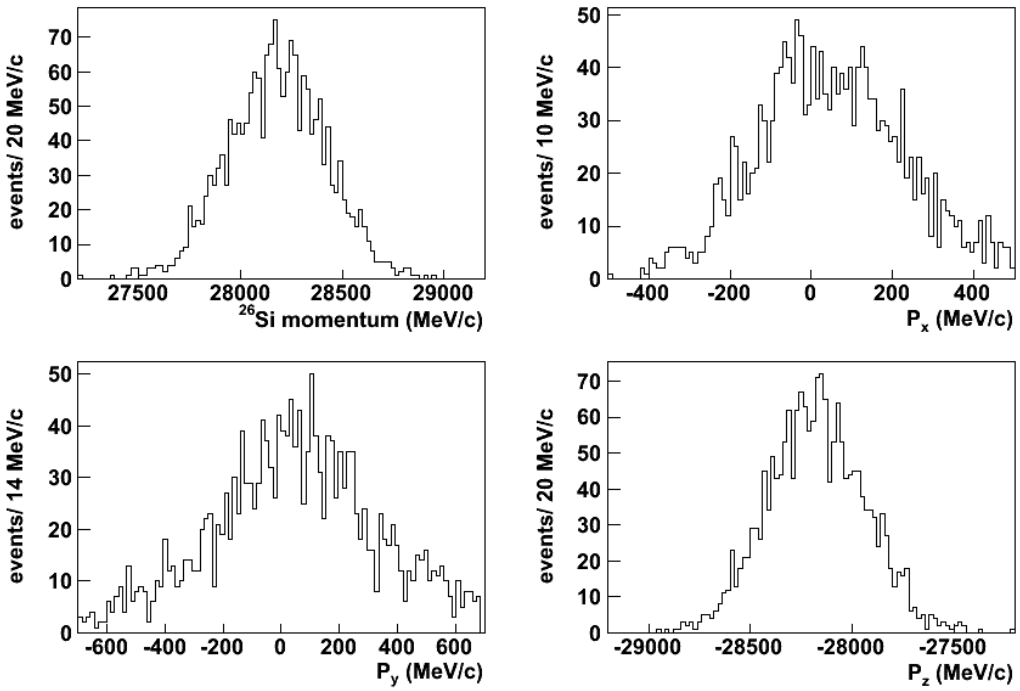

Figure 5.12: Reconstructed momentum for the heavy fragments (^{26}Si). The first image shows the module of the vector. The other three are the cartesian components.

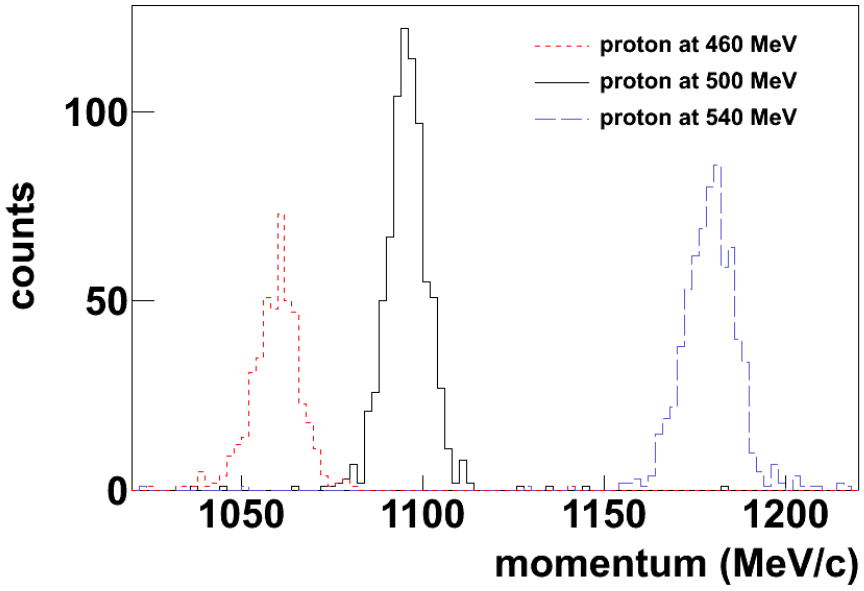

Figure 5.13: Momentum calculated for a pure beam of protons using the tracker. It is represented for protons of 460, 500 and 540 MeV

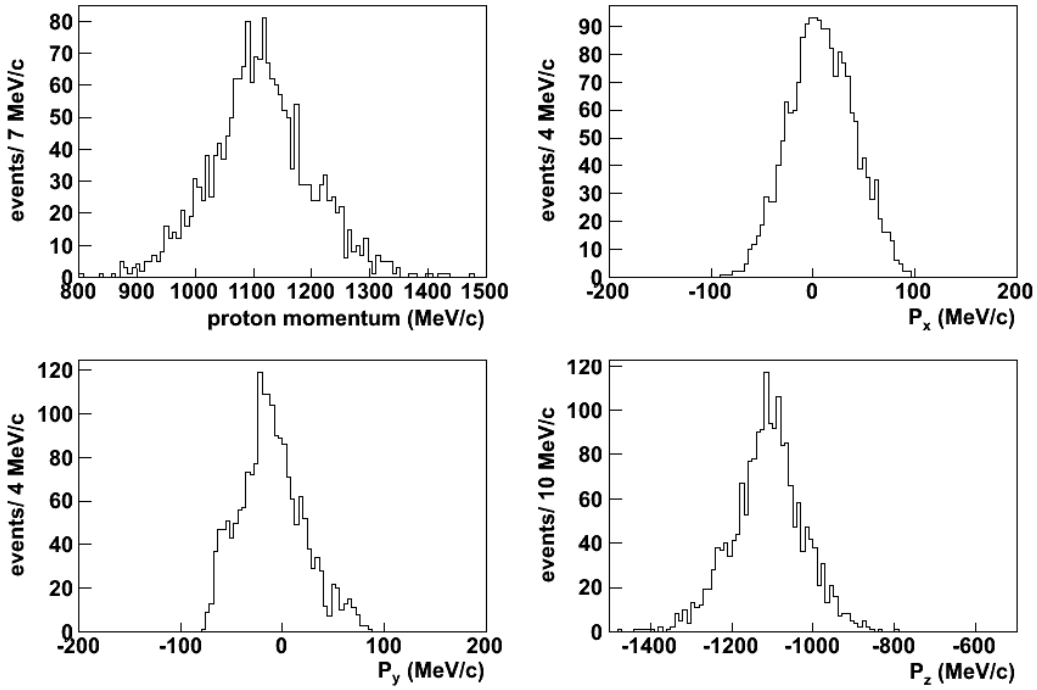

Figure 5.14: Reconstructed momentum for the protons. The first image shows the module of the vector. The other three are the cartesian components.

Chapter 6

Simulation: R3BSim

R3BSim is a simulation code particularly developed for the future R3B setup at FAIR. R3BSim is a pure GEANT4 (G4)-ROOT program that features a multihit data structure ready for event analysis and a modular geometry description that allows the integration of new detectors.

6.1. Simulation package

In the R3BSim code most of the R3B detectors are implemented. The version used for this work includes the present ALADIN-LAND setup at Cave C (GSI) (detailed description in next section). The program is written in C++; ROOT libraries are included allowing a fully integrated analysis interface: all the detectors are in a single TTree with individual branches for every detector, each one made of collections of detector hits (TClonesArray).

The simulation includes a large set of materials for the detectors and the environment that can be easily exchanged when needed. It has a messenger for users that allows to do important changes in the configuration during the execution of the program (no need to recompile).

Regarding the physical processes, G4 allows and enforces a full customization of the physics description, providing different physics lists that can be chosen by the user, for electromagnetic processes, hadronic, etc (see appendix for an example of a physics list).

Once we have a realistic description of the experimental setup and the physics, we need to simulate the incoming particles or beam. For that purpose, different event generators are available, like for instance single particles

(protons, neutrons, gammas...) at different conditions (initial point, direction, energy...). Other more complicated generators are being developed, in particular in this work we have used one based on theoretical calculations for the Coulomb dissociation of ^{27}P [Typ07]. The information is introduced in the form of a data file containing the momentum components for the ^{26}Si and the proton for a huge number of simulated C.D. events.

The different steps performed during the simulation process include:

- The starting point of the simulation (from where the particles are launched) defines the primary vertex. From that point, every particle is tracked during its flight.
- The simulation calculates the new energy and direction after each step. The step length is defined internally by the program taking into account the energy of the particle and the material that is crossing.
- The particles pass through the detectors leaving a signal that is recorded there. This information is processed in an event by event basis.
- All the recorded information is collected for thousand of events altogether. Afterwards we manage to access this information and reconstruct all the hits doing iterations with analysis algorythms. This last step is done externally.

6.2. Validation of energy loss measurements in GEANT4

To validate the internal G4 (version 4.9.1p01 in this case) energy loss calculation we have performed a simple simulation covering different ions ranging from H to U at different energies impinging different materials. This simulation includes a simple 1 cm^2 square box located inside a vacuum volume. The results are compared to experimental data.

All the simulated processes have been compared to experimental values in a quite broad energetic regime and different ions ranging from B to Pb. In figure 6.1 we plot the the percetual difference between G4 stopping power evaluation and experimental data for all the studied targets. We can observe that most of the experimental and simulated values are in close agreement in our energy regime (around 500 MeV).

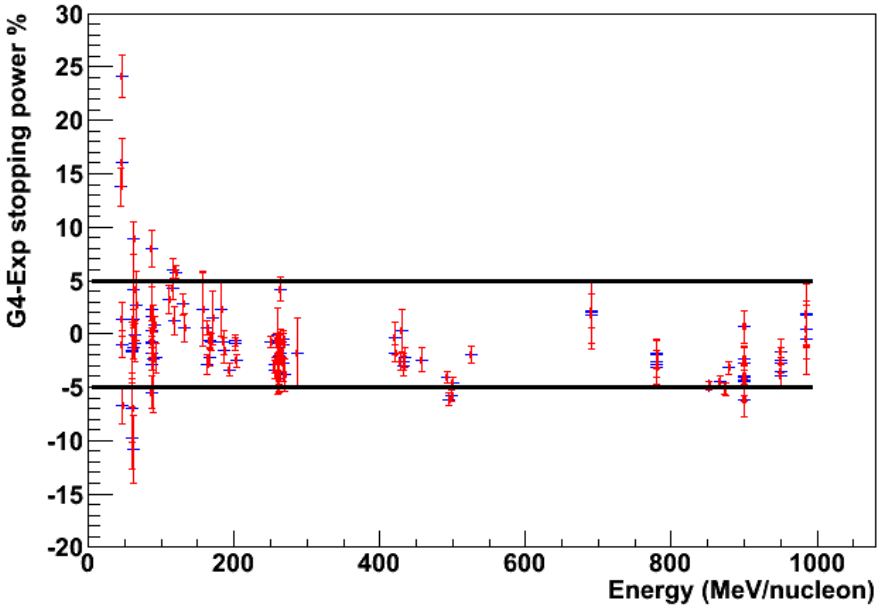

Figure 6.1: Percentual difference between experimental and calculated by G4 stopping power as a function of the incident ion energy per nucleon.

6.3. Application to the current setup at cave C (GSI)

As said before, R3BSim package can also be used for the current ALADIN-LAND setup placed in Cave C at GSI. In figure 6.2 we show the whole ALADIN-LAND setup as it was used for Coulomb dissociation (CD) of ^{27}P in a ^{26}Si and a proton (experiment S223, GSI, May 2007). In next section we briefly describe the different detectors that are included in the simulation and used to extract conclusions about the geometrical efficiency and momentum reconstruction resolution for the different reaction fragments.

6.3.1. Implementation of the setup in the simulation

Following figure 6.2 the experimental setup includes:

1. An incoming vacuum pipe which goes up to the entrance of the magnet, with a 250 μm iron exit window. This pipe follows the beam direction, this is z axis.

2. Within the vacuum pipe, there is a Pb target, where the C.D. reaction

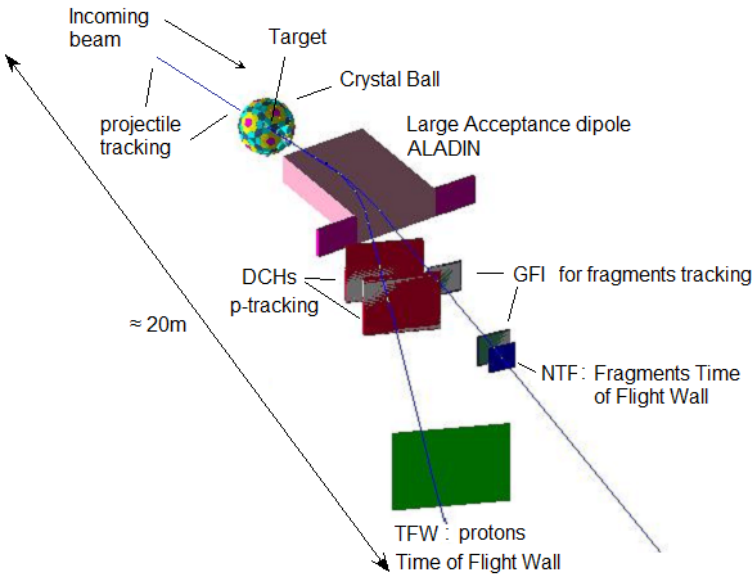

Figure 6.2: ALADIN-LAND experimental setup configuration for ^{27}P C.D.

takes place. The thickness of the target can be easily exchanged while running the simulation.

3. Behind the target we have a silicon multistrip detector (SSD) in order to measure the (x, y) position of the produced fragments. The characteristics of the detector are summarized in table 6.1.

Active area $x \times y$ (cm)	$7. \times 4.$
Media	Si
Thickness (cm), (mg/cm^2)	0.03, 69.9
Spatial resolution, σ (cm)	0.003

Table 6.1: Characteristics of the silicon multistrip detector used in the ^{27}P C.D. experiment

4. After that we simulate the gap of the ALADIN dipole ($155. \times 50. \times 230.$ cm) filled with He in order to reduce the angular straggling and rotated 7.2 degrees with respect to beamline. The iron constrains of the magnet have been also included in the simulation.

5. We have also considered two different branches for the two CD fragments, composed by tracking detectors and a TOF wall. They follow respectively the trajectories of the ^{26}Si ions and protons. The first one is rotated 16 *deg* respect to the z axis of the beamline and the second one, 32 *deg*.

6. The tracking detectors placed after the magnet are two fiber detectors (GFI) for the ^{26}Si ions and two drift chambers (DCH) for the protons. Their characteristics are given in tables 6.2 and 6.3.
   We have also included Al frames for these detectors and two 12 μm

Active area $x \times y$ (cm)	$50. \times 50.$
Media	$Scintillator\ plastic\ C_9H_{10}$
Thickness (cm), (mg/cm^2)	0.1, 103.2
Spatial resolution, σ (cm)	0.1

Table 6.2: Characteristics of the GFI detectors used in the ^{27}P C.D. experiment.

Active area $x \times y$ (cm)	102.8×80.4
Media	$50\%\ Ar + 50\%\ C_2H_6$
Thickness (cm), (mg/cm^2)	8., 8.
Spatial resolution, σ (cm)	0.02

Table 6.3: Characteristics of the drift chambers used in the ^{27}P C.D. experiment.

   mylar layers for each DHC, limiting the active volume. The drift chambers for protons are placed as close as posible to the magnet in order to optimise the geometric efficiency.

7. Finally, two TOF detectors have been included. The TOF wall for the protons will be used in the experiment only as trigger whereas the one for the ^{26}Si will provide an aditional identification of the ions by measuring their velocities. In principle, the identification of the ^{26}Si

ions will be done by means of the energy loss in the silicon detector, but as this measurement is not expected to be accurate enough, they will be also identified using the TOF technique.

All the detectors are placed in a "world" volume filled with air. Every position, size, and material can be easily exchange within the simulation without even recompiling using a Messenger routine that is implemented, so the setup can be easily adapted for any experiment.
The response of the detectors is simulated in a simple way: when a hit takes place in one detector the position, energy or time signal is recorded. Then we apply a Gaussian random around the mean value taking into account the precision of the detector. The signals are then recorded into a root tree that can be analysed in the same way as a real experiment.

6.3.2. Magnetic field of the ALADIN dipole

In this work we are using ALADIN magnetic field, which comes from experimental maps measured at GSI. We used a field map where the x, y and z dimensions of the magnet were covered by intervals of 5 cm. Our code gets the magnetic field value for a given point $\vec{r_0} = (x_0,\ y_0,\ z_0)$ within the magnet by an interpolation in the mentioned map, using the equation 6.1.

$$\begin{aligned} B_i(\vec{r_0}) &= (1-t)(1-u)(1-v)B_i(\vec{r_1}) \\ &+ (1-u)(1-v)B_i(\vec{r_2}) \\ &+ tu(1-v)B_i(\vec{r_3}) \\ &+ tuvB_i(\vec{r_4}) \\ &+ (1-t)u(1-v)B_i(\vec{r_5}) \\ &+ (1-t)uvB_i(\vec{r_6}) \\ &+ (1-t)(1-u)vB_i(\vec{r_7}) \\ &+ t(1-u)vB_i(\vec{r_8}) \quad i = x,\ y\ z \end{aligned} \tag{6.1}$$

where

$$\begin{aligned} t &= \frac{x_0 - x_{lt}}{x_{gt} - x_{lt}} \\ u &= \frac{y_0 - y_{lt}}{y_{gt} - y_{lt}} \\ v &= \frac{z_0 - z_{lt}}{z_{gt} - z_{lt}} \end{aligned} \tag{6.2}$$

and

$$\begin{aligned}
\vec{r_1} &= (x_{lt},\ y_{lt},\ z_{lt}) \\
\vec{r_2} &= (x_{gt},\ y_{lt},\ z_{lt}) \\
\vec{r_3} &= (x_{gt},\ y_{gt},\ z_{lt}) \\
\vec{r_4} &= (x_{gt},\ y_{gt},\ z_{gt}) \\
\vec{r_5} &= (x_{lt},\ y_{gt},\ z_{lt}) \\
\vec{r_6} &= (x_{lt},\ y_{gt},\ z_{gt}) \\
\vec{r_7} &= (x_{lt},\ y_{lt},\ z_{gt}) \\
\vec{r_8} &= (x_{gt},\ y_{lt},\ z_{gt})
\end{aligned}$$

The subscripts gt and lt make reference to the values of x, y and z in the field map which are next to x_0, y_0 and z_0, being $x_{lt} < x_0 < x_{gt}$, $y_{lt} < y_0 < y_{gt}$ and $z_{lt} < z_0 < z_{gt}$.
For ALADIN the most important one is the vertical B_y component of the field, which is constant along the x, y and z directions and responsible of the dipolar behaviour of the magnet. The B_x component of the field is neglegible and B_z is antisymmetric in the y and z coordinates. Taking this into account, the most relevant effect of the magnetic field over the ion trajectories will be a deflection in the x direction, depending on the ion and its energy as it is shown in equation 6.3, where m is the rest mass of the ion, q is its charge and ρ is the radio of curvature in the magnetic field B. We will use this effect to reconstruct the proton momentum.

$$\rho = \frac{\gamma m v}{Bq} \tag{6.3}$$

It is clear that a bigger deflection will result in a better separation of the proton trajectories with different momentum and will improve the resolution in the momentum reconstruction. We have selected for the simulations the maximum intensity of the field that allowed the transmission of the protons, without hitting the magnet side walls. We see in equation 6.3 that the magnitude of the field has to be modified each time we consider a different energy in order to preserve the deflection power.

6.4. Application to the experiment

The starting point of a G4 simulation is the implementation of an event generator that in this case is a file containing energy-momentum values for

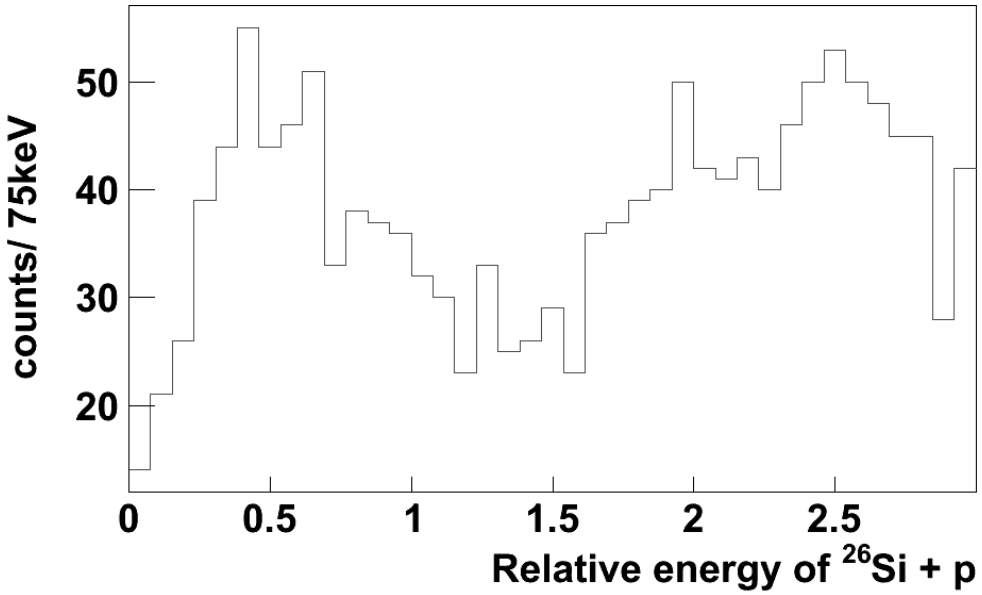

Figure 6.3: Relative energy spectrum of the CD reaction obtained from the theoretical calculation convoluted with the resolution in the simulation.

the fragments produced in the C.D. of ^{27}P following the theoretical estimations by Stefan Typel.
The event generator is based on a data file where the 4-momentum of the proton and of the ^{26}Si are stored for 10^5 CD events for ^{27}P at 500 MeV/nucleon, which can be randomly triggered.
As we try to perform a realistic simulation, the emission point within the target was forced to follow a Gaussian distribution with $FWHM = 1\ cm$ in the x and y coordinates, reproducing the expected beam profile. For the z coordinate, the location straggling was taken into account by means of a step function covering the thickness of the Pb target.
In this case, we have simulated the ^{26}Si and the proton coming out from the ^{27}P CD through the ALADIN setup.

As explained in section 3.3 a theoretical calculation was used to generate a data file containing the information of the quadrimomenta of the outgoing fragments of the CD reaction. The simulation is run using that input and the data are analysed in the same way as the real ones. The relative energy spectrum can be then represented taking into account the experimental resolution. The result is shown in figure 6.3.

Chapter 7

Experimental results

In this chapter the main observables measured in the experiment are calculated, mainly the relative energy of the outgoing fragments, which gives information of the resonant states of the ^{27}P and the cross section of the reaction. In order to obtain them, momenta of the different species involved and their relative angles are mesured and can be compared to theoretical expectations.

7.1. Relative energy spectrum

The relative energy spectrum is a very convenient observable which helps to study the resonant states of the incoming nucleus and the different electromagnetic decay modes. This spectrum is constructed from the measured momenta and energy as explained in section 2.3.

Figure shows the histogram obtained for our measured data after the selection of the reaction channel. The data amount 1888 events collected after 9 days of beam time, as the reaction is a very exotic process with low cross section as we will calculate later on this chapter.
A first view of the spectrum clearly shows the evidence of the existence of resonant states that are actually predicted by the theoretical model of S. Typel [Typ07] and measured in a previous Coulomb Dissociation experiment in RIKEN at much lower energy (57 AMeV) [Tog08], the previous results from RIKEN are shown in figure 7.2.

In our spectrum we fit the first resonant state in order to estimate the resolution of that resonance. For the higher peaks we estimate the resolution as a function of the square root of the energy scaling from the first resonance. Figure 7.3 shows this behaviour of the widths (σ of the Gaussians) with re-

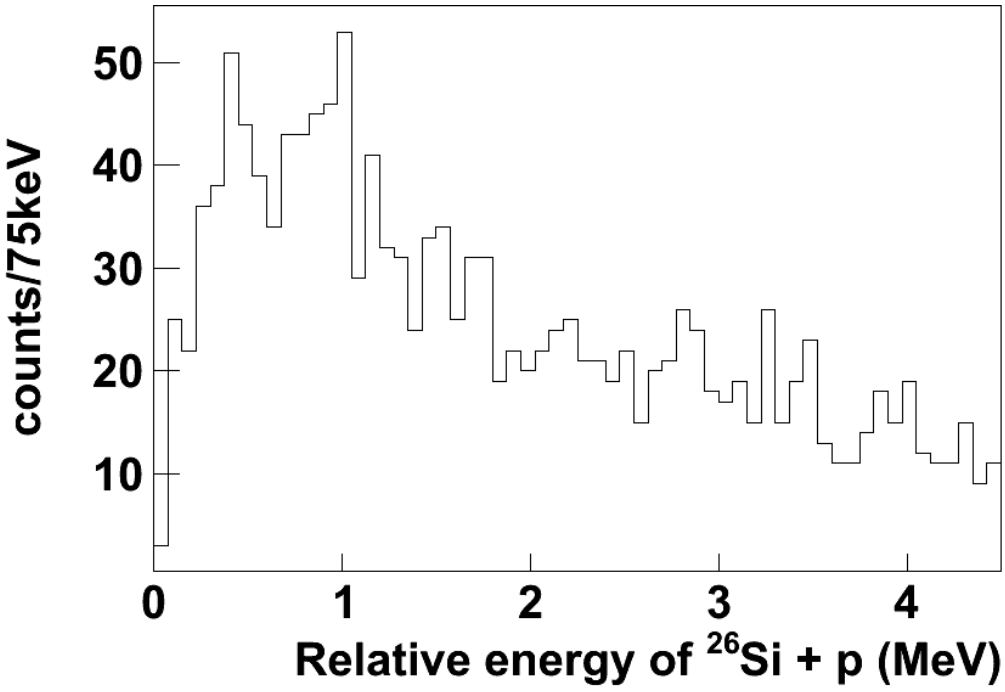

Figure 7.1: Relative energy spectra for the outgoing fragments of the C.D of ^{27}P

spect to the relative energy. The parametrization is: $= 0.2125 \pm 0.0007\sqrt{(E_{rel}}$
In principle, each resonance should behave as a Breit Wigner, but a simple inspection shows that the resolution of the experiment is much broader than the nominal radiative widths (see section 3.2), and thus, the spectrum is dominated by the experimental Gaussian resolution. In figure 7.1 Gaussian functions are used to fit the different peaks. The width is fixed to the calculated value, and only the mean value and maximum of the peak are used as free parameters.
The theoretical calculation [Typ07] estimates a large direct capture component which hides the resonances higher than the second one, however in the experiment we do not see a clear signal of the direct capture component; indeed, with the obtained spectrum it is not possible to estimate the shape or the magnitude of the contribution of this direct component to the total cross section. In all the calculations we will neglect the contribution, knowing that the partial cross section contributions will then be overestimated.
The last peak is not a clear resonance, even though there is a bump which could be interpreted as one. The bad resolution at that energy regime makes it hard to fit the peak and claim that there is a resonance. Anyhow, we fit the peak because it affects the fit of the previous resonance and the dif-

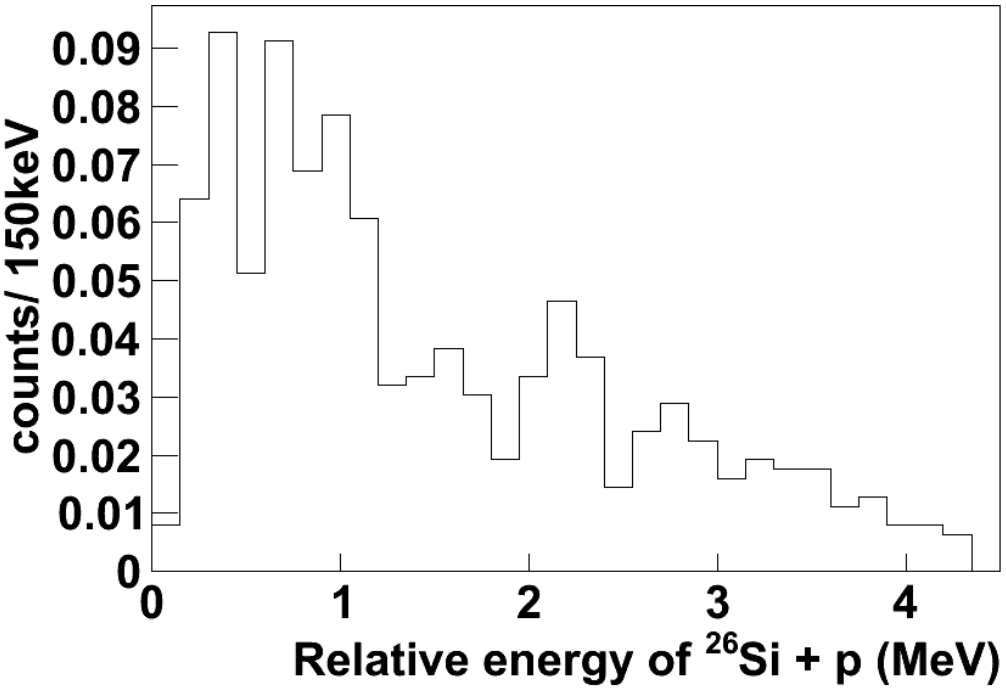

Figure 7.2: Relative energy spectrum of the outgoing system ^{26}Si+p for the RIKEN measurement[Tog08] at 57 A MeV (bottom)

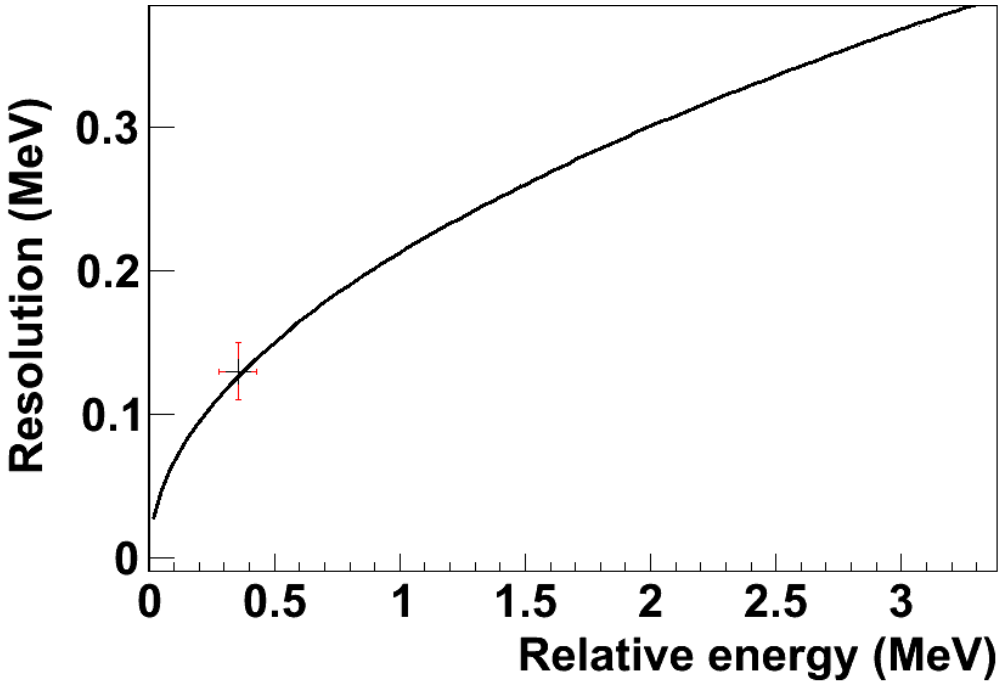

Figure 7.3: Behaviour of the resolution for the resonant states with respect to the relative energy. The cross shows the measured value for the first state; the following states are extrapolated.

ference is crucial for the study of the partial cross section for the different contributions.

The measured relative energies for the resonant states are:

- 0.36 ± 0.07 MeV
- 0.88 ± 0.09 MeV
- 1.5 ± 0.2 MeV
- 2.1 ± 0.3 MeV
- 3.1 ± 0.4 MeV

With the measured values of the relative energy the excitation energy of the incoming ^{27}P can be easily calculated as it is just $E_{exc} = E_{rel} + Q$.

A scheme of the measured excited states in this experiment is represented in figure 7.4 in comparison with the previous measurements of RIKEN [Tog08], Caggiano et al [Cag01] and also to theoretical USDB expectations and the comparison to the mirror nucleus states (^{27}Mg). Our measurements show good agreement within the resolution. In this experiment we had the opportunity to measure the gammas emited in the reaction as well thank to the crystal ball. Thus, we can check if the ^{26}Si of the final state of the C.D. reaction is in the ground state or in the first excited state. It is known that the first excited state of ^{26}Si is at 1.795 MeV, meaning that in order to populate this state we would need a virtual photon of around 2.7 MeV. Those photons would involve a direct capture component which would most likely decay to the ground state. To prove that actually the contribution to the first excited state of the ^{26}Si is negligible, we have measured the gammas in the crystal ball. The obtained spectrum needs to be Doppler corrected. We check the spectra of the crystal ball in coincidence with our reaction after addback and Doppler correction, and what we see is the spectrum in figure 7.5 which actually shows a peak at 1.80±0.05 MeV which can be claimed to be the nominal 1.795 MeV coming from the decay of the first excited state of the ^{26}Si.

The nominal efficiency of crystal ball is 96% for a 1.3 MeV gamma and 0.9 for 3 MeV, we can then estimate that only some 2% of the cases populate the first excited state, being this component negligible.

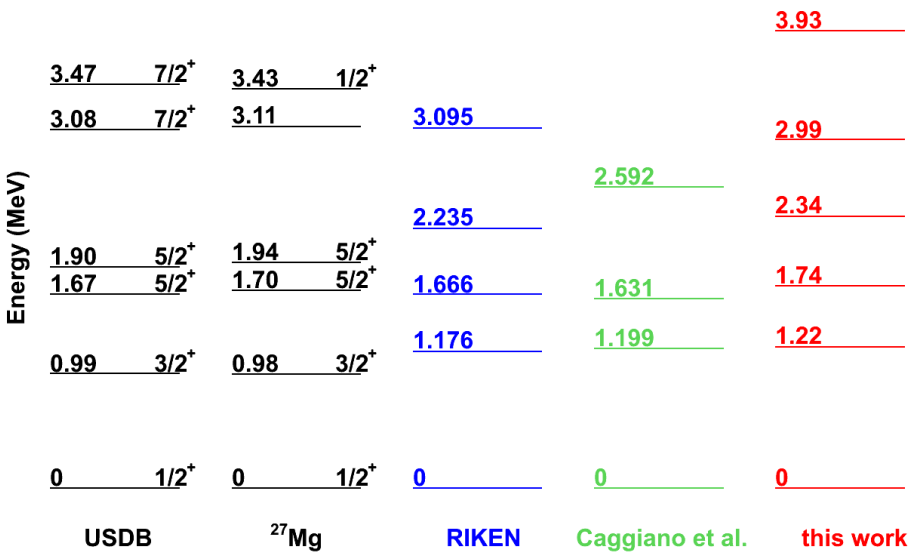

Figure 7.4: Level scheme for the ^{27} excited states measured in this experiment, compared to the previous measurements in RIKEN, the mirror nucleus ^{27}Mg and USDB calculations

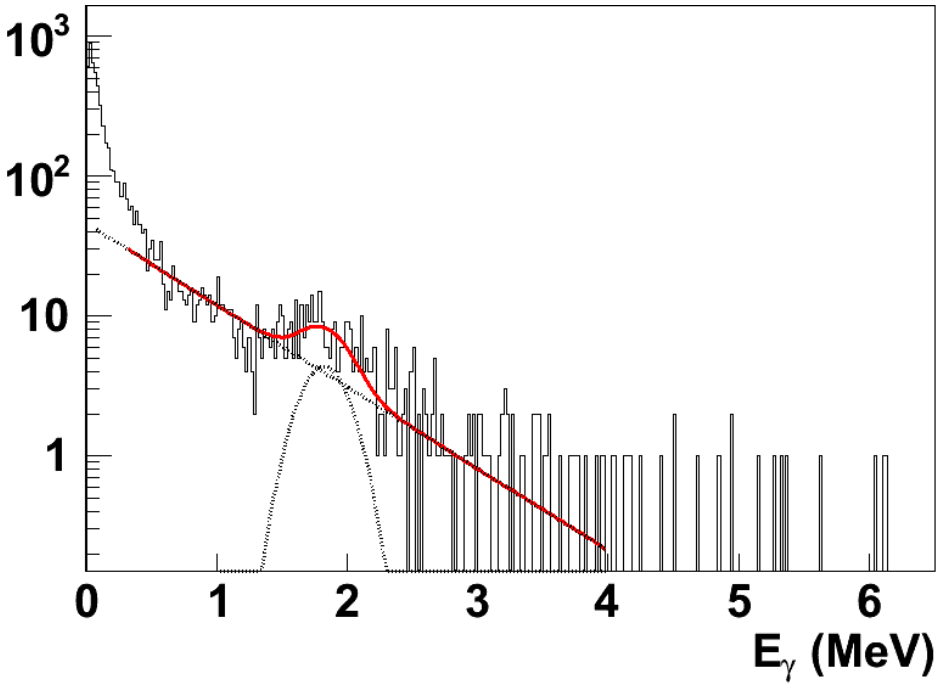

Figure 7.5: Gamma spectrum measured in crystal ball in coincidence with Coulomb Dissociation events. The $^{2}6Si$ first excited state peak (1.795MeV) gamma can be seen.

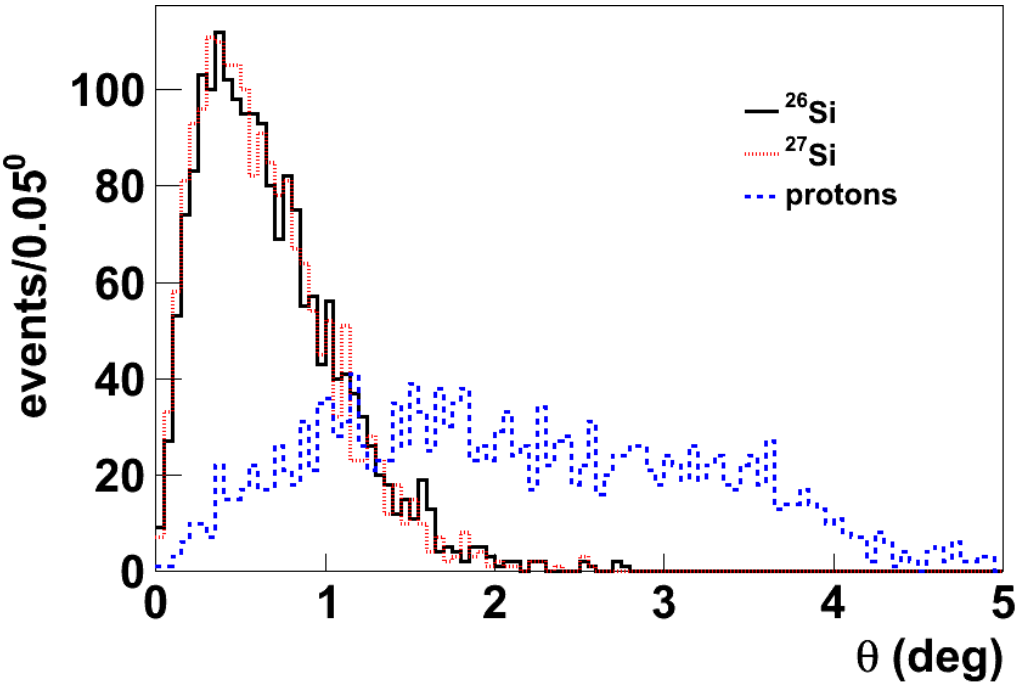

Figure 7.6: Laboratory relative polar angles in the reaction plane of the 3 charged particles of the reaction: ^{27}P, ^{26}Si and protons. The angle of the outgoing fragments (^{26}Si and protons) is derived from the measured momenta. The ^{27}P is derived from the momentum which is reconstructed using the momenta of the outgoing ones taking into account the conservation of the momentum before and after the reaction.

7.2. Angular distributions

After performing the tracking (see section 5.2.7) the momentum vectors for the outgoing particles (protons and ^{26}Si) are reconstructed. With this information one can also reconstruct the angular distribution of these species just after the reaction took place in the target and also the angular distribution of the projectile (^{27}P). In figure 7.6 the measured distribution for the three species are represented. One can clearly see that the two heavy fragments are confined to a small scattering angle range with a maximum around 1.5^0. Protons are distributed over a much larger range with the maximum around 5^0, thus, the main geometrical cut will be due to the proton detection through the DCH and TFW.

This measurement can be compared to theoretical calculations [Typ07]

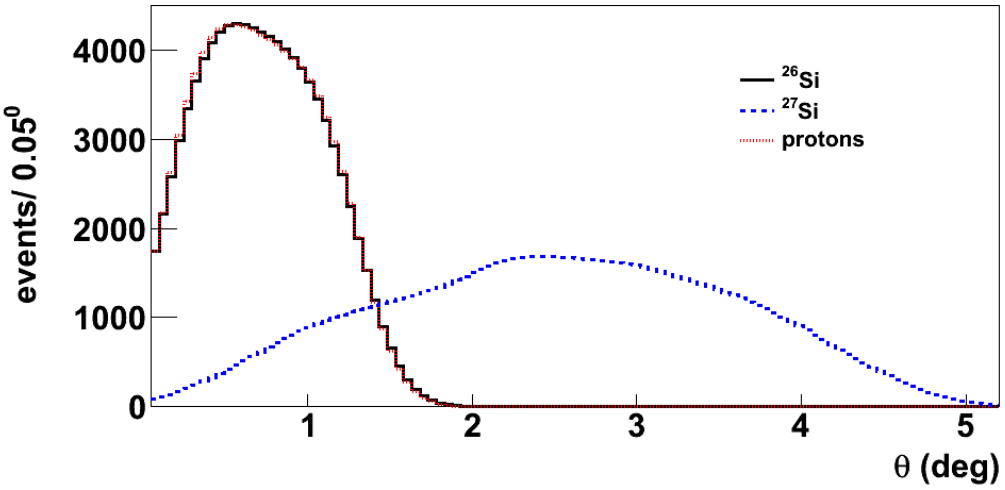

Figure 7.7: Distributions for the laboratory angles of the projectile ^{27}P and the fragments ^{26}Si and protons from the simulation of the breakup reaction $^{208}Pb(^{27}P,^{26})^{208}Pb$ at a projectile energy of 500 MeV per nucleon

and simulations in order to prove that the reaction mechanism is well understood and explained with the models which were used. In figure 7.7 one can see that the prediction of the maximum angles and distribution shapes is in good agreement with the measurements. The experimental angular resolution is spoiled due to the fact that the target interaction point cannot be defined with high precision as it has to be done with the PSP detectors. The SST would provide a better resolution but they did not work properly for the selection of the protons (they cannot be separated from delta electrons). Another interesting observable that we can construct is the relative angle between the outgoing ^{26}Si and proton. As long as we have the momentum vectors measured it is easy to calculate relative angle between the protons and the ^{26}Si. The distribution can be seen in figure 7.8 and shows evidence of the resonant states which we have studied in the relative energy spectrum. This can be used as a crosscheck.
A direct measurement of this observable would be interesting as it would give direct information regarding the resonant states, however, in this experiment we did not have the chance to measure it because the SSD provide a high precision position measurement for the ^{26}Si but not for the position of the protons due to the large number of delta electrons. The fact that only have one silicion strip detector is located after the magnet makes it impossible to distinguish the real proton track. In following experiments a second SSD was set in front of the first one making it possible to measure the polar angle

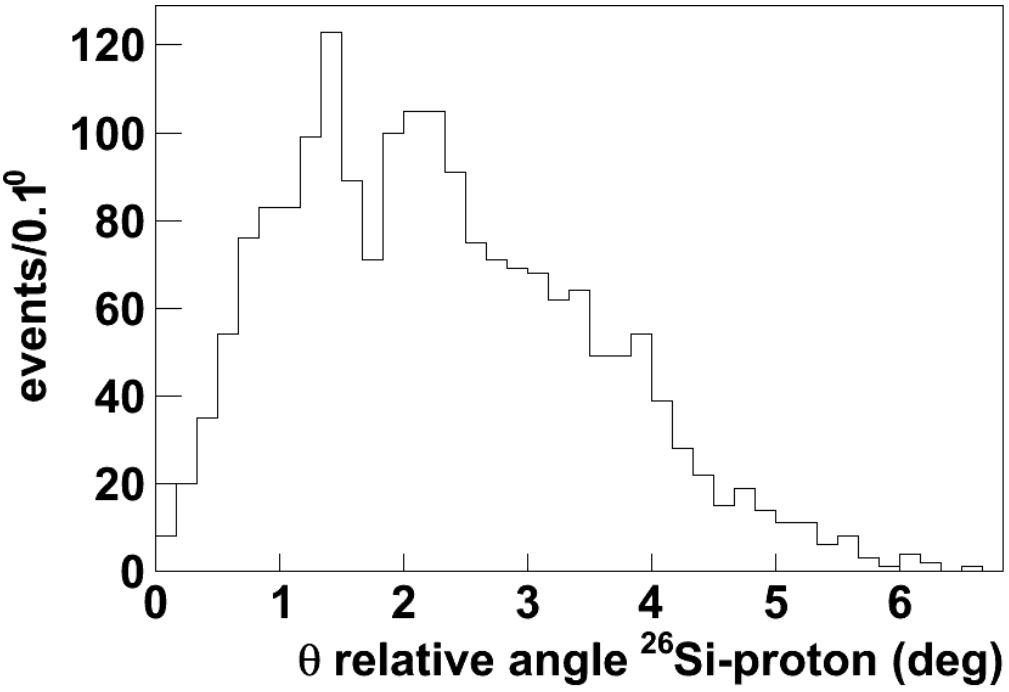

Figure 7.8: Relative polar angle in the laboratory of the outgoing fragments ^{26}Si and proton

directly.

7.3. Cross section

The cross section is an observable of major interest as it helps in understanding the reaction and its implications as explained later in the conclusions chapter. In this case we will provide the calculation of the total cross section for the C.D reaction as well as the partial cross sections for the different resonant states measured.
The reaction channel in which we are interested is the Coulomb Dissociation reaction. For this purpose we need to select those events in which an incoming ^{27}P nucleus is measured before the target and a ^{26}Si in coincidence with a proton after the reaction took place. The ratio between those events and the total ^{27}P coming from the secondary beam and detected before the target, will be used for the calculation of the cross section.
In order to give reasonable numbers a realistic estimation of the total efficiency is extremely important. In the following section we will try to explain

the different contributions that may affect our measurement and the errors involved.

7.3.1. Efficiency

For the estimation of the total efficiency, one needs to evaluate the intrinsic detection efficiency of the different parts of the setup, the efficiency of the different cuts and triggers and also the geometrical efficiency. Let us study the different contribution one by one:

- **^{27}P detection:** The secondary beam selected in the FRS gets to the Pb target. A cut on the ^{27}P using the information coming from the PSP and POS detectors is done. The number of incident ^{27}P is crucial in order to calculate the cross section. To do so, one could count directly the number of nucleus measured by the so-called incoming detectors, but in that case, one would need to carefully estimate the intrinsic efficiency of the GFI detectors and NTF when counting the outgoing ^{26}Si. Alternatively, the counting of ^{27}P can be done in the last detector (i.e. NTF): in this case a selection cut is done in the incoming deterctors, choosing a charge Z=15 and mass over charge A/Z=1.8 and selecting the reaction channel trigger (requests a hit in the NTF) which is downscaled a factor 4. In coincidence with this cut, we count all the events which hit the NTF. Then when calculating a cross section, one evaluates the counting rate of outgoing ions compared to the number of ^{27}P counted from the secondary beam, but, if we do the counting of both incoming and outgoing in the last NTF of the setup, the intrinsic efficiency of the different detectors as well as autoabsorption and transmision effects are neglected. In general we have N_0 as the counting in the incoming region and N_{out} for the reacted beam in the outgoing and the cross section would be

$$\sigma = \frac{N_{out}}{(N_0 \cdot \epsilon_{out})} \tag{7.1}$$

where ϵ_{out} is the efficiency of the heavy ion branch detectors. Doing the counting in the NTF we would have an incoming counting of N_{0ntf} and for the fragments N_{out}; the cross section in this case would be calculated as

$$\sigma = \frac{(N_{out} \cdot \epsilon_{out})}{(N_{0ntf} \cdot \epsilon_{out})} = \frac{N_{out}}{N_{0ntf}} \tag{7.2}$$

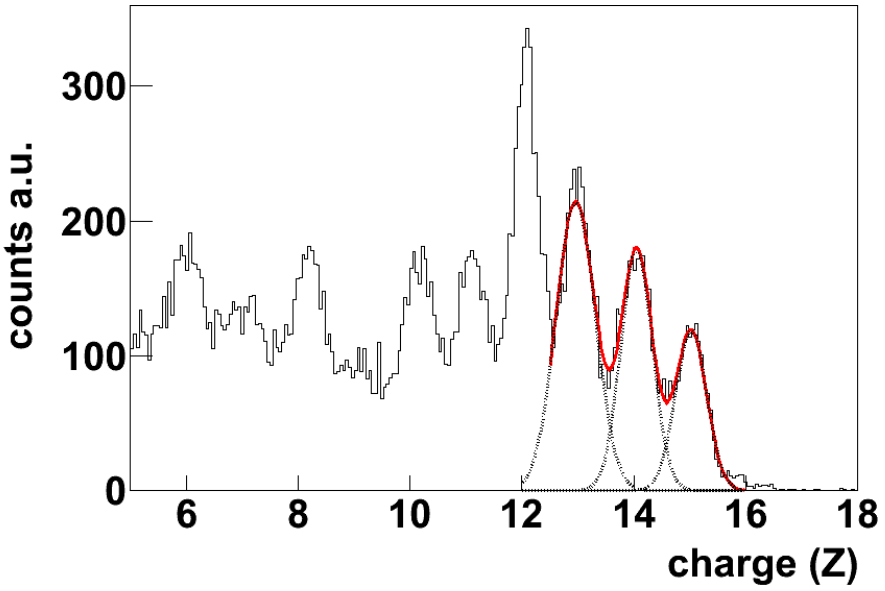

Figure 7.9: Charge (Z) of the outgoing fragments measured in the NTF. The plot shows a fit to the last three charges which is necessary to select the ^{26}Si nucleus of Z=14

and the contribution of the outgoing detectors is neglected.
In this experiment the total number of incoming ^{27}P measured in the NTF is 4440738 with a reaction trigger downscaled a factor 4, and the tracked outgoing ^{26}Si are counted to be 1788 without downscale.

- **^{26}Si detection:** In the NTF the heavy ion charge needs to be selected from all possible candidates. The detector has a good resolution in charge. We choose the cut withing 2σ of the mean value with an associated error of 95.4%. In figure 7.9 the charges measured in NTF are plotted. The separation between contiguous charges is clear. A fit of the three last charges is shown. The mean value for the ^{26}Si is 14.05 and the σ=0.28, so we make a cut in a charge value from 13.44 and 14.56 which comprises 2σ.
  As explained before, the intrinsic efficiency effects are neglected in the cross section calculation as the counting of the incoming ^{27}P is also done in the NTF.

- **Proton detection:** The protons after the reaction have a scattering angle ranging from 0 to 5 degrees. After ALADIN these protons are deflected into the so-called proton branch and need to be detected in

two DCH and the TFW. In order to estimate the detection efficiency we count the protons detected in two of the three detectors in coincidence and we compare with the counting obtained for the third one. With this method it is not neccessary to supposse a 100% efficiency for any of the detectors and compare with it.
The values obtained with this calculation are:

- DCH1 93.6 ± 1.4%
- DCH2 96.5 ± 1.5%
- TFW 84.8 ± 1.1%

and the total efficiency for the entire branch would be 77 ± 2%

- **Geometrical efficiency:** Another important factor to take into account is the geometrical efficiency of the setup. In principle we claim that our setup covers full kinematics but this is never exact, and thus, precise studies are needed.
After the fragments are tracked, one can study the momentum distributions that are expected to be pure Gaussians. Whenever we see the tails of the Gaussian cut, we can say that there is a geometrical constrain in the detector which avoids the full detection. In this experiment the heavy ions dont show any constrain as it was actually expected knowing that the scattering angle is very small (maximum 1.5 degrees) (see fig. 7.6) and the ion distribution after the magnet is very well confined within the area range of the detectors. But this is not the case for the protons; the scattering angle and spread are much larger and several cuts can be seen in the momentum distribution.
In figures 7.10 and 7.11 the momentum distribution in x and y direction at different ranges of relative energy is plotted for the protons. The lack of statistics makes it hard to work with the momentum divided in regions. The binning is chosen accordingly in order to get quasi-Gaussian shapes. The y components are not centered in 0, showing that the detector is not perfectly perpendicular to the beam in that direction.
For every region we calculate the expected Gaussian distribution and estimate the "missing" counts. This is our estimation of the efficiency. One can also see that the momentum distribution gets broader when increasing the energy, indeed we can claim that grows with the square root of the relative energy. The errors are only statistic ones. For every region we estimate the total geometrical efficiency as the product of

the x and y contributions and the statistic error transmited. The total efficiency is then calculated as the average of the six regions weighted with the maximum value given by the Gaussian fit and the error using the statistical error transmision expression with the derivatives. The average calculated value is 75± 14%

Another way of studying the geometrical cuts is by plotting the azimutal angle ϕ of the reconstructed ^{27}P. This angle is reconstructed from the tracking of both outgoing species ^{26}Si and protons, so, any existing cut would appear. The distribution for this angle should be plain and any deviation can be explained with a geometrical cut. In figure 7.12 one can clearly see that the distribution is far from being plain. We estimate the maximum value at $\pm 90^0$ to be the maximum geometrical efficiency, and thus, all other regions should amount the same number of counts. The estimation of the maximum at which the efficiency would be 100% is the bigger error source. We calculate the efficiency first supossing that the maximum is at 60 counts and then at 40 counts and we take the average. The error is the difference between the average and the maximum and minimum selected. A simulated ϕ spectrum is plotted in red over the measured one. The difference between them gives the efficiency. With this study the value obtained is 73 ± 15% in perfect agreement with the value obtained with the momentum distributions.
We can now use both measurements in order to estimate the total geometrical efficiency getting 74 ± 15%.

The total efficiency taking into account all the contributions amounts 57 ± 12%.

With all these we can represent the variation of the efficiency with the relative energy as in figure 7.13. This dependency is then used to calculate the partial cross section of the different resonant contributions.

7.3.2. Total cross section estimation

An electromagnetic excitation (named Coulomb contribution) cannot be exclusively measured, it always comes accompanied by secondary reactions when measured via the virtual photon approach. We have to handle with two different contributions: non-specific reactions taking place outside of the target and reactions at the target due to nuclear interactions (named nuclear

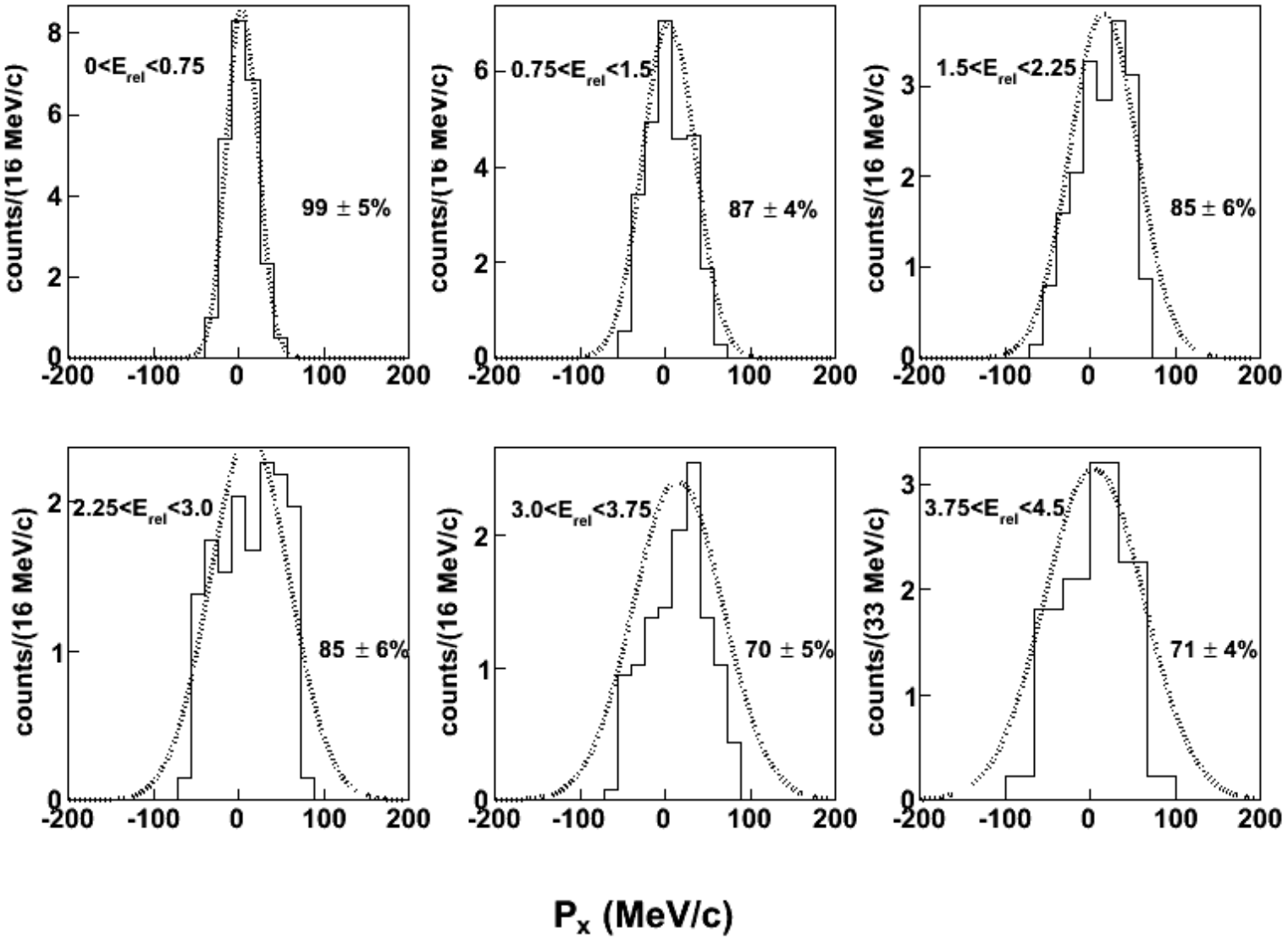

Figure 7.10: Efficiency study of the momentum distribution for the x component for different relative energy regions. Every plot shows the reconstructed momentum for a range of 0.75 MeV in relative energy. The Gaussian fits show the expected momentum distribution. The difference between the measured area and the one calculated with the fit gives the efficiency

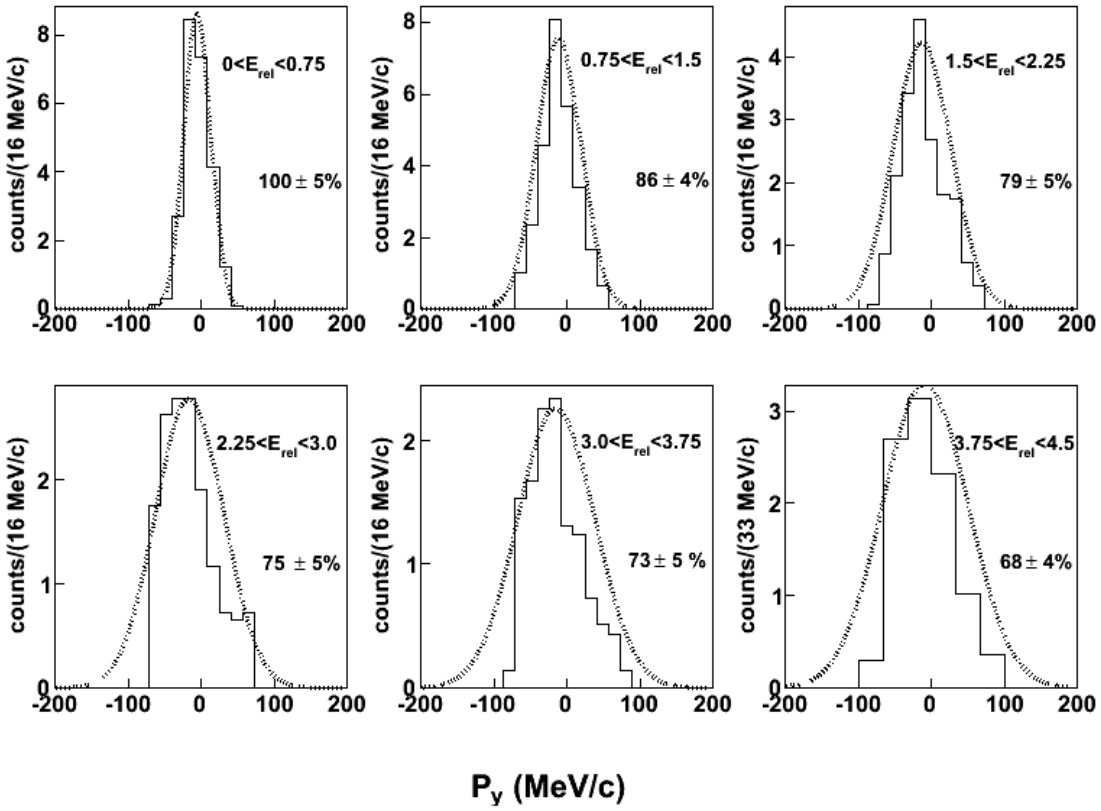

Figure 7.11: Efficiency study of the momentum distribution for the y component for different relative energy regions. Every plot shows the reconstructed momentum for a range of 0.75 MeV in relative energy. The Gaussian fits show the expected momentum distribution. The difference between the measured area and the one calculated with the fit gives the efficiency

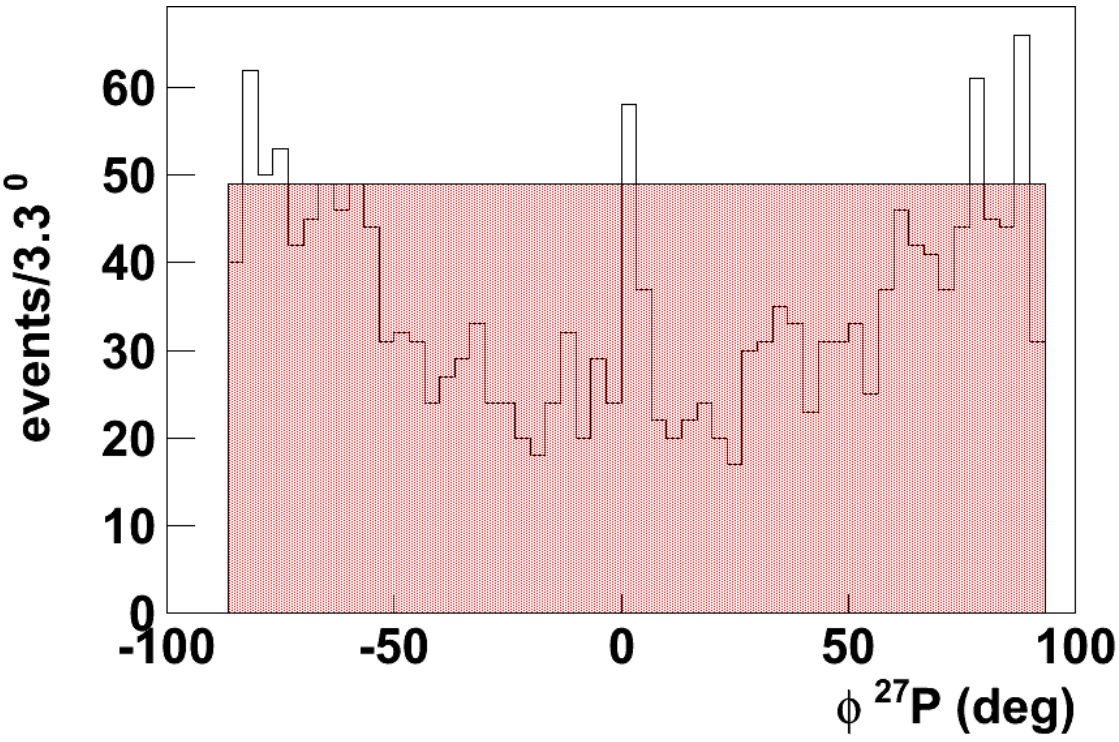

Figure 7.12: Azimutal angle of the ^{27}P nucleus. The asymetry provides information about the geometrical efficiency. The red distribution is a simulated one of the plain angular distribution expected.

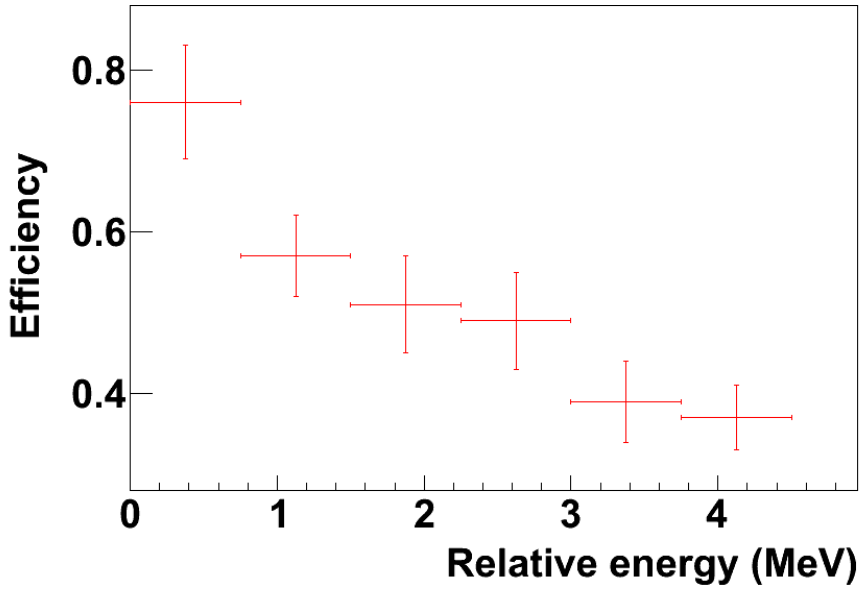

Figure 7.13: The figure shows the efficiency values obtained at different relative energies

contribution). Nuclear and Coulomb contributions cannot be separated because the impact parameter cannot be measured. In addition, the secondary reactions occurring in layers of matter other than the target cannot be sorted out event by event since the single SSD after the target does not allow a precise reconstruction of the reaction vertex. Therefore, two inclusive spectra have to be subtracted from each other: one with a ^{208}Pb target and one without target. The electromagnetic excitation follows approximately a quadratic law with respect to the charge of the target nucleus, thus, a ^{12}C target can be used for the measurement of the nuclear component as it will only provide a minor electromagnetic excitation contribution as compared to the ^{208}Pb target (the CD component is then negligible). This is possible provided the scaling of the nuclear component between ^{12}C and ^{208}Pb is known.
For the scaling a semi-empirical model [Bor95] is used providing the nuclear cross section σ_T^{nucl} for a target T using the measured cross section of a ^{12}C target $sigma_C$:

$$\sigma_T^{nucl} = \frac{1 + a \cdot A_T^{1/3}}{1 + a \cdot A_C^{1/3}} \sigma_C \equiv \alpha_T \sigma_C \tag{7.3}$$

with $a = 0.14$. Considering a ^{nat}Pb target with $A_{Pb} = 207.2$, a scaling factor $\alpha_{Pb} = 1.385$ is obtained. The calculation of the Coulomb excitation cross section relies on the following relationship connecting the cross section σ with

the interaction probability p for a target T:

$$\sigma_T = p_T \cdot \frac{M_m(T)}{d_T \cdot N_{Av}} \tag{7.4}$$

where $M_m(T)$ is the molar mass of the target material [g/mol], d_T is the target thickness [g/cm^2], and N_{Av} is the Avogadro number [mol^{-1}]. Taking into account that the background contribution must be subtracted on the interaction-probability level, the Coulomb excitation interaction probability is given by the following expression:

$$p_{CD} = (p_{Pb} - p_{empty}) - (p_C - p_{empty}) \cdot \left(\alpha_{Pb} \frac{d_{Pb} \cdot N_{Av}}{M_m(Pb)} \cdot \frac{M_m(C)}{d_C \cdot N_{Av}} \right) \tag{7.5}$$

Since both Pb and C target measurements contain background, it must be subtracted from both contributions. However, subtracting the background from both measurements yields a larger statistical error than if only the background difference is subtracted once in the end. This can be shown by rearranging equation (7.5):

$$p_{CD} = p_{Pb} - p_C \left(\alpha_{Pb} \frac{d_{Pb}}{M_m(Pb)} \cdot \frac{M_m(C)}{d_C} \right) - p_{empty} \left(1 - \alpha_{Pb} \frac{d_{Pb}}{M_m(Pb)} \cdot \frac{M_m(C)}{d_C} \right) \tag{7.6}$$

The final Coulomb excitation cross section is given when combining equations (7.6) and (7.4):

$$\sigma_{CD} = p_{Pb} \left(\frac{M_m(Pb)}{d_{Pb} N_{Av}} \right) - p_C \left(\alpha_{Pb} \frac{M_m(C)}{d_C N_{Av}} \right) - p_{empty} \left(\frac{M_m(Pb)}{d_{Pb} N_{Av}} - \alpha_{Pb} \frac{M_m(C)}{d_C N_{Av}} \right) \tag{7.7}$$

This last expression can also be applied bin-wise to any observable distribution.

Figure 7.14 shows the tracked masses of Si for the three targets. For the pure C.D. events one expects to have only ^{26}Si but in the nuclear part one can also see ^{25}Si. If the subtraction is correct, this last peak should dissapear. Figure 7.15 shows the final mass after subtraction. One can clearly see that the ^{25}Si peak dissapears as expected.

The obtained value with this formula needs to be corrected with the estimated average efficiency of $\eta = 57 \pm 12\%$, being the final value of the cross section $\sigma_{CD}^{eff} = \sigma_{CD}/\eta$.
The total number of ^{27}P counts for the Pb target is $N_{Pb}^{total} = 17762952$, for

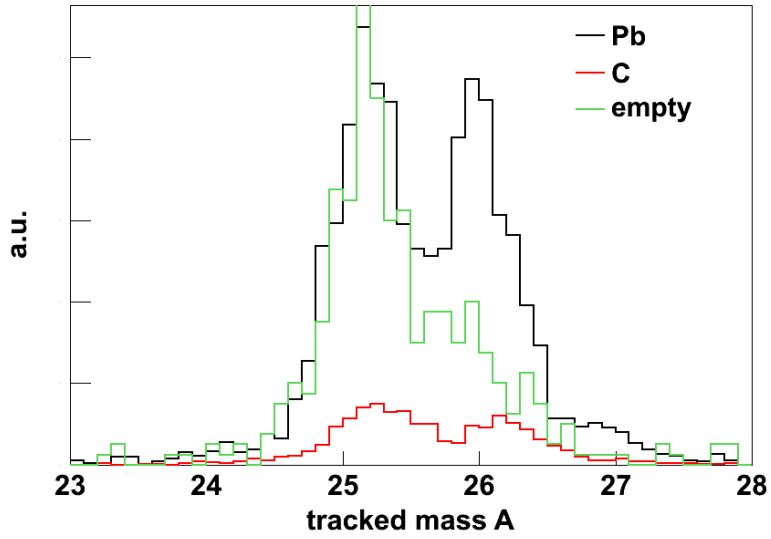

Figure 7.14: Tracked mass of the Si isotopes after the reaction for three targets: lead, carbon and empty.

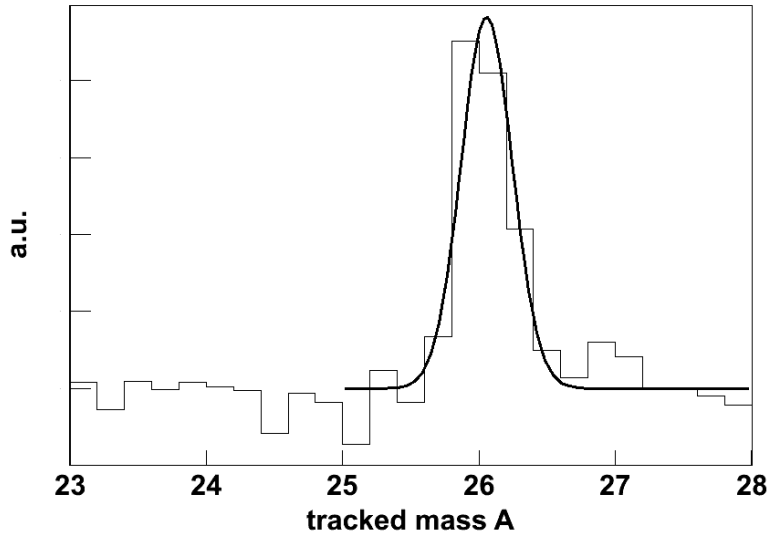

Figure 7.15: Tracked mass of the C.D. after nuclear and background subtraction. Only ^{26}Si is remaining.

the C target $N_C^{total} = 2860684$, and for the empty $N_{empty}^{total} = 2504144$.
From all these statistics the events with a ^{26} and a proton in coincidence in the outgoing amount only $N_{Pb}^{reaction} = 1056$, $N_C^{reaction} = 402$, $N_{empty}^{reaction} = 10$, for the three different targets respectively.
The obtained cross section for the Coulomb dissociation at all relative energies amounts 84± 15 mb, and for energies ranging from 0 to 3 MeV, 55± 7 mb. The considered error sources are the statistical errors and the contribution from the efficiency calculation.
S. Typel's calculation [Typ07] predicted a value of 98 mb for energies up to 3 MeV which does not reproduce the experimental result accurately even though the order of magnitude is correct.

7.3.3. Resonant states cross section estimation

As said before, when inspecting the relative energy spectrum, one can see several peaks corresponding to the excited states of the ^{27}P. In figure 7.13 the dependency of the efficiency with the relative energy is shown. Applying the corresponding values to the relative energy spectrum 7.1 we can reconstruct the spectrum corrected by efficiency. Every calculated factor is applied in an energy range of 0.75 MeV. The resulting spectrum is shown in figure 7.16. The resonant states are again fit to Gaussians.

With the Gaussian fit in the cross section we can now calculate the integral for every peak and convert it to cross section values, having an estimation of the for that particular resonance.
The measured values are:

- 10 ± 3 mb
- 19 ± 4 mb
- 16 ± 3 mb
- 14 ± 3 mb

We do not calculate the cross section for the last state because it would not be reliable as we are not taking into account the higher states that may affect their cross section.

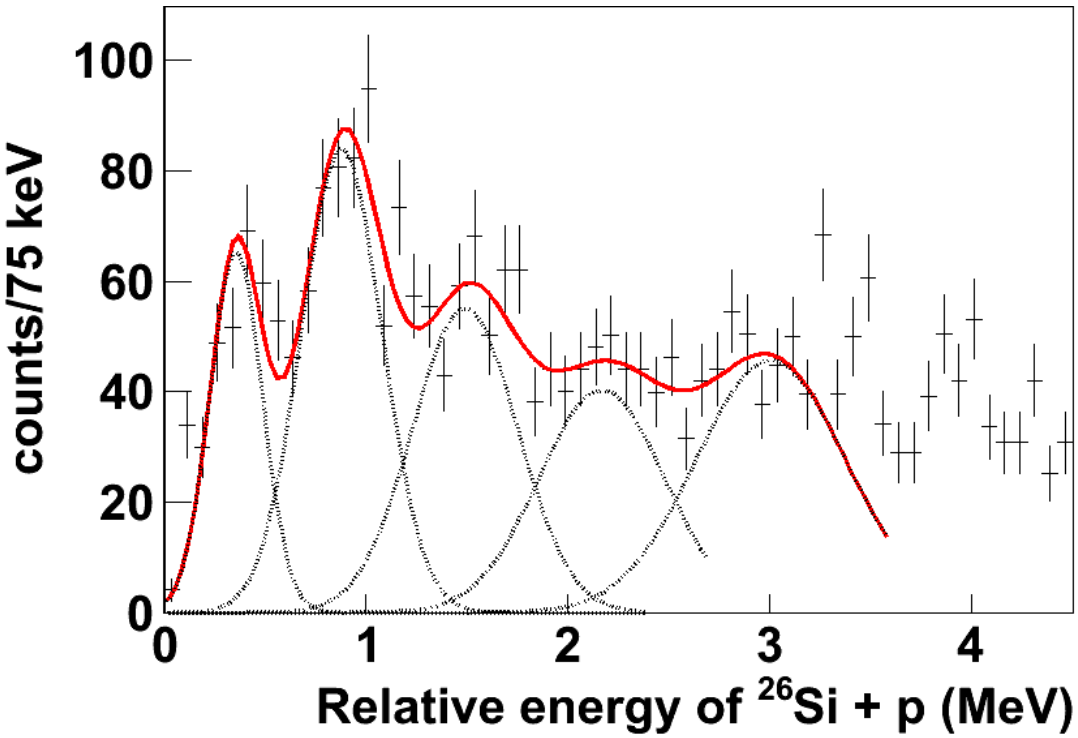

Figure 7.16: Relative energy spectrum corrected by efficiency using the values in figure 7.13. Resonant states are fit to Gaussians.

7.3.4. Cross section of the direct reaction (p,γ), stellar reaction rate and competition between the direct capture and the β decay.

As explained in 2.4, the cross section of the C.D. reaction can be converted into the cross section of the direct capture one.
The first excited state is a mixture of a M1 and E2 components; in order to calculate the direct reaction we need to use the equivalent photon number that depends on the multipolarity. A mixing of 96.4% E2 3.6% M1 was predicted by Stefan Typel for this case, meaning that the measured value for the M1 component is within the error. Using this numbers, the resulting cross sections for the different states are:

- First resonance: $7.8 \pm 1 \times 10^{-8}$ mb
- Second resonance:$2.7 \pm 1 \times 10^{-6}$ mb
- Third resonance:$1.6 \pm 1 \times 10^{-5}$ mb
- Fourth resonance:$1.4 \pm 1 \times 10^{-5}$ mb

In table all the measured quantities are summarised for the different resonant states.

Table 7.1: Experimental parameters of the resonances in ^{27}P. The numbers in brackets indicate the error in the last significative number.

J^π	E^* [MeV]	σ_{CD} [mb]	Γ_γ [eV]	$\omega\gamma$ [eV]	$\sigma_{(p,\gamma)}$ [mb]
$\frac{3}{2}^+$	1.22(7)	10(2)	$4(1)\times 10^{-4}$	$9(3)\times 10^{-4}$	$7.8(1)\times 10^{-8}$
$\frac{5}{2}^+$	1.74(9)	19(4)	$1.3(3)\times 10^{-3}$	$4(1)\times 10^{-3}$	$2.7(1)\times 10^{-6}$
$\frac{5}{2}^+$	2.3(2)	16(3)	$1.9(7)\times 10^{-3}$	$6(2)\times 10^{-3}$	$1.6(1)\times 10^{-5}$
$\frac{7}{2}^+$	2.9(3)	14(3)	$1.7(5)\times 10^{-3}$	$7(2)\times 10^{-3}$	$1.4(1)\times 10^{-5}$

These results can be compared to the theoretical expectations [Typ07] shown in table 3.1. The experimental values for the first two resonant states are larger than the calculation (two times for the first resonance and three times for the second). This could be expected in some sense, as we are not considering the direct capture component at all which in the theoretical model is predicted to amount around 80 mb.

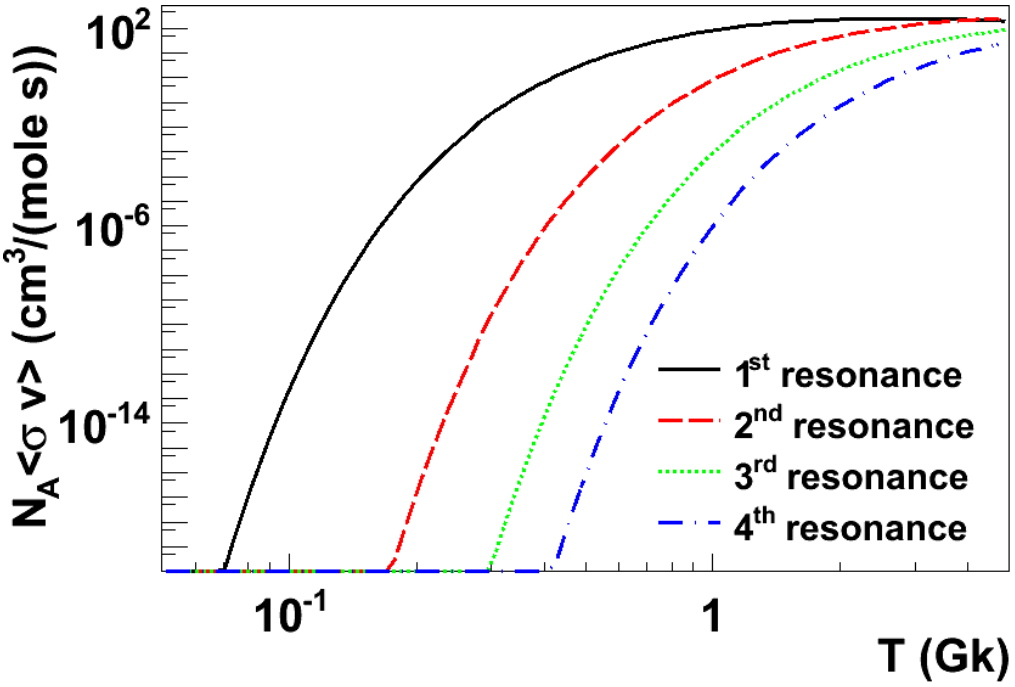

Figure 7.17: Reaction rate for the first three excited states related to the temperature.

With this cross sections calculated one can now estimate the stellar reaction rate for different temperature regimes. By using equation 2.20, the reaction rate for the first excited states with known multipolarities are calculated and plot in figure 7.17 At temperature regimes typical of novae and X-ray burst scenarios (0.08-5 GK) the resonant capture through the first excited state of the ^{27}P dominates being the higher contributions neglegible.

With this reaction rate one can compare the capture reaction with the β decay at different temperature regimes and study how they compete.
The partial lifetime of a given nucleus in a stellar capture reaction X+y→Z+z, can be calculated as:

$$\tau_X = \frac{A_y}{\rho f_y N_A \langle \sigma v \rangle} \tag{7.8}$$

where A_y is the mass number of the projectile, f_y its mass fraction N_A the Avogadro's number and $\langle \sigma v \rangle$ the reaction rate.
In our case A_y=1, f_y=0.5 (based on the fact that most of the fractions measured in novae by spectroscopic means are mostly around that value [Sta98])

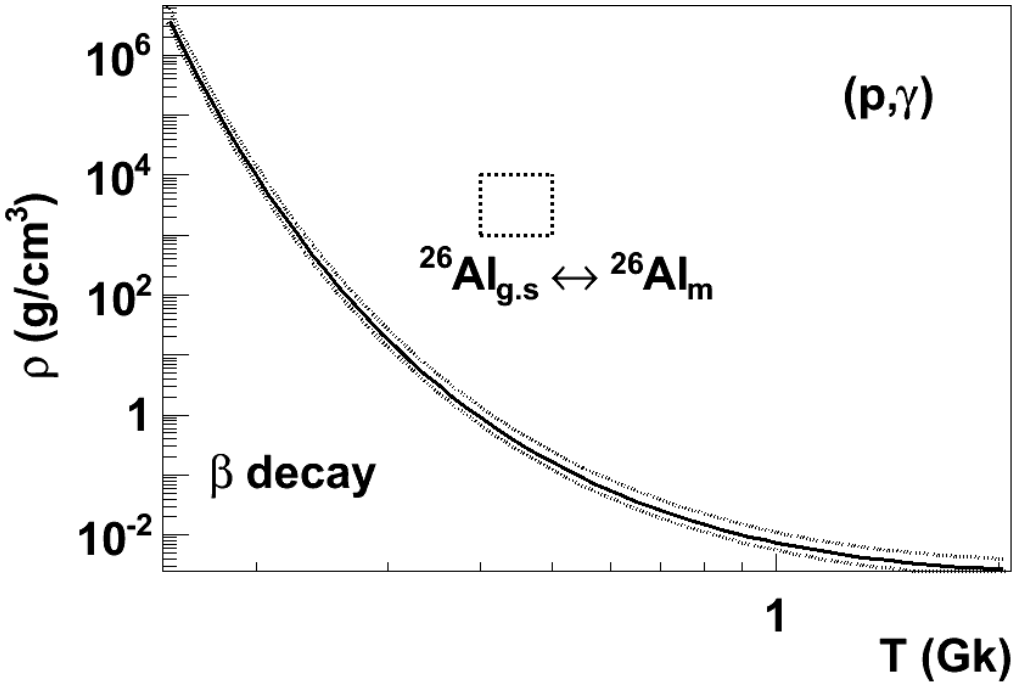

Figure 7.18: Boundary line of density and temperature at which the capture reaction and the β decay have the same strength. The dotted square represents the region in which the ground state of the ^{26}Al and the metastable state are in thermal equilibrum.

and the reaction rate is calculated as in 2.20.

In figure 7.18 the boundary line in which the β decay and the proton capture lifetime are equal. The left region is then dominated by β decay whereas the right one is mainly producing proton capture. At X-ray burst typical conditions (0.3-1.5K and 0.5-2$\times 10^6$ g/cm^3) destructing the ^{26}Si which does not evolve into ^{26}Al. It is also shown the region of density and temperature conditions in which the thermal equilibrum between the ground and metastable state of ^{2}6Al is achieved. In this region one can clearly see that the β decay cannot take place and thus the reaction proceeds mainly via proton capture. This means that the ^{26}Si is not a mayor producer of the $^{26}\mathrm{Al}_m$ which afterwards produce the characteristic 1.809 MeV gamma line of astrophysical interest.

Conclusions

The reaction ^{26}Si(p,γ)^{27}P was studied by using the virtual photon theory in a Coulomb Dissociation experiment in inverse kinematics. The reactions was meant to play a role in the synthesis of the ^{26}Al of astrophysical interest. The main goal of this experiment was to measure the reaction cross section and study the resonant capture properties which may help in clarifying the role of the reaction in the astrophysical scenario.

The experiment was performed at GSI Helmholtzzentrum für Schwerionenforschung in Darmstadt (Germany) using a primary ^{36}Ar beam which provides a secondary 498 MeV per nucleon ^{27}P beam, via fragmentation in a Be target and in-flight selection in a Fragment Separator. The secondary beam impinges a Pb target and the reaction products are studied in full kinematics in the R3B/LAND setup.

With the measurement of the products of the reaction, the relative energy spectrum can be obtained, showing the resonant states of the ^{27}P. Five states are reported at energies 1.22, 1.74, 2.34, 2.99 and 3.93 MeV. All of them are in good agreement with previous measurements in RIKEN. The third state was first evidenced in the RIKEN experiment; with our measurement we can confirm it.
Cross section is calculated for the first states obtaining 9.9, 19.5 and 16.4 mb respectively. The total cross section accounted until 3 MeV of relative energy is 67.3 mb.

Unfortunately with the poor resolution obtained in the experiment, we cannot make a direct measurement of the radiative widths and we cannot extract the S-factor as the direct component is highly suppressed.

The first resonance is an M1/E2 mixture. It was suggested that the measure-

ment of the relative angular distribution could help in having an estimation of the mixing ratio. Our measurement shows that this is not the case, and one should rely in theoretical calculations in order to estimate that ratio, as the M1 component in the Coulomb breakup is highly suppressed.

With this measurements the strength of the resonances is calculated and the stellar reaction rate at temperatures astrophysically typical is also extracted. This shows that the proton capture in which we are interested, proceeds mainly via the first excited state of the ^{27}P at typical astrophysical temperatures (0.1 to 4 Gk).
The obtained reaction rate together with the estimated rate for the proton capture of the ^{25}Mg leads to the conlusion that the ^{26}Si produced in ^{25}Mg(p,γ)^{26}Si proceeds mainly through our studied reaction ^{26}Si(p,γ)^{27}P.
At the same time, we study the competition between the β decay reaction and the proton capture of ^{26}Si. At X-ray burst typical conditions (0.3-1.5K and 0.5-2$\times10^6$ g/cm^3) the capture reaction dominates destructing the ^{26}Si which does not evolve into ^{26}Al. We can also see that density and temperature conditions in which the thermal equilibrum between the ground and metastable state of ^{26}Al is achieved, the β decay cannot take place so the reaction proceeds mainly via proton capture. This means that the ^{26}Si is not a mayor producer of the ^{26}Al$_m$ which afterwards produce the characteristic 1.809 MeV gamma line of astrophysical interest.

Resumen

Esta tesis doctoral se centra en el estudio experimental de la Disociación Coulombiana del ^{27}P a 498 MeV por nucleón en el laboratorio alemán Helmholstz zentrum fur Schwerionenforschung (GSI) con sede en Darmstadt.
La Disociación Coulombiana se usa en este caso para estudiar en cinemática inversa la reacción de captura de protones ^{26}Si(p,γ)^{27}P de alto interés astrofísico.

La Física Nuclear es una disciplina fundamental para construir una imagen coherente de la producción y evolución de los constituyentes primordiales de nuestro Universo, así como de la posterior producción y evolución estelar. En el primer cuarto del siglo XX se desarrollaron un número importante de teorías explicando estos aspectos. En particular, tuvieron gran éxito las teorías de Eddington [Edd20] y Bethe [Bet39] explicando procesos de fusión nuclear que tenían lugar en las estrellas. El éxito de estos trabajos propició el desarrollo de nuevas teorías de nucleosíntesis estelar que se han revelado como una parte clave para profundizar nuestro conocimiento del universo.
En este contexto destaca el famoso artículo de Burbidge, Fowler y Hoyle de 1957 [Bur57] que postula las estrellas como escenarios del origen de los elementos en contraposición a las viejas teorías que asumían que el origen de los nucleidos era una bola de fuego inicial al comienzo del universo que condensaba toda la materia. Estos modelos eran muy atractivos porque permitían explicar gran cantidad de observables, sin embargo, no eran capaces de explicar el hecho observacional de que no todas las estrellas tuviesen la misma composición superficial.

Los principales procesos involucrados en la síntesis estelar son la combustión de Hidrógeno, Helio, Carbono, Neon, Oxígeno y Silicio; captura de neutrones por medio de los procesos s y r (lento y rápido respectivamente), captura de fotones y captura rápida de protones a través del proceso rp.

El proceso rp o captura rápida de protones consiste en la captura consecutiva de protones produciendo así núcleos más pesados. Este proceso ocurre en la zona rica en protones de la carta de núcleos. Este proceso compite con la desintegración α.
Para que la captura de protones sea posible, el medio tiene que encontrarse a muy alta temperatura (mayor de 0.3 GK) para que los protones puedan sobrepasar la barrera Coulombiana presente en todas las reacciones con partículas cargadas. Se necesita también un gran flujo de protones, por ello, se requieren ambientes muy ricos en hidrógeno. La escala temporal del proceso viene fijada por las desintegraciones β^+ en o cerca de la "dripline" de protones, porque la interacción débil es más lenta que la fuerte y la electromagnética a este régime de temperaturas (típicamente del orden de 100s).

La primera evidencia de que la nucleosíntesis es un proceso que todavía está teniendo lugar en las estrellas fue el descubrimiento de trazas con una elevada proporción de ^{26}Mg/^{24}Mg en el meteorito de Allende (grano presolar meteorítico). El estudio de este tipo de granos y los cocientes isotópicos que en ellos se dan (entre ellos ^{27}Al/^{26}Al) , ayuda a clarificar el escenario astrofísico en que se produjeron y también a entender los procesos de nucleosíntesis en estos escenarios. Posteriormente la detección de poblaciones de^{26}Al en escenarios estelares sirvió para confirmar esta hipótesis. Ese isótopo tiene una vida media de medida de 1.05×10^6 años, mucho más corta que la edad del universo, por lo tanto, la detección de este núcleo es una evidencia directa de que la nucleosíntesis es un proceso que todavía está teniendo lugar en las estrellas. La técnica experimental utilizada para ello consistió en medida de los rayos γ procedentes de la desexcitación del ^{26}Mg producido por la desintegración beta del ^{26}Al. La primera medida directa de este rayo γ se desarrolló en el High Energy Astrophysics Observatory [Mah82; Mah84] confirmando así la hipótesis de que las estrellas son importantes agentes de la nucleosíntesis.

La nucleosíntesis del ^{26}Al se ve complicada por la presencia un estado isomérico ^{26}Al$_m$ de corta vida media (τ 9.15 s). La única manera de sintetizar el estado fundamental (de vida media larga) ^{26}Al$_g$ es en escenarios explosivos tipo Nova a través de reacciones de captura de protones por parte del ^{25}Mg; dicha captura puede producir tanto el estado fundamental como el isomérico [Jos99].
El isómero se desintegra fundamentalmente al estado fundamental de ^{26}Mg,

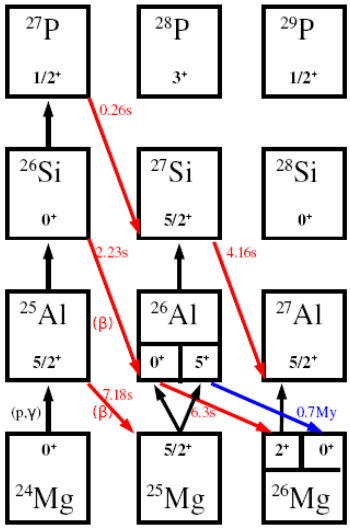

Figure 7.19: Subset of the nuclide chart showing the ions involved in the production of ^{26}Al, including the reaction of interest $^{26}Si(p,\gamma)^{27}P$

mientras que el estado fundamental se desintegra al primer excitado de este produciendo un rayo γ de 1.809 MeV, que puede ser detectado. La principal via de producción del ^{26}Al es ^{24}Mg(p,γ)^{25}Al(β^+,ν)^{25}Mg(p,γ)^{26}Al. Una via alternativa es la cadena ^{24}Mg(p,γ)^{25}Al(p,γ)^{26}Si(β^+,ν)^{26}Al. La destrucción β del ^{26}Si a ^{25}Al compite con la reacción de captura de protones ^{26}Si(p,γ)^{27}P haciendo así un bypass a la producción de ^{26}Al. En la figura 7.19 puede verse un corte de la tabla de núcleos en esta región con las principales reacciones involucradas.
Conviene resaltar que la desintegración β del ^{26}Si produce solamente el isómero ^{26}Al$_m$ y no el estado fundamental.

En este escenario, la reacción ^{26}Si(p,γ)^{27}P es de suma importancia por estar en el camino de producción del proceso rp y por sus implicaciones en la producción de isótopos de alto interés astrofísico como el ^{26}Al y el ^{27}Al.

Disociación Coulombiana del ^{27}P

La medida directa de la reacción estelar de captura de protones (p,γ) es extremadamente complejo [Bem05]; en condiciones típicas de una Nova por

ejemplo, la ventana de Gamow para la reacción^{26}Si(p,γ)^{27}P está alrededor de 300 keV. Por ello, una medida directa requeriría un haz de ,uy baja energía. La sección eficaz en ese régime energético para la reacción de captura sería muy pequeña (del orden de nb) puesto que la energía de los núcleos en interacción está muy lejos de la barrera Coulombiana ($\approx$ 3.5 MeV). Una medida directa requeriría por lo tanto un haz de ^{26}Si muy intenso o que la toma de datos se prolongase mucho en el tiempo para poder acumular suficiente estadística.
Para solucionar este inconveniente, proponemos un método indirecto para extraer la sección eficaz de la reacción (p,γ) a partir de la reacción inversa que puede medirse con mucha más eficiencia.

La Disociación Coulombiana [Bau86] [Win79] se propone como un método muy adecuado para el estudio de transiciones electromagnéticas entre estados ligados de dos partículas y estados resonantes a baja energía relativa entre las partículas resonantes. En este método, el campo nuclear Coulombiano se usa como fuente para el proceso de fotodesintegración, por lo que en lugar de la reacción directa (p,γ), se mide la reacción inversa (γ,p).
La interacción entre dos núcleos puede tener origen nuclear o electromagnético, el electromagnético domina para valores altos de parámetro de impacto. C.F. Weizsäcker [Wei34] y E.J. Williams [Wil34] demostraron de manera independiente en 1934 que, bajo ciertas condiciones, la interacción puede compararse con la interacción de un cuanto o fotón virtual, asumiendo que los efectos de las diferentes componentes de radiación se suman de manera incoherente.

En el experimento que nos ocupa, el proyectil es un haz de ^{27}P que se excita mediante el campo producido por un blanco de Pb.

La destrucción del ^{26}Si mediante captura de protones en condiciones de Nova se produce mediante captura resonante del primer extado excitado del ^{27}P en el continuo ($\frac{3}{2}^{+}$) a su estado fundamental. La transición electromagnética compite entre multipolaridades M1 y E2.

El principal propósito del experimento de Disociación Coulombiana es determinar los estados resonantes resultantes y estudiar las diferentes contribuciones electromagnéticas.

A partir de la medida de la sección eficaz de la Disociación Coulombiana puede extraerse el valor correspondiente a la reacción de captura di-

recta (p,γ). Para ello se utiliza la teoría de fotones virtuales de Williams y Weizsäcker.
Para una resonancia dada puede calcularse como sigue:

$$\sigma_{(\gamma,p)} = \frac{\sigma_{CD} E_{ex}}{N_{vp}}$$

siendo E_{ex} la energía de excitación y N_{vp} el número de fotones virtuales equivalentes.
Aplicando ahora el teorema de balance detallado, puede calcularse la sección eficaz directa:

$$\sigma_{(p,\gamma)} = \frac{2J_{res}+1}{(2J_P+1)(2J_{Si}+1)} \frac{k_\gamma^2}{k^2} \sigma(\gamma, p)$$

siendo J_P y J_{Si} los espines the los núcleos incidentes (fósforo y silicio) y J_{res} el espín del núcleo compuesto en el estado resonante. k y k_γ son el número de onda del canal de salida (^{26}Si+p) y el del fotón respectivamente. Pueden calcularse como sigue:

$$k^2 = \frac{2\mu E_{rel}}{\hbar^2}$$

$$k_\gamma = \frac{E_{exc}}{\hbar c}$$

Experimento S223 en GSI (Darmstadt)

El experimento se realizó utilizando el dispositivo experimental de ALADIN-LAND en GSI con un haz de ^{27}P a 500 AMeV producido por la fragmentación en vuelo a partir de un haz primario de ^{36}Ar seleccionado con el espectrómetro FRS.

GSI es una instalación singular que permiten la producción y aceleración hasta energías relativistas de haces de iones pesados exóticos. Las fuentes de iones disponibles permiten la producción de iones que van desde protones hasta uranio. Una vez producidos, se inyectan en un acelerador lineal UNIversal Linear ACcelerator (UNILAC), que acelera los iones hasta energías del orden de 11.4 AMeV [UNI]. A continuación el haz se inyecta en un sincrotrón, el SchwerIonenSynchrotron (SIS 18), que acelera los iones hasta energías de 1 AGeV para el caso del uranio y 4.5 AGeV para protones. La versatilidad de UNILAC y SIS permite el acceso a haces de iones producidos a partir de cualquier haz primario estable o de larga vida media [Gei92].

Tras la fase de aceleración del haz primario en el sincrotrón SIS18, este se transmite hasta un separador de fragmentos (FRS) [Gei92] [Gei95] [Mue92] donde se produce y selecciona el haz secundario. Para la producción del haz radiactivo, se hace incidir el haz primario de alta energía sobre un blanco de producción de Be de 4.19 g/cm^2. Se produce entonces un gran número de especies nucleares por fragmentación nuclear. Los productos de la reacción entran en la primera mitad del FRS, que filtra todas las especies nucleares excepto aquellas con un valor específico del cociente A/Z, que se selecciona mediante el uso de un campo magnético. Cuando una partícula cargada atraviesa un campo magnético, su trayectoria se curva según la expresión

$$B\rho = \frac{p}{Q} \propto \frac{A}{Z}\beta\gamma$$

donde B es la intensidad de campo magnético, ρ el radio de curvatura de la trayectoria, p el momento de la partícula, Q su carga, A y Z los números másico y atómico respectivamente, β la velocidad y γ el factor de Lorentz asociado. La exresión anterior no tiene en cuenta el defecto de masa. La selección de un determinado ion con A y Z conocidos, se realiza a partir de la selección de la intensidad de campo magnético B teniendo en cuenta que el radio ρ viene físicamente fijado por la geometría de los imanes del FRS. A energías relativistas, los fragmentos producidos por fragmentación presentan una anchura en la distribución de velocidades estrecha lo que evita pérdidas debido a la aceptancia limitada que poseen los imanes.
El FRS está equipado con un conjunto de detectores que permiten identificar y trazar las trayectorias de los iones utilizados. De particular relevancia en este experimento son dos centelleadores situados en sendos planos focales del FRS que realizan medidas de tiempo de vuelo que permiten la determinación de la velocidad y en consecuencia la identificación de los iones.
Tras la selección del haz secundario en el FRS, el haz exótico se transmite a la Cave C donde se encuentra el dispositivo ALADIN-LAND.

El dispositivo experimental ALADIN-LAND puede dividirse en regiones:

1. A la entrada del dispositivo se encuentran detectores para la identificación de las partículas incidentes a partir de la determinación de la trayectoria que siguen y su velocidad. Son básicamente un plástico centelleador leido por cuatro fotomultiplicadores (POS) y dos detectores de silicio (PSP). POS es el "start" para todas las señales de tiempo y junto con los centelleadores del FRS mide la velocidad del haz incidente permitiendo determinar la relación carga-masa (A/Z). Los dos PSP se usan para identificar la carga de los iones (Z) a partir de medidas de

pérdida de energía y también para medir la trayectoria de estos a partir de las posiciones.

2. La región del blanco comprende una cámara de reacción de aluminio en cuyo interior está situada una rueda que permite cambiar de blanco fácilmente durante el experimento. Rodeando al blanco se encuentra un detector de silicio de micropistas que permite medir la posición de los productos de reacción tras el blanco. Rodeando la cámara de reacción se coloca un detector de rayos γ llamado Crystal Ball, que es permite la detección de rayos γ originados durante la reacción mediante 162 cristales de NaI colocados formando una esfera, y cubriendo un ángulo sólido de 4π.

3. Tras Crystal Ball se sitúa un imán de gran aceptancia (ALADIN) que permite separar a los productos de la reacción de acuerdo a su rigidez magnética. En este experimento en particular los fragmentos de interés son protones y ^{26}Si. Ambos presentan una relación carga-masa muy distinta, por lo que la separación entre ellos es muy eficiente.

4. Después de ALADIN los fragmentos de la reacción se separan en dos ramas debido a la diferente deflexión que sufren: los protones se curvarán más (en torno a 31^0) mientras que los iones se curvarán unos 16.7^0. Para la detección de ambas especies, se colocan un grupo de detectores en cada una de esas ramas. Para los protones se utilizan dos cámaras de deriva de hilos (DCH) miden las posiciones (trayectorias) y permiten reconstruir el momento. También se coloca una pared de tiempo de vuelo formada por plásticos centelleadores, que da el "stop". Para los iones se sigue la misma estructura, colocando dos detectores de fibras de centelleo (GFI) para medir las trayectorias y una pared de tiempo de vuelo (NTF) que permite la identificacion de los diferentes fragmentos pesados que se producen en la reacción y selecciona así el canal de salida.

Este dispositivo permite la medida de nuestra reacción de interés en cinemática completa.

La calibración y análisis de los más de 2000 canales electrónicos del experimento permite la determinación de los diferentes observables físicos

Resultados

El espectro de energía relativa es un observable muy conveniente que ayuda al estudio de los estados resonantes del núcleo incidente y de los diferentes modos electromagnéticos de desintegración. Este espectro se construye a partir de los momentos y energías de las partículas puestas en juego en la reacción:

$$E^* = \sqrt{\sum_i m_i^2 + \sum_{i \neq j} \gamma_i \gamma_j m_i m_j \left(1 - \beta_i \beta_j \cos \vartheta_{ij}\right)} + E_\gamma - m_{proj}$$

En la figura 7.20 se muestra un histograma con los datos obtenidos para la energía relativa en este experimento con una estadística acumulada de 1888 buenos eventos.
Pueden observarse los dos primeros estados resonantes con claridad así como otros dos estados superiores. La resolución obtenida en este caso es mucho mayor que la anchura radiativa y aumenta con la raíz cuadrada de la energía relativa, por lo que para los picos de mayor energía la resolución es muy modesta, por lo que, a pesar de que aparecen evidencias de resonancias a mayor energía, estos no son concluyentes.
La energía de las resonancias está en buen acuerdo con los valores predichos por S. Typel [Typ07] a partir de un modelo teórico y con medidas previas hechas en RIKEN a menor energía (57 AMeV) del haz incidente de ^{27}P [Tog08]. .

Para poder estimar valores realistas de la sección eficaz asociada a la reacción de disociación Coulombiana, es fundamental hacer una buena evaluación de la eficiencia. En ese sentido, es necesario computar tanto la eficiencia intrínseca de detección de los distintos detectores, como la eficiencia en el anállisis originada por los cortes en la selección de eventos y la eficiencia geométrica:

- En cuanto a la detección de los iones pesados, necesitamos hacer el contaje del número de iones de ^{26}Si que se producen a partir del ^{27}P incidente en el canal de reacción de Disociación Coulombiana. La sección eficaz se evalúa a partir del cociente entre esas dos cantidades. Haciendo el contaje de ambas en la pared de tiempo de vuelo (TFW) conseguimos que los efectos de eficiencia intrínseca se cancelen. En la práctica lo que se hace es seleccionar el ^{27}P y contar todos los iones que dejan señal en TFW en coincidencia, después se cuenta el número de iones de ^{26}Si en el mismo detector y con eso se cancelan las contribuciones intrínsecas.

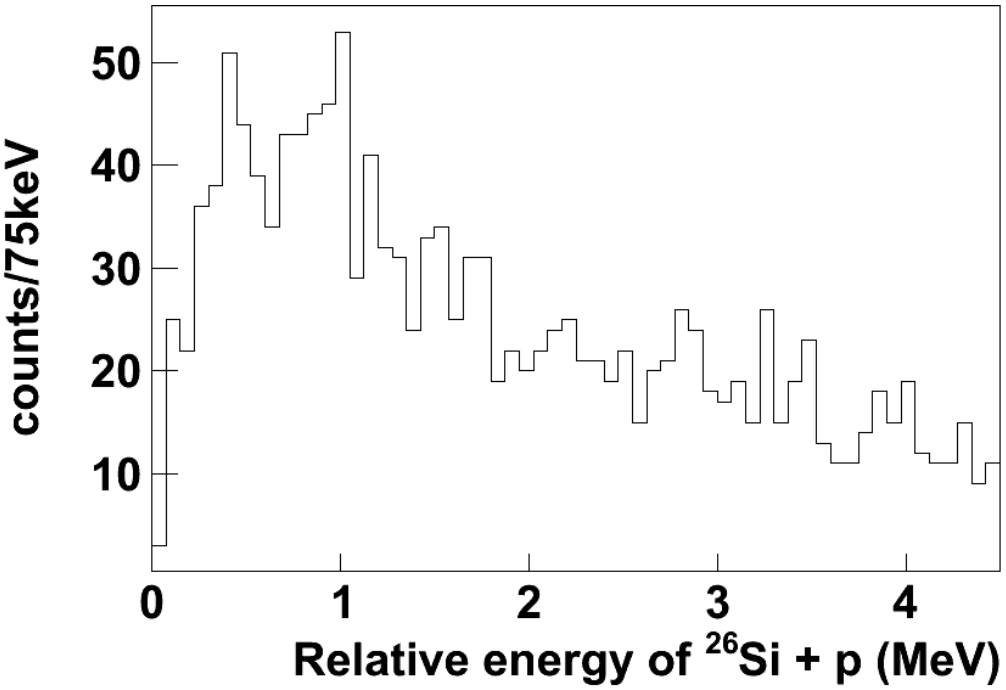

Figure 7.20: Espectro de energía relativa entre los fragmentos producidos en la Disociación Coulombiana del ^{27}P

- La propia selección de las cargas correspondientes al canal de reacción conlleva un error asociado. En este caso podemos aplicar esta selección en nuestros programas de análilsis escogiendo los valores situados a 2σ de la media, por lo tanto el error asociado es de un 95.4%.

- Los protones después de la reacción tienen ángulos comprendidos entre 0 y 5 grados. Después del imán su trayectoria se curva y son medidos por la rama de protones en las cámaras de deriva DCH y muro de tiempo de vuelo TFW. Para estimar la eficiencia intrínseca hacemos el contaje de las partículas detectadas en dos de los detectores a la vez y se cuenta en coincidencia cuántas de estas han dejado señal en el tercero. Los valores obtenidos por este método para la eficiencia de los tres detectores son:

  - DCH1 93.6 $\pm$ 1.4%
  - DCH2 96.52 $\pm$ 1.5%
  - TFW 84.78 $\pm$ 1.1%

  y la eficiencia total de la rama se estima en 76.58 $\pm$ 2.3%

- En cuanto a la eficiencia geométrica hemos hecho el estudio utilizando dos métodos independientes: el primero se basa en estudiar los espectros de momento calculados en diferentes regiones de energía; puede suponerse que cada espectro ha de comportarse de manera Gaussiana; los cortes que aparecen son debidos a la eficiencia geométrica. Se ajusta por tanto el espectro a una Gaussiana sabido el ancho esperado de la distribución y la diferencia con la medida se asigna al corte en eficiencia. El otro método se basa en la distribución angular del ángulo azimutal: esta distribución ha de ser plana. Se estima lo que difiere el espectro de una distribución plana y a partir de aquí se obtiene la eficiencia. El primer método da un valor de eficiencia de 78$\pm$ 5% y el segundo 70$\pm$ 3%, en buen acuerdo entre ellos.

Teniendo en cuenta la eficiencia calculada, podemos representar el espectro de energía relativa y ajustar las diferentes resonancias a Gaussianas (figura 7.21).
La anchura del primer pico es un parámetro libre; las anchuras posteriores se fijan a un valor escalado a partir de la primera con la raíz cuadrada de la energía.
Los valores obtenidos para energía relativa son:

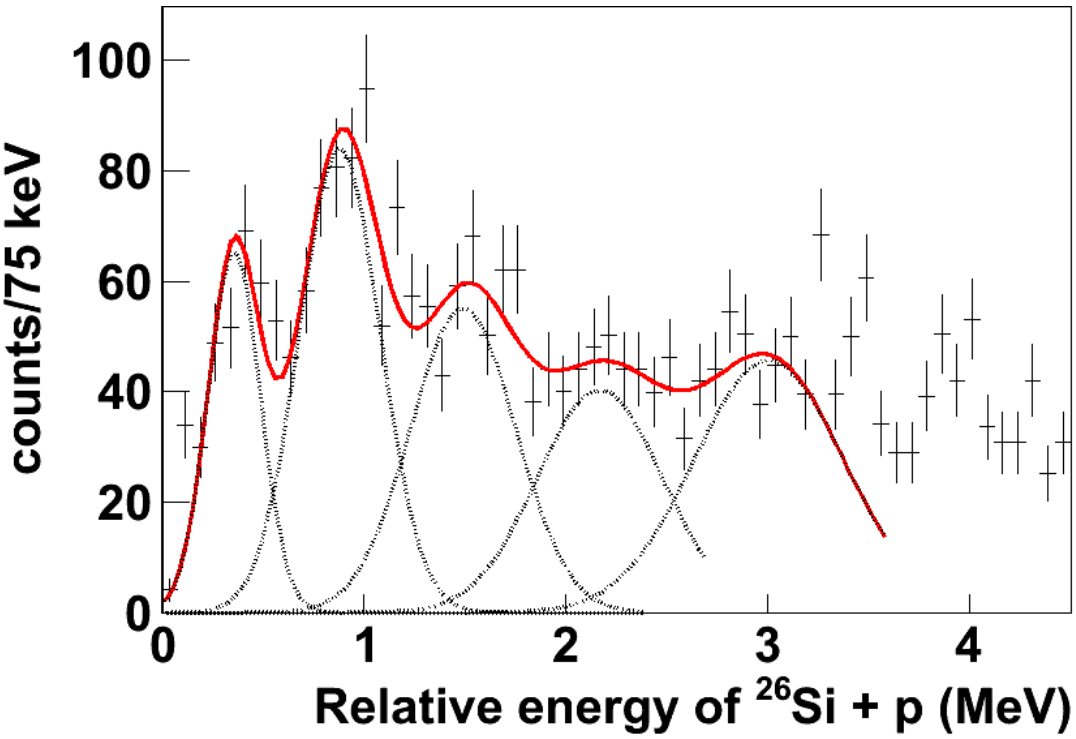

Figure 7.21: Sección eficaz de la Disociación Coulombiana frente a la energía relativa corregida por eficiencia. Los estados resonantes se ajustan a Gaussianas.

- 0.36 ± 0.07 MeV
- 0.88 ± 0.09 MeV
- 1.5 ± 0.2 MeV
- 2.1 ± 0.3 MeV
- 3.1 ± 0.4 MeV

Con esos ajustes podemos calcular la sección eficaz de cada estado obteniéndose los siguientes valores:

- 9.9 ± 3.1 mb
- 19.5 ± 4.4 mb
- 16.4 ± 4.1 mb
- 13.7 ± 3.3 mb
- 16.7 ± 4.1 mb

Un observable de alto interés astrofísico es la velocidad que caracteriza la reacción estelar a una determinada temperatura. [Rol88].
Durante la evolución de una estrella, la temperatura y velocidad de reacción van cambiando; el estudio de estos observables permiten conocer aspectos del proceso evolutivo del astro. En general se define como:

$$\langle \sigma v \rangle = \left(\frac{8}{\pi \mu} \right)^{1/2} \frac{1}{(k_B T)^{3/2}} \int_0^\infty \sigma(E) \exp\left(-\frac{E}{k_B T} \right) dE$$

donde k_B es la constante de Boltzmann, T la temperatura, μ la masa reducida, E la energía y $\sigma(E)$ la sección eficaz. La representación de esta cantidad ayuda a entender el mecanismo de captura a una determinada temperatura, así, puede estudiarse si el proceso resonante es dominante y en qué régimen de temperaturas lo será.

Con nuestros datos podemos representar la velocidad de reacción para los tres primeros estados (fig. 7.22).
A temperaturas típicas de una Nova o de escenarios de estallido de rayos X (0.08-5 GK) la captura resonante a través del primer estado excitado del ^{27}P domina claramente siendo las contribuciones de orden superior despreciables.

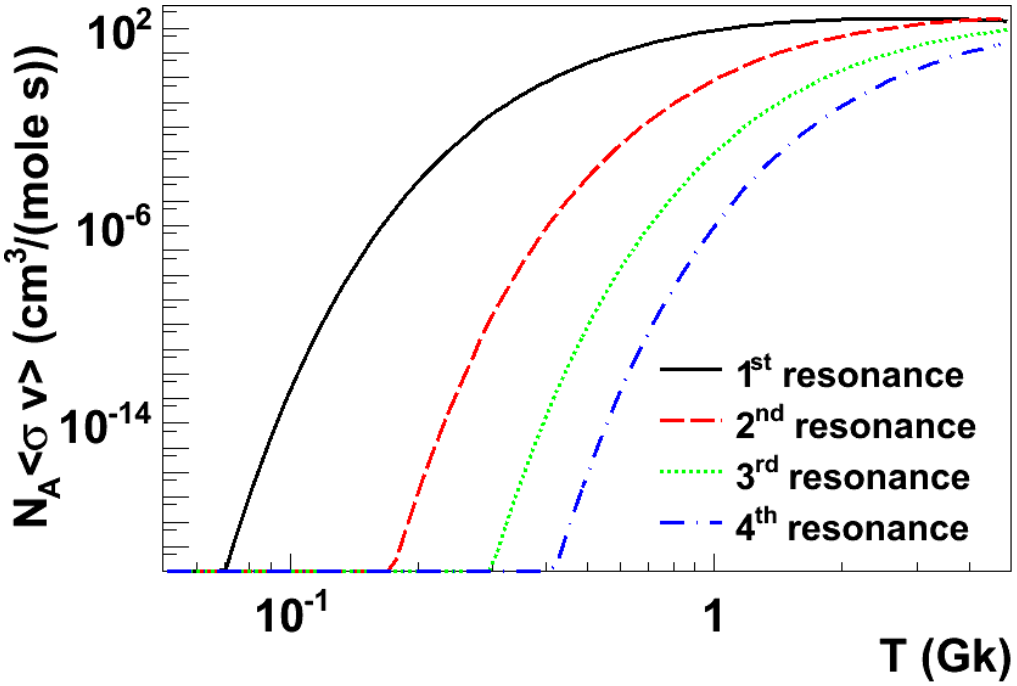

Figure 7.22: Reaction rate for the first three excited states related to the temperature.

A la vista de las medidas podemos concluir que en escenarios típicos de explosiones de rayos X (0.3-1.5K and 0.5-2$\times 10^6$ g/cm^3), la reacción de captura es dominante y por lo tanto el ^{26}Si no es una de las principales fuentes de producción de ^{26}Al

Bibliography

[AB98] B. Alex Brown, *New Skyrme interaction for normal and exotic nuclei*, Phys. Rev. C **58** (1998) 220–231.

[ATI] *ATIMA web page*, `http://www-linux.gsi.de/~weick/atima/`, accesed: 4.01.2011.

[Bau86] G. Baur, C. A. Bertulani and H. Rebel, *Coulomb dissociation as a source of information on radiative capture processes of astrophysical interest*, Nuclear Physics A **458** (1986) 188–204.

[Bem05] D. Bemmerer *et al.*, *Feasibility of low-energy radiative-capture experiments at the LUNA underground accelerator facility*, The European Physical Journal A - Hadrons and Nuclei **24** (2005) 313–319.

[Bet30] H. Bethe *et al.*, *Zur Theorie des Durchgangs schneller Korpuskularstrahlen durch Materie*, Annalen der Physik **397** (1930) 325 – 400.

[Bet39] H. A. Bethe, *Energy Production in Stars*, Phys. Rev. **55** (1939) 103 and 434–456.

[Bor95] K. Boretzky, *Systematische Untersuchungen zur Coulombanregung der Zwei-Phononen-Dipolriesenresonanz in* ^{208}Pb, Ph.D. thesis, Universität Frankfurt am Main, Germany (1995).

[Bur57] E. M. Burbidge *et al.*, *Synthesis of the Elements in Stars*, Rev. Mod. Phys. **29** (1957) 547–650.

[Cag01] J. A. Caggiano *et al.*, *Spectroscopy of Al-23 and P-27 using the (Li-7, He-8) reaction and the implications for Na-22 and Al-26 nucleosynthesis in explosive hydrogen burning*, Phys. Rev. C **64** (2001) 025802.

[Cub98] J. Cub *et al.*, *A large-area scintillating fiber detectors for relativistic heavy ions*, Nuclear Instruments and Methods in Physics Research Section A: Accelerators, Spectrometers, Detectors and Associated Equipment **402** (1998) 67 – 74.

[Die95] R. Diehl *et al.*, *COMPTEL observations of galactic 26 Al emission*, Astronomy and Astrophysics **298** (1995) 445.

[Edd20] A. S. Eddington, *The Internal Constitution of the Stars*, Nature **106** (1920) 14–20.

[Gal78] J. S. Gallagher and S. Starrfield, *Theory and Observations of Classical Novae*, Annual Review of Astronomy and Astrophysics **16** (1978) 171–214.

[Gei92] H. Geissel *et al.*, *The GSI projectile fragment separator (FRS): a versatile magnetic system for relativistic heavy ions*, Nuclear Instruments and Methods in Physics research Section B: Beam Interactions with Materials and Atoms **70** (1992) 286 – 297.

[Gei95] H. Geissel *et al.*, *Secondary Exotic Nuclear Beams*, Annual Review of Nuclear and Particle Science **45** (1995) 163–203.

[Hoy46] F. Hoyle, *The synthesis of the elements from hydrogen*, Mon. Not. Roy. Astron. Soc. **106** (1946) 343.

[Iwa] N. Iwasa *et al.*, *Measurement of the Coulomb Dissociation of* ^{8}B *at 254 MeV /nucleon and the* ^{8}B *Solar Neutrino Flux*, Phys. Rev. Lett. **83**.

[Jos99] J. José *et al.*, *Nuclear Uncertainties in the NeNa-MgAl Cycles and Production of* ^{22}*Na and* ^{26}*Al during Nova Outbursts*, Astrophysical Journal **520** (1999) 347.

[Jos07] J. José and M. Hernanz, *The origin of presolar nova grains*, Meteoritics and Planetary Science **42** (2007) 1135–1143.

[Kie93] J. Kiener *et al.*, *Determination of the 13N(p, γ)14O reaction rate through the Coulomb break-up of a 14O radioactive beam*, Nuclear Physics A **552** (1993) 66 – 81.

[LAN] *land02 webpage*, `http://www-linux.gsi.de/~rplag/land02`.

[Lee77] T. Lee *et al.*, *Aluminum-26 in the early solar system - Fossil or fuel*, Astrophysical Journal Letters **211** (1977) L107.

[Lef95] A. Lefebvre *et al.*, *Astrophysical rate of the 11C+p reaction from the Coulomb break-up of a 12N radioactive beam*, Nuclear Physics A **592** (1995) 69 – 88.

[Mah82] W. A. Mahoney *et al.*, *Diffuse galactic gamma-ray line emission from nucleosynthetic 60Fe, 26Al, and 22Na preliminary limits from HEAO 3*, Astrophysical Journal **262** (1982) 742.

[Mah84] W. A. Mahoney *et al.*, *HEAO 3 discovery of 26Al in the interstellar medium*, Astrophysical Journal **286** (1984) 578.

[Mah09] K. Mahata *et al.*, *Position reconstruction in large-area scintillating fiber detectors*, Nuclear Instruments and Methods in Physics Research Section A: Accelerators, Spectrometers, Detectors and Associated Equipment **608** (2009) 331 – 335.

[Met82] V. Metag *et al.*, *The Darmstadt-Heidelberg-Crystal-Ball*, Technical report, Proc. Geiger Memorial Meeting (1982).

[Mot91] T. Motobayashi *et al.*, *Determination of the astrophysical 13N (p, γ) 14O cross section through the Coulomb dissociation method*, Physics Letters B **264** (1991) 259 – 263.

[Mot94] T. Motobayashi *et al.*, *Coulomb Dissociation of* ^{8}B *and the* ^{7}Be$(p,\gamma)^{8}$B *Reaction at Low Energies*, Phys. Rev. Lett. **73** (1994) 2680–2683.

[Mue92] G. Muenzenberg, *The GSI projectile fragment separator (FRS): a versatile magnetic system for relativistic heavy ions*, Nuclear Instruments and Methods in Physics research Section B: Beam Interactions with Materials and Atoms **70** (1992) 265 – 275.

[Pac84] B. Paczynski, *Binary Stars* **225** (1984) 275–280.

[Pal05] A. Palacios *et al.*, *New estimates of the contribution of Wolf Rayet stellar winds to the galactic 26Al*, Astronomy and Astrophysics **429** (2005) 613.

[Pas08] S. Paschalis, *Relativistic One-Nucleon Removal Reactions*, Ph.D. thesis, University of Liverpool (2008).

[Pra96] N. Prantzos and R. Diehl, *Radioactive 26Al in the Galaxy: observations versus theory*, Physics Reports **267** (1996) 1.

[R3B05] *Technical proposal for the Design, Construction, Commissioning and Operation of R^3B: A universal setup for kinematical complete measurements of reactions with Relativistic Radioactive Beams*, Technical report, FAIR (2005).

[Rol88] C. E. Rolfs and W. S. Rodney, *Cauldrons in the Cosmos*, The University of Chicago Press (1988).

[ROO] *ROOT webpage*, `http://root.cern.ch`.

[Ros08] D. Rossi, *Investigation of the Dipole Resonance of Nickel Isotopes in the Presence of a High-Frequency Electromagnetic Field*, Ph.D. thesis, University of Mainz (2008).

[Sch01] H. Schatz *et al.*, *End Point of the rp Process on Accreting Neutron Stars*, Phys. Rev. Lett. **86** (2001) 3471–3474.

[Sta98] S. Starrfield *et al.*, *Evolutionary sequences for Nova V1974 Cygni using new nuclear reaction rates and opacities*, Monthly Notices of the Royal Astronomical Society **296** (1998) 502–522.

[Sta06] M. Stanoiu *et al.*, *Fragment tracking with Si microstrip detectors*, Technical report, GSI Scientific Report, FAIR-EXPERIMENTS 21 (2006).

[Tog08] Y. Togano, *Experimental Investigation of the Stellar $^{26}Si(p,\gamma\ )^{27}P$ via Coulomb Dissociation*, Ph.D. thesis, Rikkyo University (2008).

[Typ03] S. Typel and B. A. Brown, *Skyrme Hartree-Fock calculations for the α-decay Q values of superheavy nuclei*, Phys. Rev. C **67** (2003) 034313.

[Typ07] S. Typel, *Coulomb Breakup of ^{27}P into ^{26}Si + proton at 500 A MeV*, Private communication (2007).

[UNI] *UNILAC webpage*, `http://www-inj.gsi.de`.

[Wei34] C. von Weizsacker, *Radiation emitted in collisions of very fast electrons*, Z. Phys. **88** (1934) 612–625.

[Wil34] E. Williams, *Nature of the high-energy particles of penetrating radiation and status of ionization and radiation formulae*, Phys. Rev. **45** (1934) 729–730.

[Win79] A. Winther and K. Alder, *Relativistic Coulomb excitation*, Nuclear Physics A **319** (1979) 518–532.

[Zin98] A. Zinner, *Stellar nucleosynthesis and isotopic composition of presolar grains from primitive meteorites*, Annu. Rev. Earth Planet. Sci. **26** (1998) 147–188.

[Zuc00] P. Zuccona *et al.*, *Forward Spectrometer for Sudy of Low-lying Barion resonances. SPES4-π Experiment at Saturne II (Saclay)*, EP-9-2000-2352 (2000).